Aus dem Institut für Klinische Neuroimmunologie
der Ludwig-Maximilians-Universität München
Direktoren: Prof. Dr. Hohlfeld, Prof. Dr. Kerschensteiner

Aus der Abteilung für Neuroimmunologie
dem Max-Planck-Institut für Neurobiologie
Direktor: Prof. Dr. Hartmut Wekerle

Calcium signals in encephalitogenic T cells on their way into central nervous system tissues

An in vivo imaging study

Dissertation
zum Erwerb des Doktorgrades der Naturwissenschaften
an der Medizinischen Fakultät
der Ludwig-Maximilians-Universität München

vorgelegt von

Nikolaos I. Kyratsous

aus

Kozani, Griechenland

2016

Betreuer: **Priv. Doz. Dr. Naoto Kawakami**

Mitgutachter: **Prof. Dr. Gerhild Wildner**
Klinikum der Universität München, München
Augenklinik und Poliklinik

Prof. Dr. Peter Nelson
Klinikum der Universität München, München
Medizinische Klinik und Poliklinik IV

Priv. Doz. Dr. Reinhard Obst
BioMedizinisches Zentrum der LMU, München
Institut für Immunologie

Dekan: **Prof. Dr. med. dent. Reinhard Hickel**

Tag der mündlichen Prüfung: 21.12.2016

Eidesstattliche Versicherung

Nikolaos I. Kyratsous

Name, Vorname

Ich erkläre hiermit an Eides statt,

dass ich die vorliegende Dissertation mit dem Thema

Calcium signals in encephalitogenic T cells on their way into central nervous system tissues - An in vivo imaging study

selbständig verfasst, mich außer der angegebenen keiner weiteren Hilfsmittel bedient und alle Erkenntnisse, die aus dem Schrifttum ganz oder annähernd übernommen sind, als solche kenntlich gemacht und nach ihrer Herkunft unter Bezeichnung der Fundstelle einzeln nachgewiesen habe.

Ich erkläre des Weiteren, dass die hier vorgelegte Dissertation nicht in gleicher oder in ähnlicher Form bei einer anderen Stelle zur Erlangung eines akademischen Grades eingereicht wurde.

München, 03.08.2016

Ort, Datum   Unterschrift Doktorandin/Doktorand

Στο Χρήστο και στο Στέφανο

Εις τον Θεόκριτο παραπονιούνταν
μια μέρα ο νέος ποιητής Ευμένης·
«Τώρα δυο χρόνια πέρασαν που γράφω
κ' ένα ειδύλλιο έκαμα μονάχα.
Το μόνον άρτιόν μου έργον είναι.
Αλλοίμονον, είν' υψηλή το βλέπω,
πολύ υψηλή της Ποιήσεως η σκάλα·
κι απ' το σκαλί το πρώτο εδώ που είμαι
ποτέ δεν θ' ανεβώ ο δυστυχισμένος.»
Είπ' ο Θεόκριτος· «Αυτά τα λόγια
ανάρμοστα και βλασφημίες είναι.
Κι αν είσαι στο σκαλί το πρώτο, πρέπει
νάσαι υπερήφανος κ' ευτυχισμένος.
Εδώ που έφθασες, λίγο δεν είναι·
τόσο που έκαμες, μεγάλη δόξα.
Κι αυτό ακόμη το σκαλί το πρώτο
πολύ από τον κοινό τον κόσμο απέχει.
Εις το σκαλί για να πατήσεις τούτο
πρέπει με το δικαίωμά σου νάσαι
πολίτης εις των ιδεών την πόλι.
Και δύσκολο στην πόλι εκείνην είναι
και σπάνιο να σε πολιτογραφήσουν.
Στην αγορά της βρίσκεις Νομοθέτας
που δεν γελά κανένας τυχοδιώκτης.
Εδώ που έφθασες, λίγο δεν είναι·
τόσο που έκαμες, μεγάλη δόξα.»

Κ. ΚΑΒΑΦΗΣ - ΤΟ ΠΡΩΤΟ ΣΚΑΛΙ

(Από τα *Ποιήματα 1897-1933*, Ίκαρος 1984)

TABLE OF CONTENTS

SUMMARY

Multiple Sclerosis (MS) is an autoimmune disease, which features a highly complex pathogenic cascade and involves the infiltration of mononuclear cells into the brain and spinal cord. Although many essential steps in the development of the disease remain ambiguous, experimental and clinical studies indicate that autoreactive CD4$^+$ helper T cells are crucial for induction of inflammation in the central nervous system (CNS). By using Experimental Autoimmune Encephalomyelitis (EAE) as an animal model for MS, it was previously shown that encephalitogenic T cells mature in peripheral organs. Next, T cells migrate to the CNS, become activated, and initiate inflammation. During their sojourn, the T cells perceive stimuli and respond to their microenvironment through signal transduction mechanisms.

To portray the serial signaling in transfer EAE (*t*EAE), two activation reporters, a FRET-based calcium biosensor and a fluorescent NFAT activation marker were combined with *in situ* two-photon microscopy. The Twitch calcium sensor can detect weak signals which are accumulated within the cells and lead to T cell activation. On the other hand, NFAT sensor can reliably detect T cell activation induced by antigen recognition *in vivo*. During T cell maturation in the spleen, both myelin basic protein (MBP) specific encephalitogenic and OVA specific control T cells displayed similarly low frequent and short-lasting calcium signaling. This process was driven by chemokine and MHC class II-dependent signals. Next, arrived at leptomeningeal blood vessels, the portal to the spinal cord, intravascular T cells presented minimal calcium activity. Short-lasting calcium signaling was detected only during rolling-crawling transitions. After extravasation, in spinal cord leptomeningeal space and parenchyma, the T cells responded with high, sustained calcium plateaus, and NFAT translocation. T cells presented longer-lasting elevated calcium levels (>2 min) after contacting local antigen presenting (APC) cells, whereas OVA specific T cells presented only short calcium spikes. Each APC displayed different potential to stimulate T cells likely due to the limited availability of immunogenic myelin proteins. This T cell reaction was most pronounced in the prodromal phase, and followed a 'first come – first served' rule for antigen recognition. When MHC class II was blocked by intrathecal injection of blocking antibody, MBP specific T cells presented only short-lasting calcium signaling similar to those in the spleen. Accordingly the treatment reduced the infiltration of T cells and clinical severity.

To directly correlate the activation of encephalitogenic T cells with their calcium signaling, a new combined sensor was generated. The co-expression of Twitch and ΔNFAT protein required a set of fluorescent proteins (FP) that would have minimal bleed through in their emission channels. Five FPs were evaluated, and mRuby2 was selected as the red analogous counterpart of ΔNFAT-GFP. In combination with

Twitch, ΔNFAT-mRuby2 displayed similar translocation kinetics compared to ΔNFAT-GFP and presented adequate two-photon absorption. Nonetheless, more detailed studies need to be performed regarding the dual sensors' transduction efficiency.

ZUSAMMENFASSUNG

Multiple Sklerose (MS) ist eine Autoimmunerkrankung mit einer hochkomplexen pathogenen Kaskade, die mit der Infiltration mononuklearer Zellen in das Gehirn und das Rückenmark einhergeht. Wenngleich viele essentielle Schritte in Krankheitsausbruch und -verlauf noch ungeklärt sind, offenbaren experimentelle und klinische Studien, dass autoreaktive $CD4^+$-T-Helferzellen für die Induktion der Entzündung im zentralen Nervensystem eine wesentliche Rolle spielen. Mithilfe der experimentellen autoimmunen Enzephalomyelitis (EAE) als Tiermodell für MS konnte gezeigt werden, dass enzephalitogene T-Zellen in der Peripherie heranreifen, bevor sie in das ZNS einwandern, dort aktiviert werden und Entzündungen auslösen. Während ihres Aufenthalts erhalten die T-Zellen Stimuli und reagieren über Signaltransduktionsmechanismen auf ihre Mikroumgebung.

Um die seriellen Signalwege in adoptiv transferierter EAE darstellen zu können, wurden zwei Aktivierungsreporter mit *in situ* Zwei-Photonen-Mikroskopie kombiniert: Twitch, ein FRET-basierter Calcium-Biosensor, und mit einem Fluorophor markiertes NFAT. Twitch ist in der Lage, schwache Signale zu detektieren, die in den Zellen akkumulieren und zur T-Zell-Aktivierung führen. Das mit einem Fluorophor markierte NFAT hingegen macht durch *in vivo* Antigenerkennung ausgelöste T-Zell-Aktivierung sichtbar. Während der T-Zellreifung in der Milz zeigten sowohl die für das Myelin-basische Protein (MBP) als auch die als Kontrolle dienenden für Ovalbumin (OVA) spezifischen T-Zellen wenige und kurze Calcium-Signale. Dieser Prozess wird von Chemokin- und MHCII-abhängigen Signalen gesteuert. Im nächsten Schritt - in den leptomeningealen Blutgefäßen, die für T-Zellen das Tor zum Rückenmark darstellen - wiesen intravaskuläre T-Zellen eine minimale Calcium-Aktivität auf. Kurze Calcium-Signale wurden nur während des Übergangs vom Rollen zum Kriechen der T-Zellen an der Blutgefäßwand detektiert. Nach der Extravasation in den leptomeningealen Raum und das Rückenmarksparenchym reagierten die T-Zellen mit konstant hohen Calcium-Levels und NFAT-Translokation. Die MBP-spezifischen T-Zellen zeigten eine langanhaltende Erhöhung des Calciumspiegels (>2 min) nach dem Kontakt mit lokalen Antigen-präsentierenden Zellen, wohingegen in OVA-spezifische T-Zellen nur kurze Calcium-Spikes ausgelöst wurden. Die Antigen-präsentierenden Zellen hatten unterschiedlich starke Effekte auf die T-Zell-Stimulation, vermutlich aufgrund der begrenzten Verfügbarkeit immunogener Myelinproteine. Diese Reaktion der T-Zellen war in der Prodromalphase am stärksten ausgeprägt und folgte in Bezug auf die Antigenerkennung dem Prinzip „wer zuerst kommt, mahlt zuerst". Bei Blockierung der MHCII-Moleküle durch intrathekale Injektion blockierender Antikörper wiesen MBP-spezifische T-Zellen nur einen kurzen Anstieg der intrazellulären Calciumkonzentration auf, vergleichbar mit den Calciumsignalen während der Reifung in der Milz.

Dementsprechend minderte diese Behandlung die Infiltration von T-Zellen in das ZNS und somit den Schweregrad der klinischen Symptome.

Für die direkte Korrelierung der Aktivierung der enzephalitogenen T-Zellen mit deren Calciumsignalen wurde ein kombinierter Sensor entwickelt. Die Co-Expression von Twitch und dem ΔNFAT-Protein erforderte eine Zusammenstellung von Fluoreszenzproteinen mit minimalem Bleedthrough in die jeweils anderen Emissionswellenlängen. Fünf Fluoreszenzproteine wurden getestet und mRuby2 wurde als im roten Wellenlängenbereich emittierendes Pendant zu ΔNFAT-GFP ausgewählt. In Verbindung mit Twitch wies ΔNFAT-mRuby2 eine ähnliche Translokationskinetik wie ΔNFAT-GFP mit geeigneter Zwei-Photonen-Absorption auf. Nichtsdestotrotz sind detailliertere Untersuchungen nötig, um die Transduktionseffizienz des Doppelsensors vollständig zu bestimmen.

INTRODUCTION

1.1 Multiple Sclerosis

Multiple Sclerosis (MS) is a chronic autoimmune demyelinating disease of the central nervous system (CNS) in which the interplay between inflammatory and neurodegenerative processes results in inflammation, demyelination and axonal damage. The timeline of MS research arises with Charcot's definition and naming of MS back in 1868 and Dawson's reports about MS neuropathology in 1916. Since then, MS still remains an indecipherable disease which has been, however, treatable for approximately the last 20 years (Ransohoff et al., 2015).

Four patterns of disease evolution have been described extensively. Relapsing remitting MS (RRMS), secondary progressive MS (SPMS), primary progressive MS (PPMS) and progressive relapsing MS (PRMS) share common pathophysiology but differ in symptom severity, clinical score and CNS lesion morphology. In RRMS, patients experience relapses about once per 2 years and after 15 to 25 years this MS pattern may lead to SPMS (Scalfari et al., 2014). On the contrary, in PPMS pattern no relapses occur and it targets only a small minority of total patients. Most people are diagnosed between the ages of 20 and 40 (Ransohoff et al., 2015) and most forms of MS affect women with higher prevalence ratio (2.3-3.5:1) (Harbo et al., 2013).

Although the pathogenic mechanisms of MS are largely unknown, experimental and clinical studies implicate the immune system. Both T cell and B cell-dependent mechanisms are involved; B cells form follicle-like aggregates in the meninges of SPMS patients (Howell et al., 2011). While detailed mechanisms are not clear, $CD4^+$ helper T cells play an important role in the formation of CNS infiltration. Autoreactive $CD4^+$ T cells exist even in healthy individuals; however, in most cases, they do not induce autoimmunity. It is speculated that only after a specific triggering in peripheral organs, autoreactive T cells are able to infiltrate into their target organ and initiate a cascade of inflammatory events like recruiting other types of immune cells, such as monocytes and B cells. Leukocyte infiltration has been reported in grey and white matter and both in chronic and presymptomatic MS lesions (Ciccarelli et al., 2014). In addition, cytotoxic and pro-inflammatory factors from the inflamed meninges further activate CNS-homing and CNS-resident innate immune cells and contribute to demyelination and neurodegeneration (Friese et al., 2014). Notably, neuronal damage is the main contributor to permanent clinical disability in MS and may occur even without demyelination (Bitsch et al., 2000) or even with an intact Blood Brain Barrier (BBB) in patients with PPMS (Frischer et al., 2009).

Numbers of studies have shown that MS presents a complex etiology and various risk factors influence MS incidence, e.g. genetic (Hillert and Olerup, 1993), environmental (Ragheb and Lisak, 1993) and viral infections through molecular mimicry (Serafini et al., 2007). Genetic predisposition is obvious in monozygotic twins, who they feature a much higher concordance (25%) when compared to dizygotic twins (5%) or to their non-twin siblings (2.9%) (Willer et al., 2003). The principal genetic loci determining susceptibility to MS is the Human Leukocyte Antigens (HLA) loci and it either has disease-associated alleles (e.g. HLA-A*0301) (Harbo et al., 2004) that confer a greater risk of MS development or protective-associated alleles (e.g. HLA-A*0201, HLA-C*05) (Yeo et al., 2007, International Multiple Sclerosis Genetics et al., 2011) which decrease the risk of MS. In addition, recently genome-wide association studies have shown that an intriguing proportion of non-Major Histocompatibility Complex (MHC) genetic variants fall near genes related to the immune and nervous system and are significantly associated with the disease. In particular, many variants are located close to genes that are involved in the T helper cell differentiation pathway, including genes coding for cytokine pathway (e.g. *CXCR5*, *IL7*, *IL12A*) co-stimulatory (e.g. *CD37*, *CD40*) and signal transduction (e.g. *STAT3*, *MALT1*) (International Multiple Sclerosis Genetics et al., 2011). The IL2RA (also known as CD25) genetic variant has recently been negatively associated with MS susceptibility (Maier et al., 2009).

As of today, Vitamin D has been highlighted as the most crucial environmental risk factor for MS and its role has been confirmed through many population and epidemiological studies. High-latitude regions tend to have higher rates of MS compared to regions closer to the equator where people get more sunlight and have higher blood levels of vitamin D (Smolders, 2011). However, a functional interaction between MS and vitamin D has been indicated by many genetic studies as well. The expression levels of HLA molecules have been linked to vitamin D levels (Ramagopalan et al., 2009) and it has been reported that the vitamin D receptor binding sites are significantly enriched near MS associated genes (Ramagopalan et al., 2010).

1.2   Experimental Autoimmune Encephalomyelitis

MS presents a complex disease with variable clinical and pathological manifestations and involves diverse pathogenic pathways that have been difficult to be fully recapitulated by a single experiment model. Experimental Autoimmune Encephalomyelitis (EAE) is a well-established animal model for MS and it is widely used. Although many different EAE models are available, none of them covers the entire MS pathology and each of them mimics only a particular facet of the disease.

A precursor of an EAE model was suggested by Rivers et al. in 1933 (Rivers et al., 1933). These early attempts were able to induce encephalomyelitis to rhesus monkeys by repeated injections of rabbit brain matter. The aim of this study was to decipher the pathogenesis of post rabies vaccination; however, during that time '*the relation of the injections to the disease of the nervous system was not clear'*. Only after the introduction of complete Freund's adjuvant (Freund et al., 1947), the induction of EAE became more reliable and simple. At first, two protein components of myelin, myelin basic protein (MBP) and proteolipid protein (PLP), were characterized as encephalitogenic and considered target antigens in MS (Ben-Nun et al., 2014). Over the years, a plethora of potential autoantigens have been tested for the induction of EAE such as the myelin oligodendrocyte glycoprotein (MOG) or other non-myelin CNS antigens like the glial antigens GFAP and S100β (Krishnamoorthy and Wekerle, 2009).

EAE can be induced by various ways, including active immunization with Freund's adjuvant, spontaneous EAE models by using transgenic mice (Pöllinger et al., 2009) and adoptive transfer of autoreactive T cells (Ben-Nun et al., 1981a). The consensus behind these methods is the central role of autoreactive CD4$^+$ helper T cells. For example, during active immunization with a target autoantigen, autoreactive T cells expand *in vivo*. Also, the transgenic mice which develop spontaneous EAE overexpress self-reactive T cell receptors (TCR). More directly, during adoptive transfer, autoreactive CD4$^+$ T cells are the driving force that induces EAE.

1.2.1 Adoptive transfer EAE in rat

Although there are many EAE models available (Krishnamoorthy et al., 2006, Pöllinger et al., 2009, Madsen et al., 1999), unfortunately none of them can reproduce the MS disease course with precision. Therefore, it is necessary to select the suitable model for each research topic. Amongst the EAE models, the adoptive transfer EAE (*t*EAE) using Lewis rats is suitable for studying T cell infiltration into the CNS. *t*EAE has been used before for validating therapeutic compounds in drug screening and for studying the migratory behavior of T cells during the clinical course of EAE (Krishnamoorthy and Wekerle, 2009).

In this model, EAE is induced in naïve recipient animals by adoptive transfer of *in vitro* activated CNS autoantigen specific T cells (Ben-Nun et al., 1981b). After a few days of pre-clinical phase, animals lose their body weight and show paralysis of tails and hind limbs. In contrast to MS or to other EAE models, demyelination in the CNS is minimum. The disease course is monophasic and lasts around 1 week. Then, the animals recover and do not show any signs of relapse. Notably, in this *t*EAE model, the T cell immigration to the CNS displays highly reproducible disease course and fits very well to clinical observations.

After transfer, the majority of activated autoreactive T cells do not directly migrate into the CNS; on the contrary, they take a complicated biphasic journey on their way to their target tissue (Fig. 1.2.1). Indeed, the migratory pathway of MBP specific T cells was revealed after their genetic labeling with Green fluorescent protein (GFP) (Flügel et al., 1999). Within 2 hours after the transfer, MBP specific T cells migrate to the lungs (Klinkert, 1987). Then, on day 1-2 post transfer (p.t.), they start to accumulate in the perithymic lymph nodes. Afterwards, T cells infiltrate into the spleen on day 3 p.t. via blood circulation. At the same time, T cells start to infiltrate into the CNS gradually and present massive infiltration on day 4 p.t. at the peak of the disease. During the acute phase of EAE, other types of immune cells, including T cells, B cells and macrophages are recruited into the CNS and contribute to the inflammation. During the recovery phase, the population of MBP specific T cells dramatically decreases and disappears from the CNS.
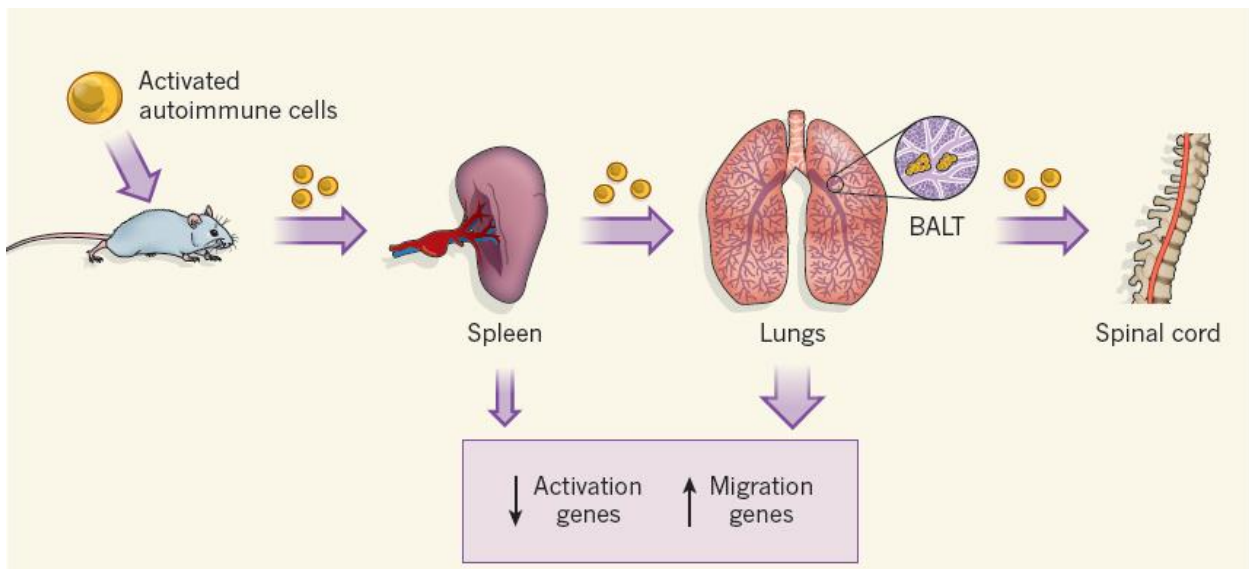
Figure 1.2.1 Maturation of encephalitogenic T cells in peripheral organs. Encephalitogenic T cells acquire migratory phenotype which is characterized by down-regulation of activation markers and up-regulation of chemokine receptors and MHC class II. Thereafter, the mature migratory T cells can infiltrate into the CNS. There are several organs suggested as place for the maturation, such as the spleen, the small intestine and the lungs (adapted from Ransohoff, 2012).

1.3   T lymphocytes infiltration into the CNS

1.3.1 T lymphocytes in pre-clinical phase

in vitro activated T cells infiltrate into the lung and the small intestine shortly after adoptive transfer. Afterwards, they acquire a migratory phenotype in the spleen where they down-regulate their cell surface activation markers, for example OX-40 and CD25 and they up-regulate chemokine receptors such as CCR5, CCR7 and CXCR4. Chemokine receptors may be important for the infiltration into the target

organ by detecting chemokines which are produced by endothelial cells and are embedded on extracellular matrix. Indeed, T cells transferred from the spleen infiltrate into the spinal cord faster than *in vitro* activated T cells (Flügel et al., 2001). Importantly, non-encephalitogenic activated T cells follow a similar migratory pathway but they infiltrate into the CNS in low numbers.

However, it still remains under investigation why the T cells acquire this migratory phenotype in the spleen. There is possibly an antigen-dependent interaction between T cells and local antigen presenting cells (APCs), or alternatively, there is an interaction via adhesion molecules. Since many factors from the environment can be incorporated into the lung during breathing, the lung environment is certainly an interesting location for T cell maturation. In fact, recently, it was shown that the lungs are another milieu of maturation for MBP specific T cells (Odoardi et al., 2012, Ransohoff, 2012). In another study, it was suggested that gut microbiota activate encephalitogenic T cells in a mouse spontaneous EAE model (Berer et al., 2011). Taken together, T cells may get signaling in gut associated lymphoid tissue (GALT), including Peyer's patches and lamina propria. Nonetheless, more detailed studies need to be performed regarding the role of lung and GALT in T cell activation.

1.3.2 Breaching the Blood Brain Barrier

CNS is considered as an immunoprivileged site while a healthy brain is nearly devoid of immune cells. The presence of BBB acts as a physical and functional barrier that prevents the entry of toxic substances and immune cell trafficking from the periphery into the CNS. BBB is formed by a tightly sealed monolayer of endothelial cells and cooperates closely with the surrounding astrocytes, pericytes and microglia (Zlokovic, 2008). This dynamic interface is not always solid while activated T cells are able to modify and breech the BBB permeability (Engelhardt and Coisne, 2011). During EAE, BBB breaching initiates with the prodromal T cell infiltration and progresses with the subsequent perivascular leukocyte accumulation. However, the infiltration of autoantigen specific T cells into the CNS seems to be insufficient to induce CNS inflammation. It was shown that both encephalitogenic T cell infiltration into the CNS and activation are necessary to induce clinical EAE (Kawakami et al., 2004).

Adoptively transferred T cells appear within the blood vessels at the spinal cord leptomeninges. Those T cells, at first, roll and later crawl on the intraluminal surface (Fig. 1.3.1). Rolling cells follow the blood stream with high velocity and tether to the endothelial cells in a P-selectin-dependent manner (Piccio et al., 2002). Circulating CD4^{+} T cells with high levels of PSGL-1 and increased transmigration capacity across BBB have been found in MS patients (Bahbouhi et al., 2009). The transition from rolling to crawling is mediated mainly via integrins. Indeed, treatment with anti-integrin α4 and αL antibodies

diminished crawling cells and ameliorated the clinical symptoms of EAE (Bartholomäus et al., 2009). T cells adhere and crawl preferentially against the direction of the blood flow at velocities of 12-13 µm/min (Bartholomäus et al., 2009). Crawling is BBB-specific, as it is rarely observed in any peripheral organ (Bartholomäus et al., 2009) and it is antigen-independent (Pesic et al., 2013).

After intraluminal crawling, which lasts 15 minutes on average, T cells extravasate to the leptomeningeal area through the BBB. Diapedesis occurs via two different pathways: either the para-cellular or the trans-cellular pathway (Engelhardt and Ransohoff, 2012). The duration of diapedesis is around 10-20 min (Bartholomäus et al., 2009). Intraendothelially stored chemokines seems to play an important role in diapedesis (Shulman et al., 2012), however, as of today, the signals that favor diapedesis have remained obscure.
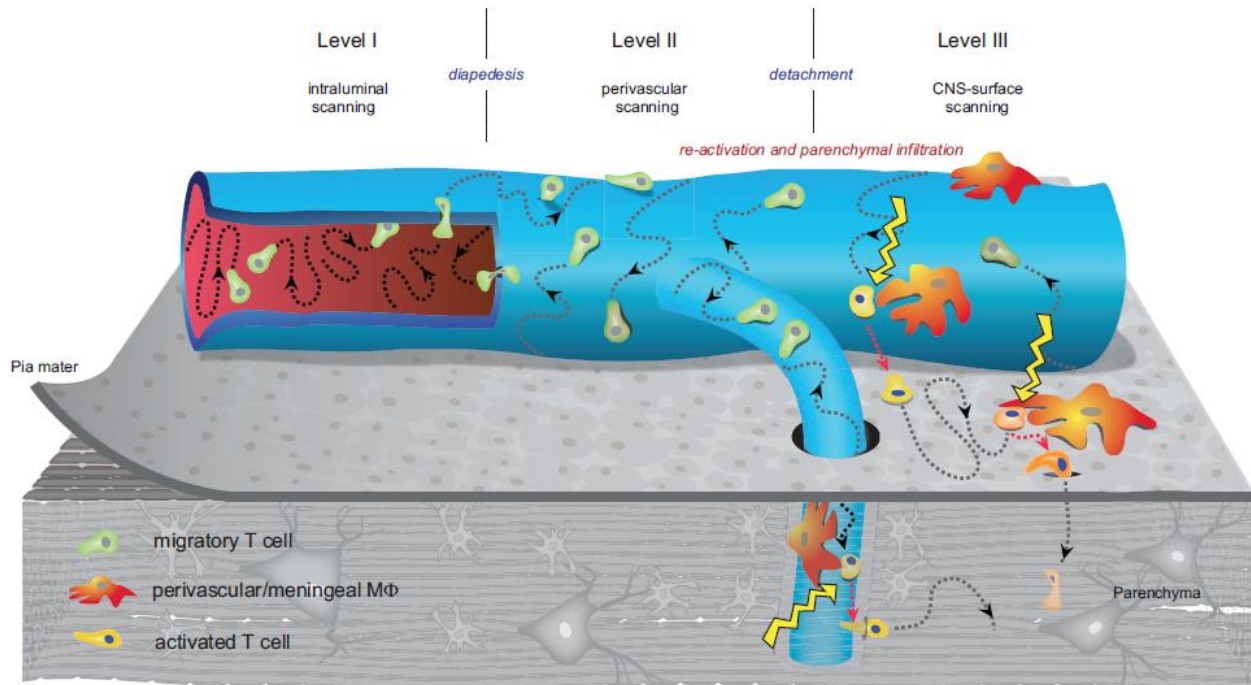
Figure 1.3.1 The invasion steps of encephalitogenic T cells into the CNS tissue (adapted from Bartholomäus et al., 2009).

1.3.3 T lymphocytes infiltration into the CNS beyond the Blood Brain Barrier

After the extravasation, infiltrated T cells continue to scan the outer surface of leptomeningeal vessels and interact with local APCs (Bartholomäus et al., 2009). Depending on the different stages of the clinical course, these contacts may vary from short interactions (only a few minutes) to constant prolonged interactions (10-30 min). Although all evidences suggest that T cells are activated in the spinal cord leptomeninges, as of today, it has not been possible to visualize the T cell activation *in situ* due to

methological limitations. Pesic et al. (Pesic et al., 2013) as well as others (Lodygin et al., 2013, Marangoni et al., 2013) visualized T cell activation by applying a nuclear factor of activated T cells (NFAT)-GFP fusion protein during intravital imaging. They reported that infiltrated encephalitogenic T cells become activated when they contact with local APCs, while NFAT-GFP fusion protein translocates from cytosol to nucleus.

Afterwards, activated T cells penetrate deeper within the CNS parenchyma. The majority of T cells follow a motile pattern with high velocity and spontaneous movement (Kawakami et al., 2005). Intravital recordings revealed immunological synapses during the stationary phase of T cells. These results suggest that T cells may be further activated in parenchyma by local APCs.

1.4 Calcium signaling in T lymphocytes

Calcium is a universal second messenger important for a diverse range of T cell functions including proliferation, differentiation, homeostasis, activation and cell death. The sequence of T cell signaling events is tightly regulated by positive and negative feedback pathways that involve cytosolic and transmembrane molecules in cooperation with a plethora of ion channels. In resting T cells the cytosolic calcium concentration is maintained at ~50-100 nM, whereas following T-cell receptor (TCR) stimulation it elevates to ~1 μM (Joseph et al., 2014). The extracellular calcium concentration across the plasma membrane (PM) is ~1 mM and consists an important calcium pool in addition to the endoplasmic reticulum (ER) which also features elevated calcium concentration (~500 nM).

T cells are processing extracellular stimuli into an encoded calcium signal which subsequently coordinates downstream T cell functions. During calcium signaling, calcium does not function as a binary switch; instead it displays a variety of signaling patterns like single transient spikes, repetitive oscillations or sustained plateaus. These patterns differ in amplitude and frequency which are important parameters for determining the efficiency and the specificity of cellular responses. For example, NFAT nuclear translocation initiates by frequent rapid oscillatory calcium signals (Dolmetsch et al., 1998) and is preserved with sustained and low-calcium levels (Dolmetsch et al., 1997). On the contrary, nuclear factor kappa B (NFκB) is activated only by transient and infrequent spikes of high-calcium signals (Song et al., 2012) and remains in the nucleus for a longer period of time compared to NFAT (Dolmetsch et al., 1997). Moreover, the concentration of peptides affects the calcium oscillations in cytotoxic T cells, as low peptide concentrations reduce the magnitude of calcium and produce higher oscillations (Faroudi et al., 2003). On the other hand, it was reported that calcium oscillations increase the sensitivity of T cells to detect weak stimuli like low doses of antigen (Lewis, 2001).

1.4.1 Calcium flux through TCR engagement

Upon a T cell recognizes its target cell and conjugates with it through the immunological synapse (IS), it undergoes cytoskeletal rearrangements and exhibits a dramatic increase of intracellular calcium concentration within seconds (Fig. 1.4.1). A key initiating event after the engagement of the specific antigen is the increased phosphorylation of the immunoreceptor tyrosine-based activation motifs (ITAMs) on the cytosolic side of the TCR-CD3 complex by the SRC family kinases LCK and Fyn (Mustelin and Tasken, 2003). Subsequently, the ZAP-70, which is a CD3ζ-chain-associated tyrosine kinase protein (TKP), is activated and results in the formation of signaling microclusters (Balagopalan et al., 2009). The phosphorylation of the CD3ζ-chain also initiates other phosphorylation events for many adaptor proteins such as SLP76 (SRC-homology-2-domain-containing leukocyte protein of 76 kDa) and the transmembrane adaptor protein LAT (linker for activation of T cells) (Feske, 2007). LAT acts as a scaffold with many docking sites for SRC homology 2 (SH2) domain-containing adapter proteins including phospholipase Cγ1 (PLCγ1), Grb2 and Grb2-related adaptor proteins (GADS) (Joseph et al., 2014). SLP76 is indirectly associated to LAT through its binding with the SH3 domain of GADS and is involved in the recruitment of several signaling molecules including regulators of calcium signaling and integrin activation (Balagopalan et al., 2009).
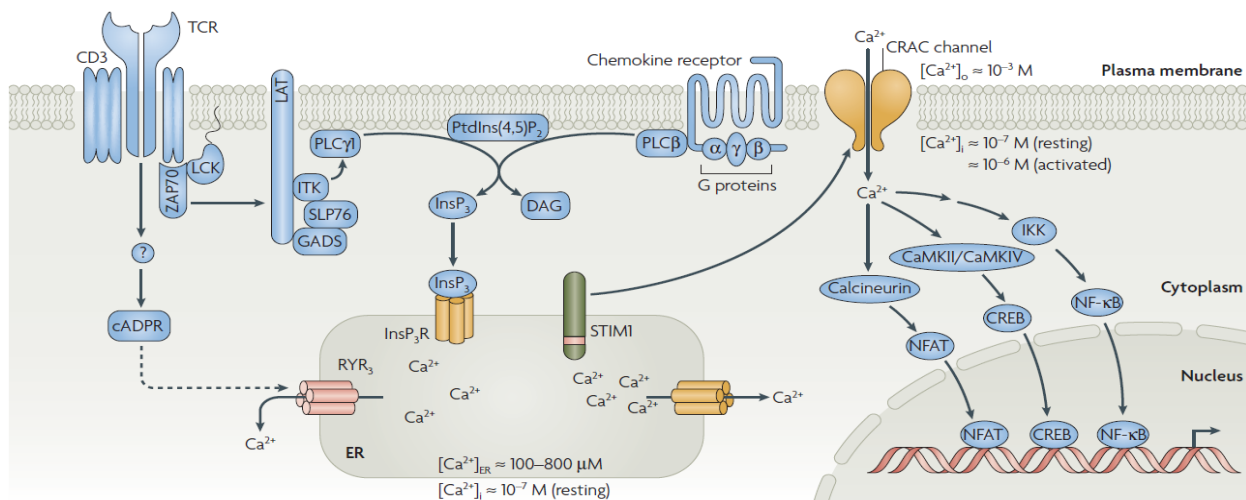
Figure 1.4.1 T cell calcium cascade through TCR engagement or chemokines. In resting T cells, a steep gradient in calcium concentrations exists between the cytoplasm and the extracellular space, as well as between the cytoplasm and the lumen of the ER. The intracellular calcium concentrations in T cells is tightly regulated and kept between ~100 nM in resting cells and ~1000 nM following TCR stimulation. Antigen recognition through the TCR results in the activation of protein tyrosine kinases, such as LCK and ZAP70, which initiate phosphorylation events of adaptor proteins, such as SLP76 and LAT. This leads to the recruitment and activation of ITK and PLCγ. Similarly, binding of G protein-coupled chemokine receptors results in the activation of PLCβ. PLCβ and PLCγ catalyse the hydrolysis of the membrane PtdIns(4,5)P2 to IP₃ and DAG. IP₃ binds to and opens IP₃ receptors in the membrane of the ER, resulting in the release of calcium from intracellular calcium stores. A decrease in the calcium content of the ER is sensed by STIM1, which in turn activates CRAC channels in the plasma membrane. Calcium influx through CRAC channels and elevated intracellular calcium concentration activate calcium-dependent enzymes, such as calcineurin, and thereby transcription factors, such as NFAT or NF-κB (adapted from Feske, 2007).

A series of signaling events ensue following the phosphorylation of LAT. PLCγ1 is phosphorylated by the interleukin-2 (IL-2)-inducible T-cell kinase (Itk), and undergoes a conformational change (Joseph et al., 2014). PLCγ1 catalyses the hydrolysis of the membrane phosphatidylinositol 4,5-bisphosphate in order to produce the second messengers cytosolic inositol triphosphate (IP_3) and membrane-associated lipid, diacylglycerol (DAG) (Christo et al., 2015). DAG activates PKCθ and the MAPK/ERK pathways that promote the activation of the transcription factors activator protein-1 (AP-1) and the NF-κB to induce cytokine gene transcription (Schulze-Luehrmann and Ghosh, 2006). IP_3 binds to its tetrameric IP_3 receptor (IP_3R) on the ER membrane, triggering the opening of the IP_3R channels and release of calcium from intracellular calcium stores (Joseph et al., 2014). The aforementioned release serves as the primary rise of calcium levels in the cytosol and generates an intracellular calcium concentration of up to 500nM, almost five-fold higher than the basal levels (Christo et al., 2015).

Nevertheless, calcium influx from ER stores makes a relatively small contribution and mainly serves as a sensitive trigger for controlling a much larger flux of calcium across the plasma membrane. Several important ion channels that belong to store-operated calcium entry (SOCE) and mediate calcium influx and release have been reported including IP_3 receptors (Kotturi et al., 2006), transient receptor potential channels (Omilusik et al., 2013), ATP-responsive purinergic P2 receptors (Junger, 2011), *N*-methy-D-Aspartate activated receptors (Affaticati et al., 2011) and voltage-dependent calcium channels (Feske et al., 2012).

In lymphocytes, the calcium-release-activated calcium (CRAC) channels are the main source of calcium influx and are composed of a hexamer containing six ORAI subunits (Hou et al., 2012). The depletion of calcium from ER is sensed by the stromal cell interaction molecule (STIM) proteins STIM1 and STIM2 which translocate to PM via ER microtubules (Pozo-Guisado et al., 2013). These proteins are key regulators of SOCE and they trigger sustaining intracellular calcium above resting levels for some minutes, up to hours. In general, when calcium stores are replete in ER, STIM1 exists as a monomer and calcium binds to their EF hand domain causing a closed and stable inactive conformation. Following the depletion of calcium stores in ER, calcium dissociates from the EF hand domain of STIM1 resulting in the oligomerization of STIM1 molecules and their accumulation in puncta in regions of ER located 10-25nm beneath the PM (Park et al., 2009). ORAI1, which exists as a dimer in PM, upon STIM1 coupling forms tetramers and mediates the opening of the ORAI channels (Penna et al., 2008).

Following the opening of ORAI channels, a sustained influx of extracellular calcium occurs and promotes the binding of calcium to the four high affinity EF-hands of calmodulin (CaM). CaM binds and activates calcineurin which in turn dephosphorylates the inactive NFAT transcription factor resulting in the

translocation of NFAT into the nucleus and the induction of NFAT-mediated gene transcription (Macian, 2005).

1.4.2 Calcium flux through chemokine receptors

Independently of the TCR engagement, T cells may also attain a migratory phenotype through calcium influx pathways during leukocyte trafficking. This multi-step process involves a precise interplay between chemokines, selectins and integrins binding. For example, chemokines induce a conformational change to integrins from intermediate to high affinity and avidity in order to initiate firm arrest and support the subsequent migration.

Chemokine receptors belong to the seven transmembrane (7TM) G protein coupled receptor (GPCR) family and play a crucial role in a diverse range of functions like in development and homeostasis, or in host response to inflammation and infection. In general, GPCRs trigger leukocyte mobilization towards the source of chemokine gradients, a process often referred to as chemotaxis. As of today, 23 different chemokine receptors have been unidentified and 48 chemokine ligands can activate them (Zweemer et al., 2014).

All 7TM receptors follow a general activating mechanism regardless the binding site of the agonist or the chemical nature of it (Jensen and Rosenkilde, 2009). Endogenous chemical agents or exogenous stimuli like peptides, ions or biogenic amines induce GPCRs activation and transduce this signal via a mechanism of G protein coupling. More specifically, upon ligand binding and agonist stimulation, 7TMs undergo intracellular conformational changes and form active-state complexes with heterotrimeric GTP-binding proteins (G proteins). Also, it has been reported that some GPCRs reside in the PM in a conformational equilibrium between active and inactive biophysical states and the type of the ligand may shift the equilibrium toward the active receptor state (Bennett et al., 2011). In active state complexes, the recruited Gα subunits release GDP and exchange it for GTP. This exchange leads to the dissociation of G proteins into activated α subunit and βγ dimers (Reiter and Lefkowitz, 2006). Then, the G protein subunits stimulate enzymes such as adenylate cyclase or phospholipase Cβ (PLCβ) (Fig. 1.4.1). Next, PLCβ cleaves phospholipids to produce IP_3 and DAG. Similar to calcium flux through TCR engagement, IP_3 production triggers the release of calcium from intracellular ER stores. It is important to note that SOCE activation is triggered only by the reduction of calcium levels in ER stores and not by any signaling molecule like G proteins, PLC or IP_3 (Park et al., 2009).

The magnitude and the duration of the chemokine signaling are mainly dependent on five different factors; the chemokine concentration and exposure time, the GPCR desensitization, the GPCR

internalization and the GPCR phosphorylation. All these functions are regulated and coordinated by the G protein coupled receptor kinases (GRKs) and β-arrestins (Reiter and Lefkowitz, 2006). Also, evidence suggests that G proteins are also pre-coupled with GPCRs prior to ligand-induced activation in inactive state complexes in order to increase the sensitivity and accelerate the onset of signaling (Qin et al., 2011).

1.5   Imaging T lymphocytes activation *in vivo*

In the past 50 years, many studies have revealed the dynamic nature of immune cells that allows them to invade and migrate within different tissues (Gowans, 1966). However, only the last decade and with the advent of biochemical, genetic and high resolution imaging tools it has been possible to identify and analyze the choreography of specific immune cell populations at the single-cell level. Indisputably, a crucial achievement was the introduction of fluorescent proteins into immune cells (Flügel et al., 1999). In combination with two-photon microscopy, it is possible nowadays to trace on a subcellular level the spatial and temporal regulation of many signaling pathways (Cahalan and Parker, 2008).

As it was mentioned before, calcium is one of the most well-known intracellular signaling molecules for many intracellular signaling cascades, including T cell activation and chemokine receptor triggering. Many experiments were performed before using chemically synthesized calcium indicator dyes such as Fura-2 (Grynkiewicz et al., 1985), Fluo-3 (Minta et al., 1989) and Indo-1 (Tsien et al., 1985) in immune and neuronal cells. However, a main disadvantage of these sensors is that T cells pump out dyes in a range of several hours via multi-drug resistance transporters (Sommer et al., 1994). Besides, they are applicable only for short-term experiments due to extensive cell proliferation (Randriamampita and Lellouch, 2014).

To overcome the aforementioned limitations, a genetically encoded calcium Förster/fluorescence resonance energy transfer (FRET)-based biosensor (Miyawaki et al., 1997) was introduced in HeLa cells. This biosensor consisted of two fluorescent proteins (FP), CaM and a calmodulin-binding peptide M13 derived from the myosin light-chain kinase. Upon calcium chelation, CaM wraps around the M13 domain and energy transfers between the flanking FPs.

This proof of concept was followed later for the construction of the TNXXL biosensor (Mank et al., 2008). TNXXL is based on a Troponin C (TnC) calcium binding domain instead of CaM, flanked by the two FPs CFP and cpCitrine. This intracellular calcium indicator was modified and optimized in order to be expressed in mouse T cells (Mues et al., 2013). Mues et al. described that the high degree of sequence homology in the coding regions of cpCitrine and CFP impeded the expression of TNXXL in T cells. In fact, Rhode et al. reported deletions of the direct tandem repeats during virus replication (Rhode et al., 1987).

To circumvent these limitations, cpCitrine was codon diversified ([CD]) by inserting silent mutations and maintaining the amino acid sequence intact. The affinity of this new calcium sensor, Twitch1, was further improved by replacing the TnC domain with a higher calcium-binding moiety.

Similar to the first descripted FRET sensor, in a low-calcium environment, Twitch1 emits cyan fluorescence upon CFP excitation (Fig. 1.5.1A). This situation changes dramatically when intracellular calcium concentration elevates. Intracellular calcium binds very rapidly to the TnC[CD] domain and induces conformational change of Twitch1, i.e. CFP and cpCitrine[CD] become in close proximity to each other. Under this condition, emitted light from CFP excites cpCitrine[CD] and cpCitrine[CD] emits yellow fluorescence (Fig. 1.5.1B). By analyzing the ratio (cpCitrine[CD] /CFP), the intracellular calcium could be quantified. This ratiometric analysis marks a major advantage on intravital imaging experiments. In general, because of the fact that T cells are moving *in vivo* at the three dimensional volume, the fluorescence can be influenced by the imaging depth and becomes error-prone. However, this is not the case for Twitch1 ratiometric analysis, since both CFP and cpCitrine[CD] emissions are influenced by imaging depth in the same manner. Also, Twitch1 expressing mouse T cells demonstrated similar reactivity against their specific antigens compared to Twitch1 negative counterparts. In addition, Twitch1-labeled encephalitogenic T cells did not lose their encephalitogenicity or alter their phenotype. It is important to note that the expression levels of Twitch1 were constant during the entire course of the disease.
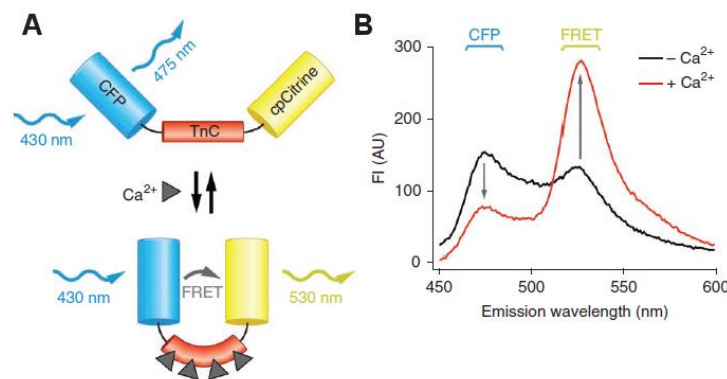
Figure 1.5.1 A. Schematic representation of the calcium sensor TN-XXL. Cyan fluorescent protein (CFP) and a yellow fluorescent protein (cpCitrine) are connected by a calcium sensitive troponin C domain (TnC). At low calcium environment, protein emits blue light. Upon calcium influx, protein emits yellow light. B. Spectrophotometric analysis of lysate from TN-XXL–expressing EL4 cells before and after addition of 1 mM calcium. Excitation was at 430 nm. FI, fluorescence intensity; AU, arbitrary units (adapted from Mues et al., 2013).

An alternative activation sensor, which complements the Twitch1 sensor, has been developed (Pesic et al., 2013, Marangoni et al., 2013, Lodygin et al., 2013). T cell activation can be detected by analyzing sub-cellular localization of NFAT family. As it was described previously, upon T cell activation, the phosphatase calcineurin dephosphorylates NFAT and causes its nuclear translocation and the induction of

NFAT mediated gene transcription (Shaw et al., 1995). The NFAT1 protein, in particular, is a transcriptional factor that is expressed in most immune cells and is regulated by calcium signaling. In the non-activated T cells, NFAT is localized into the cytosol. However, upon TCR stimulation, NFAT rapidly translocates into the nucleus within only few minutes (Fig. 1.5.2B).

The highly conserved DNA-binding domain of NFAT (Macian, 2005) was deleted so as not to interfere with endogenous gene regulation (Aramburu et al., 1998). Next, a GFP-labeled, truncated variant of NFAT1 was applied in order to visualize T cell activation within the spinal cord (Pesic et al., 2013) (Fig. 1.5.2A). ΔNFAT-GFP translocation of autoreactive T cells was observed within the leptomeningeal area and after extravasation (Pesic et al., 2013, Lodygin et al., 2013). This activation signal occurs only within a few minutes after stimulation and does not necessarily demand a long-lasting contact. T cells with nuclear NFAT exhibit a reduced motility and are able to sequentially make contacts with meningeal phagocytes.
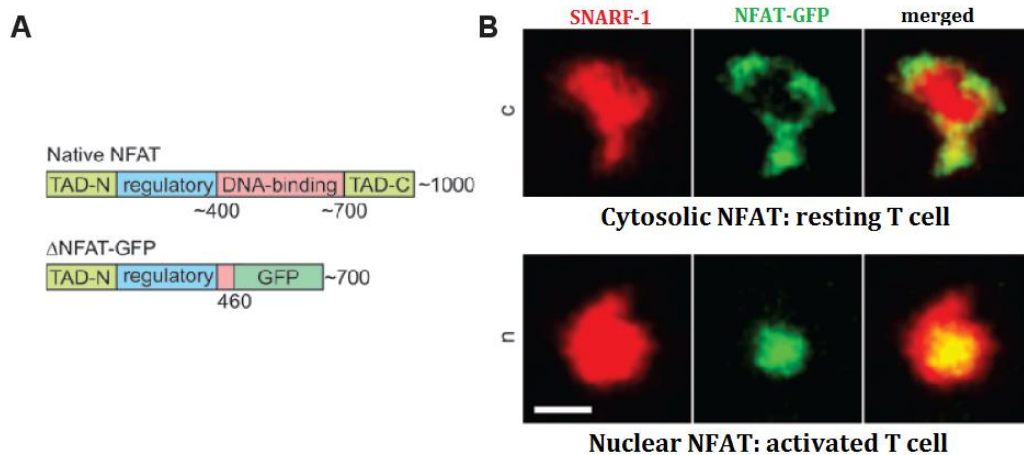
Figure 1.5.2 ΔNFAT-GFP as an activation marker of T cells. A. Native and truncated versions of NFAT. Amino acids numbers are indicated. TAD, transcription activation domain. B. *in vivo* T cell activation indicated by the cellular localization of the NFAT-GFP marker. Two patterns of NFAT-GFP (green)/SNARF-1 (red) in double-labeled T cells: cytosolic in resting cells and nuclear in activated T cells. Scale bar: 5µm (Adapted from Pesic et al., 2013).

OBJECTIVES

The main question addressed in this study was how symphonic infiltration of autoreactive T cells into the CNS is initiated. The experimental model that was applied was *t*EAE, which has proved to be a very important model in the study of MS. Although autoreactive T cells exist in healthy individuals and do not induce EAE, unknown trigger(s) stimulate autoreactive T cells and start infiltration into the CNS. In order to visualize autoreactive T cell activation *in vivo*, two newly developed activation reporters, Twitch and fluorescent NFAT were combined with *in situ* imaging by using two-photon microscopy.

The first aim of this study was to examine how T cells acquire a "migratory phenotype" in peripheral lymphoid organs. Since Twitch is a sensitive calcium sensing protein, it was speculated that it could detect weak signals such as the involvement of adhesion molecules and chemokine receptors.

The second aim of this study was to detect crawling-rolling transition calcium signals and record their strength and rhythm. Previous attempts to visualize the activation status of intraluminal ΔNFAT-GFP-expressing T cells during crawling and rolling were not successful. Most probably, the stimuli was not sufficient to translocate ΔNFAT-GFP to the nucleus.

In addition, it was important to quantify the frequency, the duration and the topography of calcium signaling of autoreactive T cells during antigen recognition in the spinal cord meninges. As of today, the majority of studies on calcium imaging have been performed in lymph nodes after providing excessive amount of antigen by immunization. In this study, it was speculated that the limited availability of immunogenic myelin proteins, even during the acute phase of EAE, would better reflect the physiological context of antigen recognition.

The last aim was to determine whether T cells accumulate calcium tonic signals from different APCs until a certain activation threshold is exceeded. For this reason, a new, dual Twitch and ΔNFAT sensor was generated.

MATERIAL & METHODS

2.1 Material

2.1.1 Bacteria

E. coli NEB 5-alpha Electrocompetent (NEB C2989K)

2.1.2 Oligonucleotides

Name	Sequence 5' →3'	Purpose
NFATdsRed2BglII	GATCAGATCTAGCTTCCACCATGGACGTCC	F2U-Δzeo-NFAT-DsRed2
NFATdsRed2NotI	GATCGCGGCCGCTACAGGAACAGGTGGTGG	F2U-Δzeo-NFAT-DsRed2
mRubyAgeIfw	GATAAACCGGTCGCCACCATGGTGTCTAAGGGCGAAGAGCTG	F2U-Δzeo-NFAT-mRuby2-ΔpolyA
mRubyNotIre	CTATAGGCGGCCGCTTACTTGTACAGCTCGTCCATCCCA	F2U-Δzeo-NFAT-mRuby2-ΔpolyA
NFATMfeIfw	GATAACAATTGAGCTTCCACCATGGACGT	PINCO-puro-ΔNFAT-mRuby2-Twitch2B
mRuby2MfeIre	CTATAGCAATTGAGGTCGAAAGGCCCGGA	PINCO-puro-ΔNFAT-mRuby2-Twitch2B
LSSmOrAgeIR	CTATAGACCGGTGCGGCCGCTTACTTGTACAGCT	pMSCV-ΔPGK-puro-ΔNFAT-LSSmOrange
LSSmOrAgeIF	GATAAACCGGTCGCCACCATGGTGAGCAAGGGC	pMSCV-ΔPGK-puro-ΔNFAT-LSSmOrange

Table 2.1.1 List of cloning primers.

2.1.3 Plasmids

Vector backbones	Purpose	Provider
pRSET-B	Expression vector	Invitrogen, Karlsruhe
pMSCVneo / pMSCVpuro	Retroviral vector	Clontech, Heidelberg
F2U-ΔZeo	Lentiviral vector	(kindly provided by Stefan Lichtenthaler Lab, DZNE)
PINCO	Retroviral vector	(Grignani et al., 1998)
pFusionRed	FusionRed fusion vector	(Shemiakina et al., 2012)

Table 2.1.2 List of vector backbones used in this study.

Name	Provider
pRSETB-LSSmOrange	(kindly provided by Oliver Griesbeck Lab, MPI)
pRSETB-mKate2	(kindly provided by Oliver Griesbeck Lab, MPI)
pRSETB-mRuby2	(kindly provided by Oliver Griesbeck Lab, MPI)
pMSCV-puro-ΔNFAT-GFP	(Pesic et al., 2013)
PINCO-GFP	(Grignani et al., 1998)
pMSCV-Δneo-Twitch1	(Mues et al., 2013)
pMSCV-Δneo-Twitch2B	(Thestrup et al., 2014)
pMSCV-neo-IRES-DsRed2	(Odoardi et al., 2007b)
pMSCV-puro-ΔNFAT-DsRed2	This study
F2U-Δzeo-NFAT-DsRed2	This study
pMSCV-puro-ΔNFAT-mKate2	This study
pRSETB-ΔNFAT-mKate2	This study
F2U-Δzeo-NFAT-DsRed2-ΔpolyA	This study
F2U-Δzeo-NFAT-mRuby2-ΔpolyA	This study
F2U-Δzeo-NFAT-FusionRed-ΔpolyA	This study
pMSCV-puro-ΔNFAT-mRuby2	This study
pMSCV-puro-ΔNFAT-FusionRed	This study
PINCO-Twitch1	This study
PINCO-Twitch2B	This study
PINCO-puro-ΔNFAT-mRuby2-Twitch2B (Proteas)	This study
pMSCV-ΔPGK-puro-ΔNFAT-LSSmOrange	This study

Table 2.1.3 List of subcloned plasmids used or constructed in this study.

2.1.4 Media, Reagents and Buffers

Bacterial growth media and buffers	Specified amount	Constituents
Luria-Bertani (LB)	10 g/l	Tryptone
	5 g/l	Yeast Extract
	10 g/l	NaCl
	100 µg/ml	Ampicillin was added for selection
Luria-Bertani (LB) Agar	10 g/l	Tryptone
	5 g/l	Yeast Extract
	10 g/l	NaCl
	15 g/l	Bacto Agar
	100 µg/ml	Ampicillin was added for selection
TAE running buffer	40 mM	Tris-HCl
	20 mM	Acetic acid
	1 mM	EDTA (pH 8.0)
DNA loading dye		R0611 (Thermo Scientific)
DNA ladder		1kb GeneRuler (Thermo Scientific)

Table 2.1.4 List of bacterial growth media and buffers used in this study.

Cell culture media, buffers and reagents	Specified amount	Constituents
DMEM	13.4 g/l	DMEM powder
	3.7 g/l	NaHCO$_3$
Freezing medium	50 % Vol.	Horse serum (inactivated)
	40 % Vol.	EH
	10 % Vol.	DMSO
EH	97.5 % Vol.	DMEM
	2.5 % Vol.	HEPES solution, 1M
Restimulation medium (RM)	99 % Vol.	TCM
	1 % Vol.	Rat serum
TCGF	80 % Vol.	TCM
	10 % Vol.	Horse serum (inactivated) Supernatant
	10 % Vol.	Supernatant from ConA stimulated mouse splenocytes
TCM	ad 1 l	DMEM
	2 mM	L-Glutamine
	10 IU/ml	Penicillin/Streptomycin
	10 ml/l	Asparagine
	1 mM	Sodium-Pyruvate
	10 ml/l	Non-essential amino acids
	4 µl/l	2-Mercaptoethanol
TCM + FCS	90 % Vol.	TCM
	10 % Vol.	Fetal calf serum (inactivated)
Phosphate buffered saline (PBS) Adjusted to pH 7.4	10 mM	Na$_2$HPO$_4$
	1.8 mM	KH$_2$PO$_4$
	140 mM	NaCl
	2.7 mM	KCl
Lysis buffer	150 mM	NH$_4$Cl
	1 mM	KHCO$_3$
	0.1 mM	Na$_2$EDTA
FACS buffer	99 % Vol.	PBS
	1 % Vol.	Rat serum
	0.05 % Vol.	NaN$_3$
Isotonic Percoll	90 % Vol.	Original Percoll
	10 % Vol.	10x PBS
Underlay Percoll	64 % Vol.	Isotonic Percoll
	36 % Vol.	PBS
CNS density gradient reagent	10.8 ml	Isotonic Percoll (1.124g/ml)
	10 ml	Underlay Percoll (1.077g/ml)
Blood lymphocyte gradient reagent	100 µl	Heparin (5000U/ml)
	0.63 ml for 5 ml blood	Optiprep
10x HBSS After bubbling with carbogen gas (95% O$_2$/5%CO$_2$), adjusted with NaHCO$_3$ to pH 7.	1368 mM	NaCl
	53 mM	KCl
	4.4 mM	KH$_2$PO$_4$
	55mM	Glucose
	3.3 mM	Na$_2$HPO$_4$
Ca^{2+} imaging buffer Adjusted to pH 7.4	140 mM	NaCl
	5 mM	KCl
	1 mM	MgSO$_4$ * 7 H$_2$O
	1 mM	CaCl$_2$
	1 mM	NaH$_2$PO$_4$ * H$_2$O

	5.5 mM	Glucose
	20 mM	HEPES
low-melting agarose solution		PBS
	3-4%	Low-melting Agarose
2x BES **Adjusted to pH 6.95**	50 mM	N,N-bis(2-hydroxyethyl)-2-aminoethanesulfonic acid
	280 mM	NaCl
	1.5 mM	Na_2HPO_4

Table 2.1.5 List of cell culture media, buffers and reagents used in this study.

2.1.5 Antibodies

Antibody (clone, isotype)	Host and specificity company	Applications
Isotope control **(MOPC31c)**	mouse AbD Serotec	Flow cytometry primary antibody
CD4 **(W3/25)**	mouse anti-rat AbD Serotec	Flow cytometry primary antibody
abTCR **(R73)**	mouse anti-rat AbD Serotec	Flow cytometry primary antibody
CD25 **(OX-39)**	mouse anti-rat AbD Serotec	Flow cytometry primary antibody
CD134 **(OX-40)**	mouse anti-rat AbD Serotec	Flow cytometry primary antibody
CD49d **(TA-2)**	mouse anti-rat AbD Serotec	Flow cytometry primary antibody
CD11a **(wt1)**	mouse anti-rat AbD Serotec	Flow cytometry primary antibody
CD45RC **(OX-22)**	mouse anti-rat AbD Serotec	Flow cytometry primary antibody
CD62L **(OX-85)**	mouse anti-rat AbD Serotec	Flow cytometry primary antibody
CD11b **(OX-42)**	mouse anti-rat AbD Serotec	Flow cytometry primary antibody
MHC class I **(OX-18)**	mouse anti-rat (in this study)	Flow cytometry / intravital imaging primary antibody
MHC class II **(OX-6)**	mouse anti-rat (in this study)	Flow cytometry / intravital imaging primary antibody
Allophycocyanin (APC) IgG	Goat anti-mouse Jackson Laboratories	Flow cytometry secondary antibody
IFNγ **(DB-1)**	mouse anti-rat eBiosciences	Flow cytometry primary antibody
IL-17 **(TC11-18H10)**	PE-conjugated rat anti-mouse BD	Flow cytometry primary antibody
Isotype control **(Rat, IgG1, k)**	PE-conjugated rat antibody BD	Flow cytometry primary antibody

Table 2.1.6 List of antibodies used in this study.

2.1.6 Antigens

MBP was prepared from guinea pig brain homogenates as reported (Campbell et al., 1973). OVA was purchased from Sigma-Aldrich, Taufkirchen.

2.1.7 Animals

Lewis rats (body weight 100-150 g) were obtained from the breeding colony of the Max Planck Institute of Neurobiology. All animals were kept and bred in the animal facility at the Max Planck Institute of Neurobiology. All of the animal experiments were approved by the local authority (Regierung von Oberbayern).

2.2 Methods

2.2.1 DNA techniques

in silico **DNA analysis.** Plasmid maps were drawn with Snap Gene Viewer Version 2.8.3 (GSL Biotech, Chicago, USA); restriction enzyme digestions were designed using NEBcutter 2.0 (NEB, Frankfurt) and Snap Gene Viewer Version 2.8.3.

PCR primers. Oligonucleotide primers were designed with Snap Gene Viewer Version 2.8.3. All DNA oligonucleotides were synthesized by Metabion (Planegg/Steinkirchen, Germany) and reconstituted in sterile, deionised water to give a stock solution of 100 µM.

DNA sequencing. The sequencing was conducted by the Sequencing Service of the Genomics Service Unit in Faculty of Biology (LMU, Martinsried) using an ABI 3730 capillary sequencer. DNA sequencing results were analyzed by Snap Gene Viewer Version 2.8.3 and sequence alignment was done by ClustalW (EMBL-EBI, Cambridge, UK).

DNA modification. DNA was modified with enzymes using standard protocols provided by the manufacturers (NEB, Frankfurt; MBI Fermentas, St. Leon-Rot).

Plasmid purification. DNA purification was done with glycogen from *Mytilus edulis* (G1767) using a standard protocol provided by the manufacturer (Sigma-Aldrich, Taufkirchen).

Polymerase Chain Reaction (PCR). All PCR assays were performed using iProof High –Fidelity Master Mix (Bio-Rad, Hercules, USA) in 50 µl reactions according to the instructions of the manufacturer. The optimal

annealing temperature for each pair of primers was determined by temperature gradient PCRs. Thermal cycles were performed using a PTC-200 DNAEngine (Bio-Rad, Hercules, USA) cycler.

DNA purification. PCR products or DNA fragments were purified by the QIAquick PCR Purification Kit (Qiagen, Hilden) according to the instructions of the manufacturer. The DNA concentration was determined by using the Nanodrop spectrophotometer ND-100 (PeqLab, Erlangen).

Agarose gel electrophoresis. The agarose gels were prepared by boiling agarose 1.0% (w/v) in 1 x TAE and adding 1 μg/ml ethidium bromide. DNA was separated at 120 volts for 90 min. Gels were visualised in the Geldoc XR system (Bio-Rad, Hercules, USA). An IL 200 M transilluminator (Bachofer, Reutlingen) was used in order to excise DNA bands from preparative gels.

DNA extraction from agarose gels. DNA fragments were excised from agarose gels and DNA was isolated using the Wizard SV Gel Clean-Up System (Promega, Mannheim) according to the instructions of the manufacturer.

Ligation of DNA fragments. Vector backbone and insert were mixed in molar ratios of 1:3 to 1:5. The ligation reaction was performed using T4 DNA ligase (NEB, Frankfurt) following manufacturer's instructions. The fragments were ligated in a total volume of 20 μl T4 DNA ligase buffer using 400 units T4 DNA ligase for 1 hour at RT or for 12 hours at 18°C. The ligase was deactivated by heating at 65°C for 20 minutes.

Electroporation of _E. coli_. Electrocompetent _E. coli_ were thawed slowly on ice. Cell suspension was mixed gently to resuspend, and returned to the ice. 1 μl DNA and 50 microliters of cells were transferred to a chilled electroporation cuvette, and transfected using the GenePulser (Bio-Rad, Hercules, USA) at 25 μF, 1.7 kV, and 200 Ω. After electroporation the bacteria were immediately transferred to 500 μl LB medium agitated for 30 min at 37°C. 200 μl of cell suspension were plated onto LB agar plates containing antibiotic selection and incubated at 37°C o/n.

E. coli glycerol stock. 500 μl of an overnight culture was mixed with 500μl of 50% glycerol solution and stored in cryotubes at -80°C.

Isolation of plasmid DNA from _E. coli_. Plasmid DNA was isolated with the HiSpeed Plasmid Midi Kit (Qiagen, Hilden) or with the NucleoBond Xtra Midi (Macherey-Nagel, Düren) according to the instructions of the manufacturers. DNA was always eluted in H_2O.

2.2.2 Cloning strategies

PINCO-Twitch1 and PINCO-Twitch2B

The reported PINCO-GFP vector was digested with *BspQI* and blunt ends were generated using a T4 DNA polymerase. Subsequently, the vector was further digested with *SspI* and *EcoRI* to substitute the sequence between the two long terminal repeats (LTRs) with the LTRs and the *Twitch2B* from the pMSCV-Δneo-Twitch2B vector. *Twitch2B* including the LTRs was excised from the pMSCV-Δneo-Twitch2B vector by restriction digestion with *SspI*. Pinco-Twitch1 was generated with a similar cloning strategy (Fig. 2.2.1).
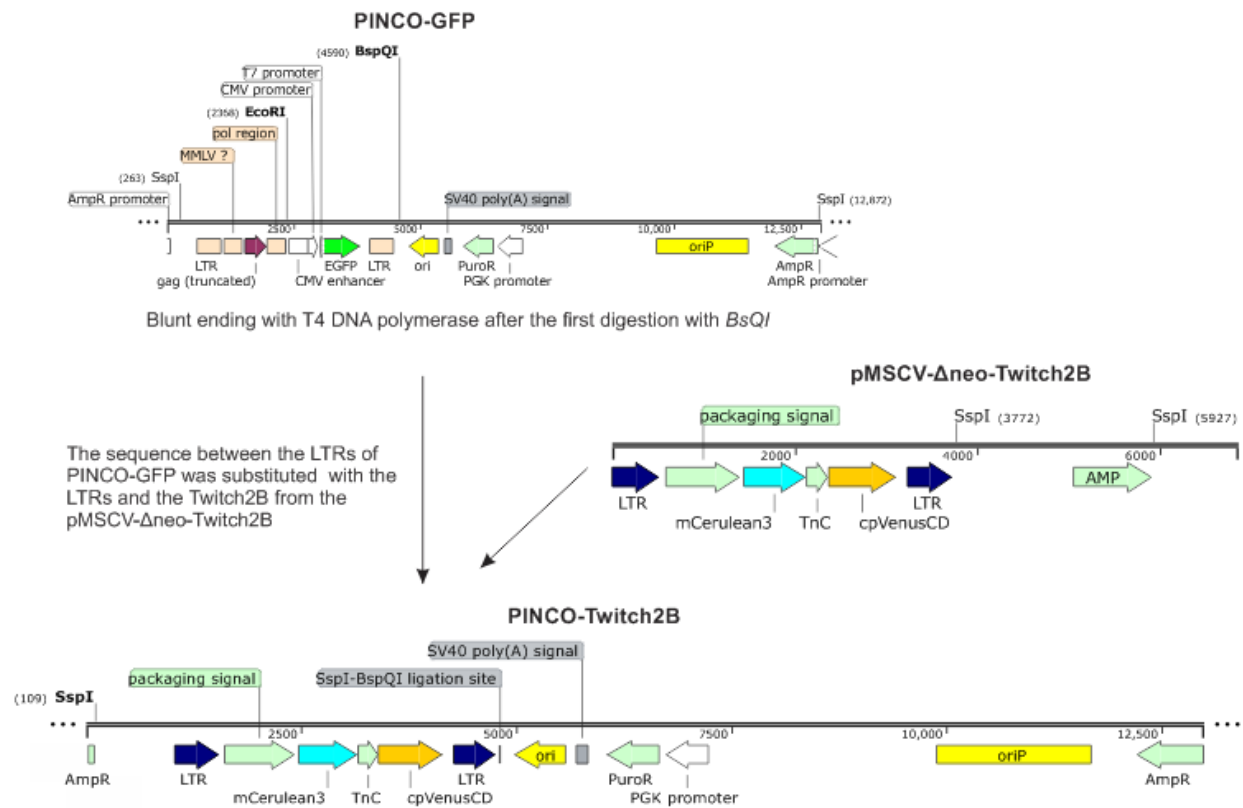
Figure 2.2.1 A. Schematic representation of cloning strategy for constructing PINCO-twitch2B plasmid. PuroR: puromycin resistance gene; ori: origin of replication.

pMSCV-puro-ΔNFAT-DsRed2

The pMSCV-neo-IRES-DsRed2 and pMSCV-puro-ΔNFAT-GFP vectors were digested with *AgeI*. Then, *DsRed2* and 120 bp from the beginning of the phosphoglycerate kinase (PGK) promoter were excised and exchanged with the sequence of *GFP* and part of the PGK promoter in pMSCV-puro-ΔNFAT-GFP vector. Importantly, the open reading frame (ORF) of ΔNFAT-DsRed2 was continuous and maintained the same as ΔNFAT-GFP (Fig. 2.2.2A).

25

F2U-Δzeo-NFAT-DsRed2

ΔNFAT-DsRed2 was cloned into the lentivirus F2U-ΔZeo plasmid. PCR based cloning was performed with NFATDsRed2BglII and NFATDsRed2NotI primers (see table 2.1.1). These primers added *BglII* and *NotI* restriction sites to the ends of *ΔNFAT-DsRed2* fragment. After digestion, this fragment was cloned into the *BamHI-NotI* digested F2U-ΔZeo plasmid (Fig. 2.2.2B).
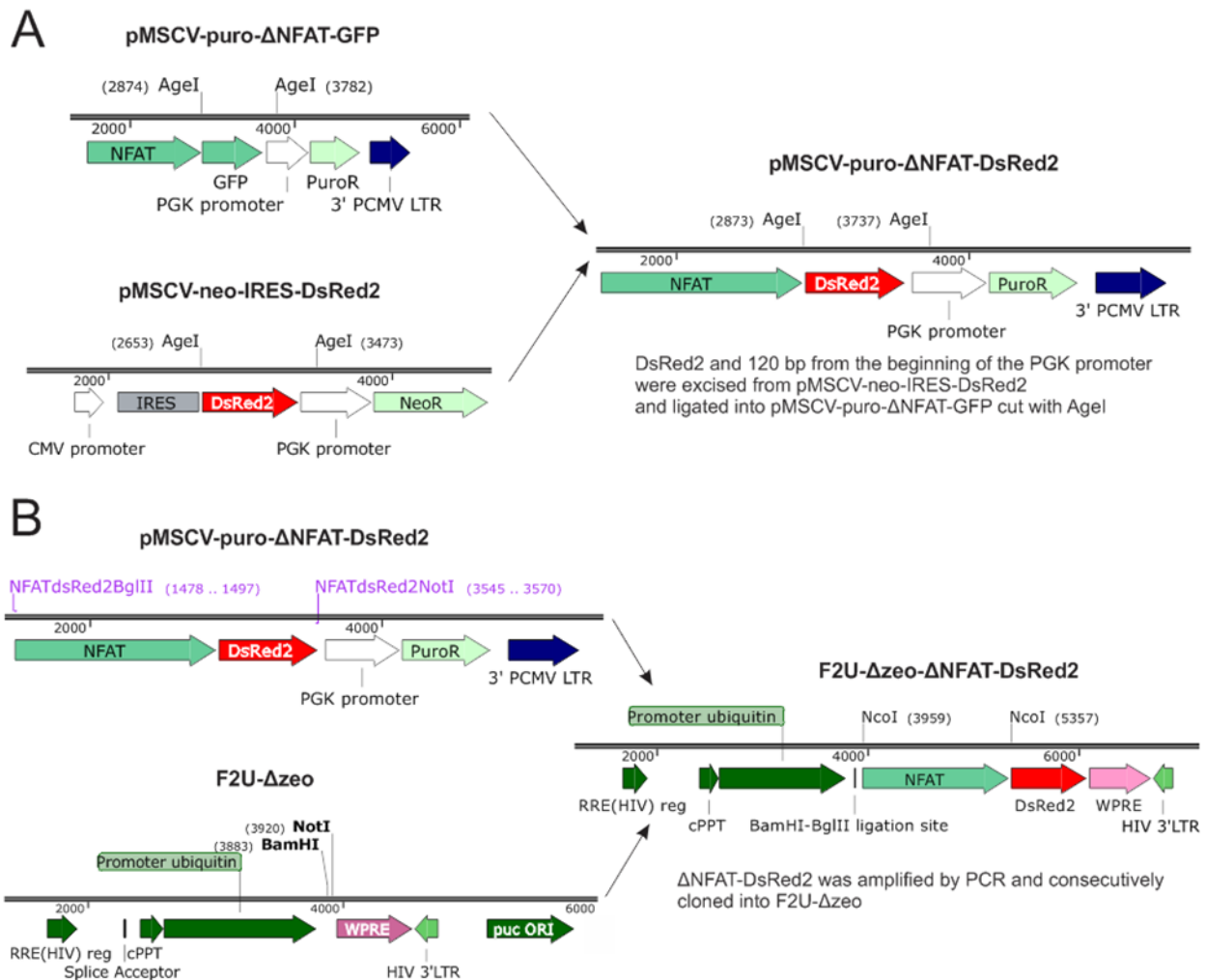
Figure 2.2.2 A. Schematic representation of cloning strategy for constructing pMSCV-puro-ΔNFAT-DsRed2 plasmid. B. Schematic representation of cloning strategy for constructing F2U-Δzeo-NFAT-DsRed2 plasmid. IRES: internal ribosome entry site; RRE: Rev Response element; cPPT: central polypurine tract; WPRE: Woodchuck Hepatitis Virus Posttranscriptional Regulatory Element.

pMSCV-puro-ΔNFAT-mKate2

The pMSCV-puro-ΔNFAT-GFP vector was digested with *NcoI*. *ΔNFAT* was excised and ligated upstream of *mKate2* into the pRSETB-mKate2 vector. Then, the donor pRSETB-ΔNFAT-mKate2 and the recipient pMSCV-puro-ΔNFAT-GFP vectors were digested with *EcoRI*. During the final cloning step, 291 bp

from the end of Δ*NFAT* and *mKate2* were excised and exchanged with the sequence of *GFP* and the identical area of Δ*NFAT* in the pMSCV-puro-ΔNFAT-GFP vector (Fig. 2.2.3).
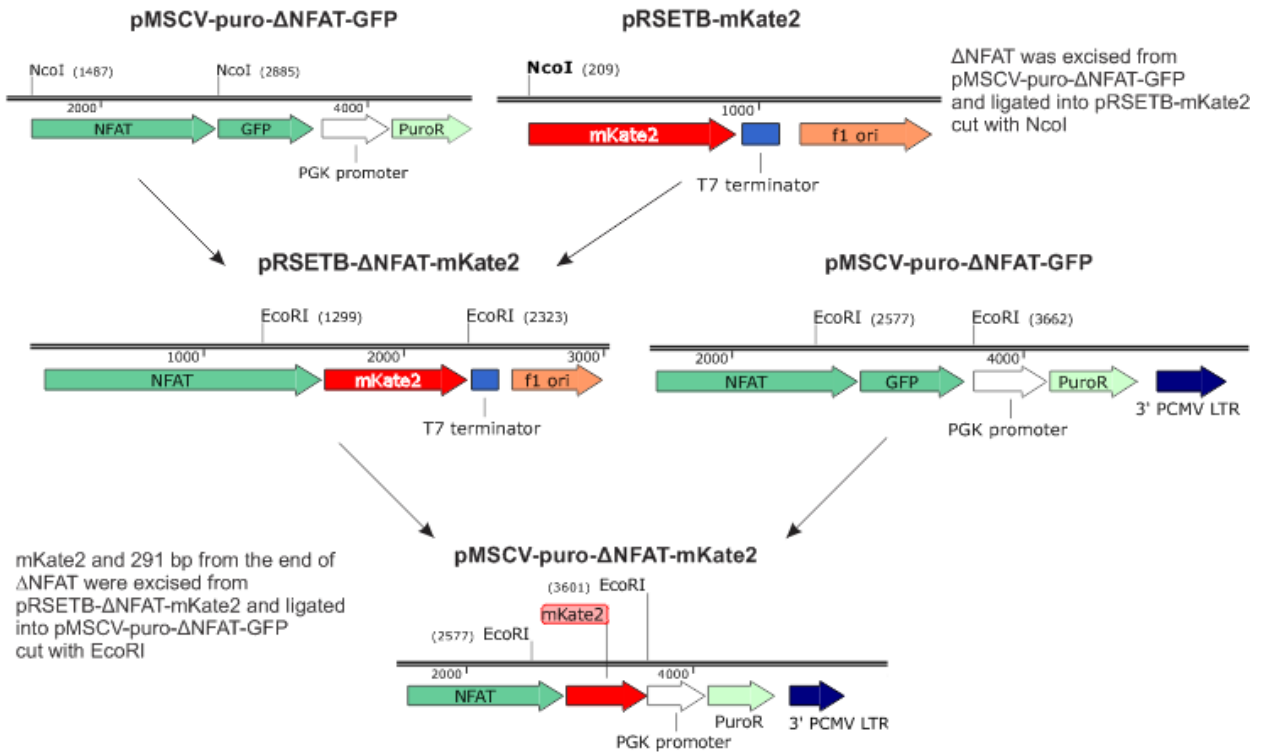
Figure 2.2.3 Schematic representation of cloning strategy for constructing pMSCV-puro-ΔNFAT-mKate2 plasmid.

pMSCV-puro-ΔNFAT-mRuby2 & pMSCV-puro-ΔNFAT-FusionRed

The same cloning strategy was followed in order to generate the ΔNFAT-mRuby2 and ΔNFAT-FusionRed vectors. Both FPs were cloned downstream of the ORF of the *NFAT* gene into the lentivirus F2U-Δzeo-NFAT-DsRed2-ΔpolyA plasmid. *mRuby2* was amplified from the pRSETB-mRuby2 plasmid by PCR. The applied primers mRubyAgeIfw and mRubyNotIre (see table 2.1.1) added *AgeI* and *NotI* restriction sites to the ends of mRuby2 fragment. FusionRed was digested with *AgeI* and *NotI* from the pFusionRed vector and cloned directly to the aforementioned lentivirus vector. Next, the F2U-Δzeo-NFAT-mRuby2-ΔpolyA, F2U-Δzeo-NFAT-FusionRed-ΔpolyA and pMSCV-puro-ΔNFAT-GFP vectors were digested with *BamHI* and *NotI*. During the final cloning step, 424 bp from the end of Δ*NFAT* and *mRuby2/FusionRed* were excised and exchanged with the sequence of *GFP* and the identical area of Δ*NFAT* in the pMSCV-puro-ΔNFAT-GFP vector (Fig. 2.2.4).
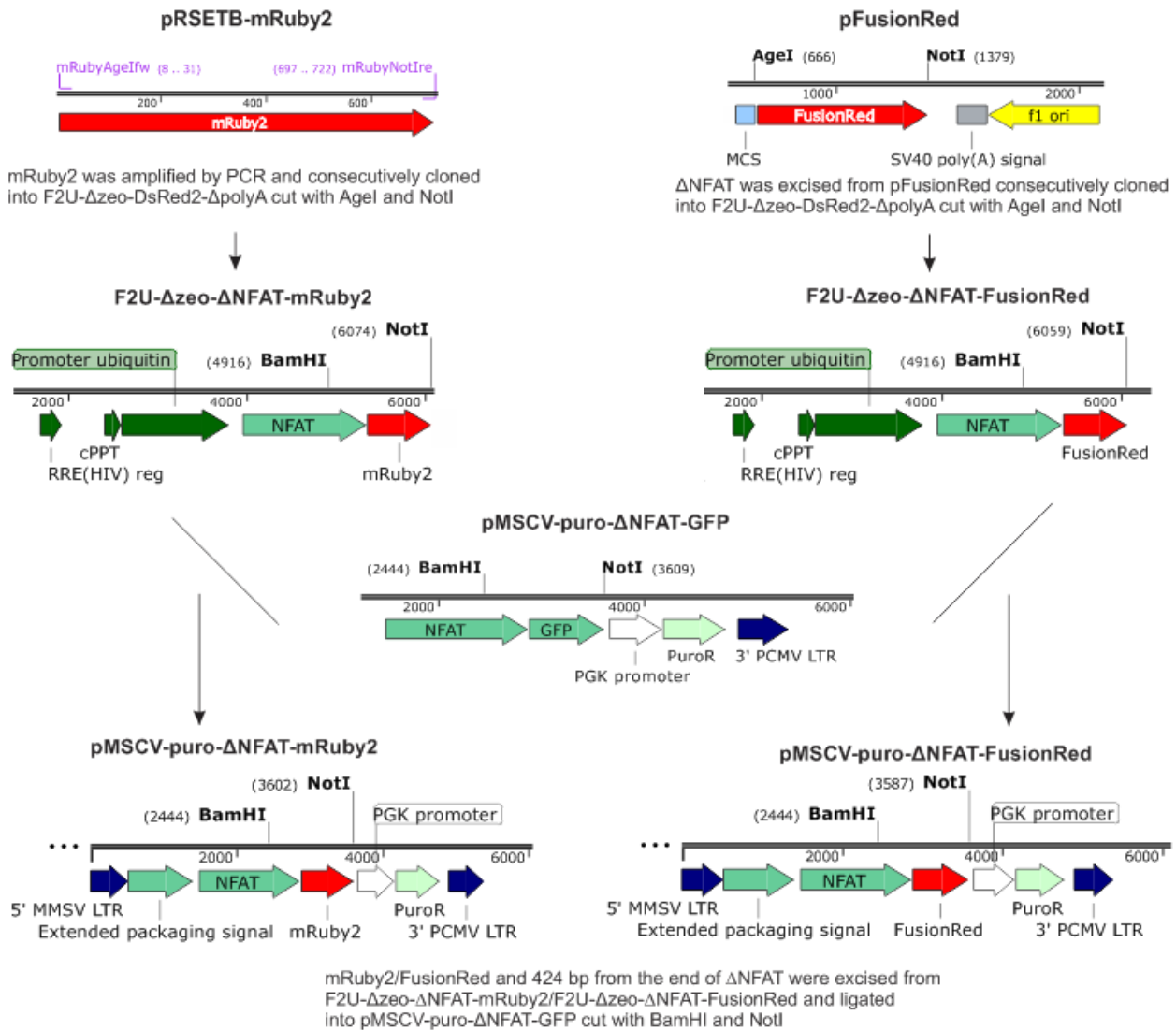
Figure 2.2.4 Schematic representations of cloning strategies for constructing pMSCV-puro-ΔNFAT-mRuby2 and pMSCV-puro-ΔNFAT-FusionRed plasmids.

pMSCV-ΔPGK-puro-ΔNFAT-LSSmOrange

LSSmOrange was amplified from the pRSETB-LSSmOrange plasmid by PCR. The applied primers LSSmOrAgeIR and LSSmOrAgeIF (see table 2.1.1) added *AgeI* restriction sites to the ends of *LSSmOrange* fragment. The pMSCV-puro-ΔNFAT-mRuby2 vector was digested with *AgeI* and the *mRuby2* was exchanged with the sequence of *LSSmOrange* (Fig. 2.2.5).
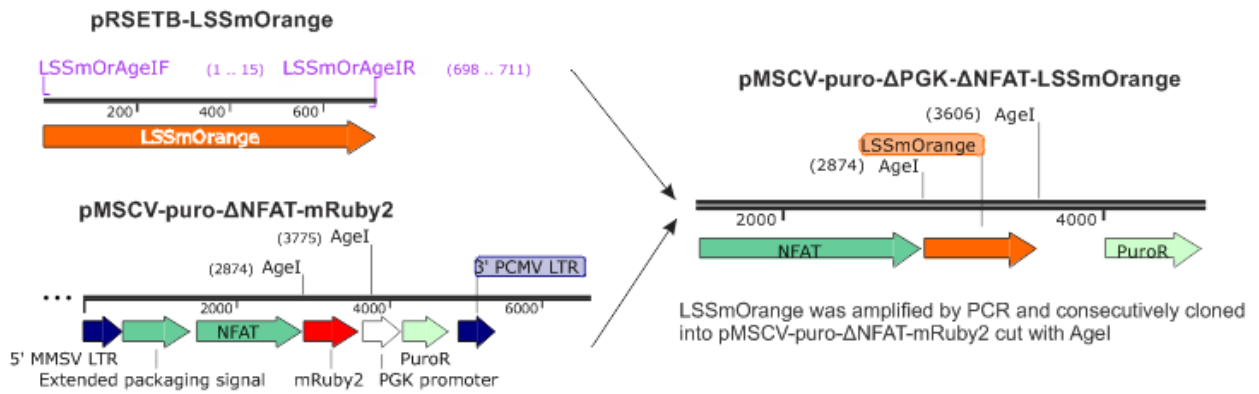
Figure 2.2.5 Schematic representation of cloning strategy for constructing pMSCV-ΔPGK-puro-ΔNFAT-LSSmOrange plasmid.

PINCO-puro-ΔNFAT-mRuby2-Twitch2B (Proteas)

To generate the PINCO-puro-ΔNFAT-mRuby2-Twitch2B (Proteas) vector, PCR based directional cloning was performed. At first, the PINCO-Twitch2B vector was digested with *EcoRI*. ΔNFAT-mRuby2 and PGK promoter were amplified from the pMSCV-puro-ΔNFAT-mRuby2 vector by PCR. The applied primers NFATMfeIfw and mRuby2MfeIre (see table 2.1.1) added *MfeI* restriction sites to the ends of *ΔNFAT-mRuby2* fragment. The ligation of the PINCO-backbone and the *ΔNFAT-mRuby2* targeted insert was achieved with compatible cohesive ends (Fig. 2.2.6).
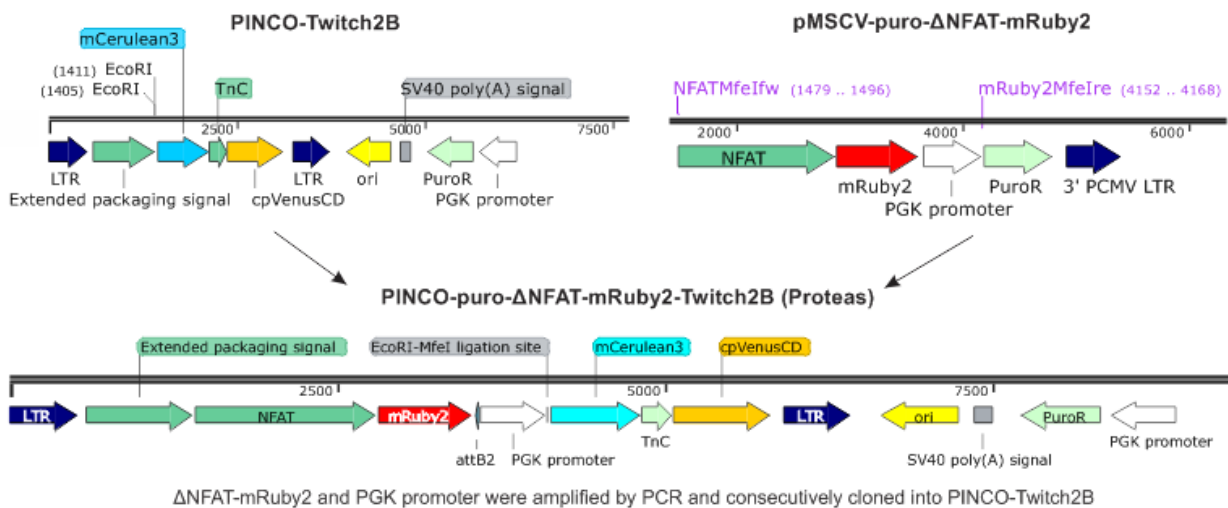
Figure 2.2.6 Schematic representation of cloning strategy for constructing PINCO-puro-ΔNFAT-mRuby2-Twitch2B (Proteas) plasmid.

2.2.3 Cell culture

Cultivation of cell lines. Cell lines were checked daily to confirm they are growing as expected. They were cultivated in fully complemented DMEM medium in standard cell culture-treated plastic dishes (BD, Heidelberg) in a humidified incubator (Heraeus) at 37°C and 10% CO_2. Adherent cells that required trypsinization, were treated with Trypsin-EDTA (PAA Laboratories) for 3-5 min at 37°C. In general, cultures were split when they were 80% confluent. Fresh media was added to cell cultures when they were not confluent in order to keep correct pH and replenish nutrients. Cells were pelleted by centrifugation at 300 rcf for 7 min at 4°C.

Cryopreservation of cell lines. For long-term storage of cell lines, $15\text{-}30\times10^6$ healthy cells with a viability of >90% were harvested and resuspended in 1.5 ml of freezing medium. Slow freeze was achieved by storing the cell lines in a dedicated Freezing Container (Thermo Fisher Scientific) at -80°C and subsequently in a liquid nitrogen tank. Cell lines were thawed quickly by incubation in a 37°C water bath for 3-5 minutes and washed once with 10 ml of EH to remove the cryoprotectant DMSO. Afterwards, cell lines were resuspended in 10 ml of warm medium.

Calcium phosphate transfection of GP+E86 cells. Twenty-four hours prior to transfection, 2×10^6 GP+E86 cells were inoculated per 10 cm culture dish in 10 ml TCM + FCS. The following day, 25 µM chloroquine (Sigma-Aldrich, Taufkirchen) was added to the medium. Next, a transfection mix was made by mixing 15-20 µg DNA in 900 µl H_2O and 50 µl 2 M $CaCl_2$. 1 ml of 2x BES was added dropwise while aerating by vortex. After 20 min incubation at 37°C the transfection complex was transferred dropwise onto the GP+E86 cells. Twelve to sixteen hours after incubation, the medium was aspirated gently and was replaced with 10 ml of pre-warmed fresh medium.

Lentivirus production and transduction. Lentivirus production and transduction was generated using the method of Kuhn et al. (Kuhn et al., 2010). Cell cultures were performed in a BSL 2 containment facility and according to work practices. However, due to technical reasons, all experiments were kindly performed by Stefan Lichtenthaler's Lab (DZNE).

Generation of retrovirally transduced, antigen-specific T cell lines. A previous reported protocol (Flügel et al., 1999) was applied in this study for generating antigen-specific T cell lines; some essential modifications were implemented regarding the Twitch1 fluorescent protein. 6-8 week old Lewis rats were immunized by subcutaneous injection of antigen (100 µg), emulsified in complete Freund's adjuvant (CFA, Difco) containing the *Mycobacterium tuberculosis* strain H37RA (4 mg/ml). 10 days after immunization,

cells from the draining lymph nodes were isolated and co-cultured with monolayers of GP+E86 cells which produce a Twitch1 gene-coding retrovirus. The mixing ratio of T cells to GP+E86 cells was 2×10^6 cells/ml to 1.5×10^5 cells/ml. Importantly, GP+E86 cells were cultured a few hours before adding T cells in order to adhere. Next, cells were transferred to a 96-well round-bottom plate in a total volume of 100µl RM containing 10µg/ml antigen. The selection process includes antibiotic resistance via retroviral gene delivery and antigen presentation. Two days later, IL-2 conditioned medium (TCGF) was added for expanding and maintaining selected cells. On day 6, T lymphocytes were either stored by cryopreservation or further restimulated. During the next round of restimulation, T cells were incubated with irradiated (5000 rad) syngeneic thymocytes in the presence of antigen. Twitch1-labelled T cells were enriched by flow cytometric sorting using a MoFlow (Dako, Hamburg) or a FACS Aria (BD). The transduced T cells were selected after the first restimulation by neomycin (400 µg/ml) only if the vector contained a neomycin resistance gene. The expression of Twitch1 was confirmed by fluorescence microscopy using an inverted Axiovert 200M microscope (Zeiss Microscopy, Jena) equipped with a CoolSnap CCD camera (Roper Scientific, Planegg).

2.2.4 Flow Cytometry (FACS)

Surface staining. *in vitro* activated GFP- or Twitch1-labeled T cells (1×10^6 cells per staining) were incubated with FACS buffer in a 96-well V bottom plate (Nunc) for 10 min on ice to prevent nonspecific antibody binding. Next, primary antibodies were added at optimized dilutions for 30 min on ice followed by two times washing in FACS buffer. A secondary antibody was applied afterwards using the same protocol. Lastly, the cells were washed once in FACS buffer and once in PBS. Every washing step required a centrifugation at 300 rcf for 10 min at 4°C.

Intracellular staining. PMA (10µg/ml)/ionomycin (1µM) stimulated T cells were used as positive control. For intracellular stainings, cells were fixed in 2 % PFA for 20 min on ice. After incubation, cells were washed in PBS. After fixation, cells were permeabilized by incubation with BD Perm/Wash buffer on ice for 15 min. Every following washing step required BD Perm/Wash buffer. The primary antibody for IFNγ (diluted 1:200) was added and cells were incubated on ice for 30-60 min. After washing three times with BD Perm/Wash, cells were resuspended in BD Perm/Wash buffer with the secondary antibody (1:200 dilution) along with PE-IL-17 (1:400 dilution) antibody for 90 min on ice. Lastly, the cells were washed once with BD Perm/Wash and once with PBS.

All samples were measured by FACS VERSE (BD) and data analysis was performed using the FlowJo software (FlowJo LLC).

2.2.5 Animal experiments

Fentanyl anesthesia mixture. Animals were anesthetized by intramuscular injection of fentanyl/midazolam/medetomidin mix (5 µg/kg, 2 mg/kg and 150 µg/kg, respectively) in PBS according to Bavarian state regulations for animal experimentation and approved by the appropriate authorities.

Adoptive transfer EAE. Transfer EAE was induced by intravenous injection (i.v.) of *ex vivo* stimulated encephalitogenic T cells to 8-12 weeks old female Lewis rats. The number of injected T cell blasts depended on the experimental setup (Table 2.2.1). The animals were monitored for weight loss and clinical scores daily. Clinical evaluation was scored as follows: 0, no disease; 0.5, loss of tail tonus; 1, tail paralysis; 2, gait disturbance; 3, complete hind-limb paralysis; 4, tetraparesis; 5, death.

Experiment	T cells	Number of transferred T cells
Intravital imaging of Twitch1-labeled T cells in the spleen (3.1.2)	$T_{MBP-Twitch1}$ or $T_{OVA-Twitch1}$	4.0-5.0×10^6
Mechanisms of antigen independent calcium spikes (3.1.3)	$T_{MBP-Twitch1}$ or $T_{OVA-Twitch1}$	First transfer: 12.0-15.0×10^6 Retransfer: 10.0×10^6
Intravital imaging of Twitch1-labeled T cells within leptomeningeal vessels (3.1.4)	$T_{MBP-Twitch1}$ or $T_{OVA-Twitch1}$	3.0-5.0×10^6
Intravital imaging of Twitch1-labeled T cells within leptomeninges (3.1.5)	$T_{MBP-Twitch1}$ or $T_{OVA-Twitch1}$	Day 2: 3.0-5.0×10^6 Day 3: 2.6×10^6
Intravital imaging of Twitch1-labeled T cells within parenchyma (3.1.6)	$T_{MBP-Twitch1}$	2.6-8.0×10^6 (depends on the day of imaging)
Deciphering the relation between antigen stimulation and intracellular calcium signaling (3.1.7)	$T_{MBP-Twitch1}$ or $T_{OVA-Twitch1}$	2.6-3.2×10^6
Leptomeningeal APCs have disparate functional potential (3.1.8)	$T_{MBP-Twitch1}$ or $T_{OVA-Twitch1}$	2.6-3.5×10^6

Table 2.2.1 Number of transferred T cells depending on the experimental setup.

Retransfer after treatment with a chemokine receptor inhibitor. $T_{OVA-Twitch1}$ were prepared three days after adoptive transfer (Pesic et al., 2013). Cells from the spleen were homogenized in EH via metal filter and treated with lysis buffer to remove erythrocytes. Next, the lymphocytes were treated with chemokine/chemokine receptor inhibitors for 60 min before transfer to secondary recipient animals. During this step, the macrophages were also removed by adhesion on culture dishes. The following inhibitors were used: Pertussis toxin (PTX) (List Biological Laboratories, 100 ng/ml), Maraviroc (Sigma, 25

µg/ml), AMD-3100 (Sigma, 25 µg/ml), and TAK-779 (Sigma, 22 µg/ml). After treatment, 10 x 10^6 Twitch1-labelled T cells were washed with EH and retransferred into naïve recipients via the tail vein.

Intrathecal injection. Stereotactic intrathecal injection was performed into the cisterna magna of anesthetized rats. For labeling of meningeal APCs, 6 µg of Texas Red or tetramethylrhodamine conjugated dextran (molecular size: 70 kDa or 2 MDa respectively from Molecular Probes) was injected into the cisterna magna between C1 and C2 using a 27G needle (BD). Intrathecal application of 0.2-0.3 mg anti-MHC class II or anti-MHC class I blocking antibody was performed similarly.

Antibody production. Anti-MHC class I and anti-MHC class II antibody producing hybridoma lines were purchased from Sigma. Cells were cultured in serum free medium (Life technologies). Supernatant was harvested from an overgrown cell culture. The antibodies in the supernatant were concentrated by using a Centricon Plus-70 according to manufacturer's protocol. Antibody concentration was measured by Nanodrop.

2.2.6 Fluorescence microscopy

Fluorescent protein-labeled GP+E86 or HEK 293 cells were resuspended in calcium imaging buffer and incubated in cell culture dishes at 37°C for at least one hour. Time lapse video microscopy was performed at controlled temperature and CO_2 conditions. Image acquisition in 30-s time intervals started before ionomycin treatment (4 µM) and continued for at least 13 min after stimulation. Time-lapse images were acquired on an inverted Axiovert 200M microscope (Zeiss Microscopy, Jena) equipped with a 37°C incubation chamber. Images were processed by MetaMorph software (Molecular Devices) and analyzed using ImageJ software (NIH).

2.2.7 Intravital two-photon microscopy

Animal preparation. Animals were anesthetized with isoflurane and subsequently with fentanyl anesthesia mixture. Next, they were intubated by tracheotomy and ventilated with 1.0-1.3% isoflurane. Importantly, isoflurane was supplied continuously during the whole imaging session. Animals were stabilized on a custom-made microscope stage and the body temperature was regulated by a heated pad (37.5°C). Electrocardiograms were recorded by electrocardiogram sensors on both forefeet, and physiological parameters, such as concentrations of inspiratory and expiratory gases, and ventilation pressure were constantly recorded during imaging.

Spinal cord imaging. For spinal cord imaging, laminectomy was performed at the upper part of lumber spinal cord (Bartholomäus et al., 2009). After midline skin incision of 2–3 cm, the paravertebral musculature was detached from the spine and a laminectomy on one spine disc was performed using a dental drill (Foredom, Bethel, USA). To exclude artifacts by the preparative disclosure of the spinal cord tissue as well as by the heart beat and breathing of the animal, 3 sequential spine discs were fixed using a custom made fixation. The water objective was embedded in a ring-shaped dam surrounding the spinal cord window built by using a low-melting agarose solution. Blood vessels and CNS meningeal APCs were visualized by intravenously and intrathecally respectively injected fluorescent dextran conjugates.

Spleen imaging. For spleen imaging, a skin incision was made and the spleen was gently exposed with intact vasculature on a custom-made stage. Wiring of blood vessels and spleen was allowed through a small opening between the stage and the animal. To exclude artefacts, a glass bottom µ-Dish (Ibidi, Martinsried) was carefully placed on the top of the spleen and pressed slightly.

Acute slice imaging. Spinal cord was excised from the T-cell-transferred animal at the acute phase of EAE. A tissue chopper was used for cutting the spinal cord into transversal 300µm-thickness slices. Slices were kept in ice-cold HBSS bubbled with carbogen gas ($95\%O_2/5\%CO_2$) and adjusted to pH 7. Next, the slices were placed at the bottom of a custom made chamber and stabilized with a slice anchor. Importantly, the slice anchor had the same thickness as the acute slice in order to stabilize it against the buffer flow and not to compress it. A buffer circulation at 37°C and bubbled with carbogen was critical for the T-cell motility. Dead cells, which may have been injured during slice preparation, were excluded from the analysis using low-dose (5 µg/ml) DAPI staining.

Image acquisition. Images were acquired by using Leica SP2 (Leica, Mannheim) equipped with a 10W Millenia/Tsunami pulsed laser (Newport Spectra Physics, Darmstadt). Typically, 260 µm x 260 µm x 30 µm xyz-volume was imaged with 512 x 512 x 10 pixels with time interval of 19-21 sec. Imaging was done with 2x zoom and with images line-averaged twice. Laser was adjusted to emit 835 nm excitation beam. The fluorescent signal was collected with water immersion objective (25x, NA 0,95) and detected by non-descanned detectors equipped with 475/50 nm (CFP), 537/26 nm (FRET), and 630/69 nm (Texas Red) band-pass filters (Semrock).

Image processing. Images were processed using ImageJ. To obtain two-dimensional movies, a Gaussian blur filter was applied and maximum intensity z-projections were made. Additionally, a Median filter was used for removing noise. Artifacts from focal drift were removed using the StackReg/TurboReg plugin.

Image analysis. Images were analyzed using ImageJ and the computing of motility parameters and calcium signals was performed using Excel (Microsoft). At each time point, the cell shape was outlined manually in the maximum projection picture. Cell coordinates were obtained for calculating the cellular motility and generating cell trajectories. The latter were aligned accordingly for the starting position.

Calculation of calcium signals. Intracellular calcium measurement in single cells was performed using the ratiometric calcium sensor Twitch1. The emission from CFP (CFP) and CpCititine (FRET) after CFP excitation was acquired. The bleed-through of CFP into the FRET channel was determined to be 44%, and the FRET signal for CFP bleed-through was corrected as cFRET = FRET − 0.44 × CFP. The ratio of cFRET/CFP was normalized as previously (Mues et al., 2013). Ratio was calculated as $\Delta R/R = (R - R_0)/R_0$ (R, actual ratio; R_0, ratio at zero calcium). Ratiometric pseudocolor pictures were created according to the normalized formula and a fire lookup table was applied.

Calculation of T cell-APCs interactions. Regions of interest (ROIs) that include the outline cell shape from both T cells and APCs were automatically crosschecked in ImageJ, and any overlap or bordering of the ROIs within 0.9375 µm was considered as a contact. A tolerance of one pixel was added to every ROI containing APCs. Because of the fact that the dendrites of the APCs were too delicate to be visualized in detail, the interruption of a contact over one time point was considered as a continuing contact.

2.2.8 Statistical analysis

For all statistical tests, Prism software (Graphpad) was used as described in the figure legends. Significance was indicated according to the p-value as the following: *$p<0.05$, **$p<0.01$, ***$p<0.001$. The scatter plots were constructed using R. The overlaid box plots extend from the twenty-fifth to the seventy-fifth percentiles and the whiskers extend from the fifth to the ninety-fifth percentiles.

RESULTS

3.1 Context-dependent calcium signaling in encephalitogenic T cells

3.1.1 Establishing Twitch1-labeled T cells

Fluorescent protein-labeled rat T cells can be established by applying simultaneous strong positive and negative selection pressures on them (Flügel et al., 1999). However, Twitch1 gene transfer into rat antigen specific T cells was initially not successful because the transduction efficiency was extremely low. It was speculated that two main factors may constrain the expression of Twitch1 into rat T cells; the size of the RNA packed into the retrovirus and the PGK promoter. Indeed, the sequence between the LTRs of the pMSCVneoTwitch1 plasmid is 2984 bp and reaches the upper limit of packaging capacity (Fig. 3.1.1A). In addition, the retroviral construct possesses two ORFs leaded by two different promoters. The ORF of Twitch1 is expressed only by the LTR promoter on the 5' end while the ORF of the Neomycin resistance cassette (NeoR) follows a strong PGK promoter. This unbalanced transcription may decrease Twitch1 expression and may enhance antibiotic resistance as well.
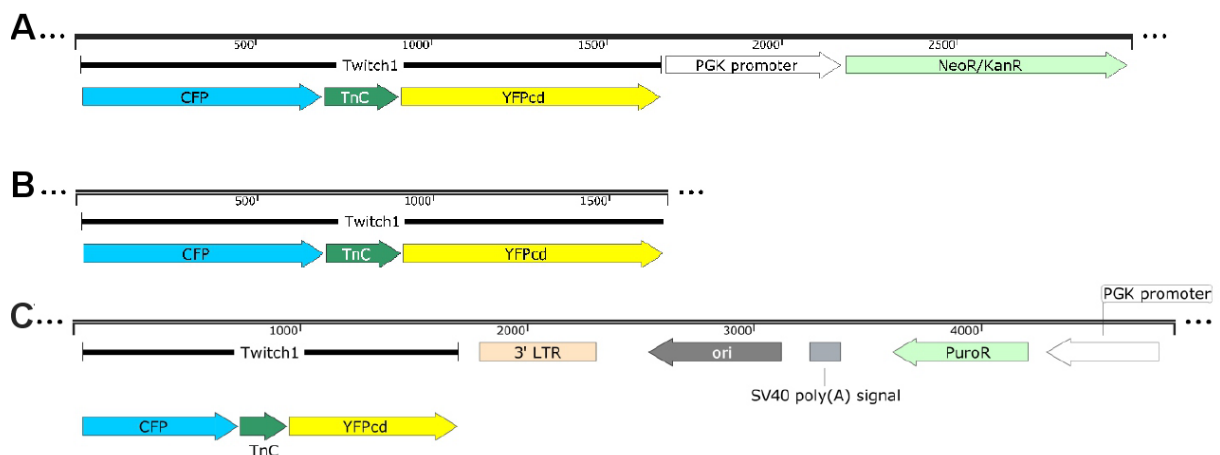
Figure 3.1.1 Twitch1 retroviral constructs. The elements of each construct are shown here. A. pMSCVneoTwitch1 B. pMSCVΔneoTwitch1 C. PINCOpuroTwitch1.

In order to increase the packaging efficiency, the size of the retrovirus was reduced by 1.3 kbp after deleting the neomycin resistance gene and the PGK promoter (Fig. 3.1.1B). However, this deletion led to a low transduction efficiency again because it was not possible to select the GP+E86 cells which produce viruses. Based on these findings, a PINCO vector was used (Grignani et al., 1998). This vector possesses a NeoR outside the LTRs and provides antibiotic resistance to transfected packaging cells. Consequently, it offers a smaller RNA size (Fig. 3.1.1C). Indeed, this modification, combined with sorting by FACS, achieved

a high efficiency gene delivery and allowed a high yield isolation of pure Twitch1-labeled T cell lines. Afterwards, T cell lines were expanded for more than 7 rounds of restimulation and it was shown that they managed to maintain Twitch1 expression in high levels (Fig. 3.1.2).

It should be mentioned that since the intracellular calcium binds to Twitch1, a high expression level of this sensor may possibly disturb some cellular functions. That was not observed in mouse T cells (Mues et al., 2013). However, it is not clear if the rat T cells present the same behavior because the sensitivity of T cells can differ among the species. Therefore, it was important to examine whether T cellular functions remain intact from the expression of Twitch1 or not.
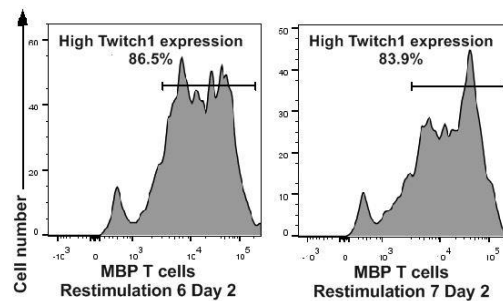
Figure 3.1.2 Representative flow cytometric histograms depicting Twitch1 expression levels in two different rounds of restimulation on day 2.

Flow cytometry confirmed that Twitch1 overexpression and calcium binding did not alter the T cell phenotype. MBP specific encephalitogenic T cells ($T_{MBP-Twitch1}$ cells) were compared with GFP-labeled counterparts and both of them showed similar expression patterns of cell surface molecules, including activation markers and adhesion molecules (Fig. 3.1.3A). Additionally, their intracellular production of inflammatory cytokines such as IFNγ and IL-17 was indistinguishable (Fig. 3.1.3B).

Next, encephalitogenicity and infiltration kinetics into the CNS were directly tested by adoptive transfer into the recipient animals. In comparison to previous studies (Pesic et al., 2013), Twitch1 expressing T cells behaved like their GFP or ΔNFAT-GFP expressing counterparts. Their encephalitogenic potential remained unimpaired (Fig. 3.1.3C-D), concluding that Twitch1 can be used as a reliable genetic indicator in rat T cells.
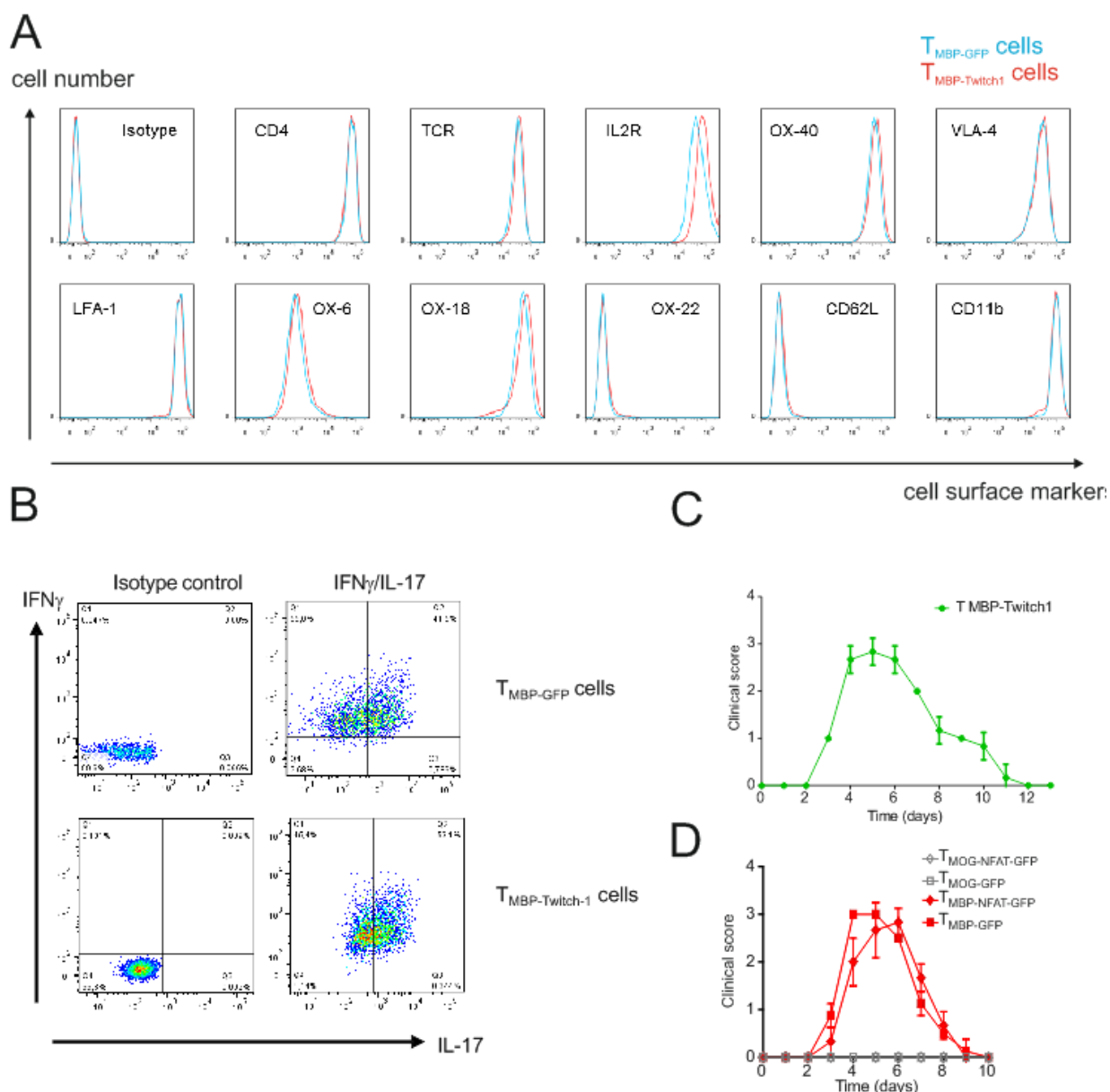
Figure 3.1.3 The phenotype of Twitch1-expressing T cells is compared with GFP-expressing T cells for cell surface markers (A) the production of inflammatory cytokines (B), and encephalitogenicity *in vivo* (C-D). A. The histograms depict the expression of cell surface markers on *in vitro*-activated GFP- or Twitch1-labeled T cells. T$_{MBP-GFP}$ (blue lines) and T$_{MBP-Twitch1}$ (red lines) cells were stained with specific antibodies as indicated and analyzed by flow cytometry. B. Dot plots of IFNγ/IL-17 intracellular staining. The inserted numbers indicate the proportion of cells in each quadrant. C-D. EAE clinical course induced by transfer of T$_{MOG-GFP}$ or T$_{MBP-GFP}$ cells as well as T$_{MOG-NFAT-GFP}$ or T$_{MBP-NFAT-GFP}$ cells and compared with EAE clinical course induced by transfer of T$_{MBP-Twitch1}$. A-D. Mean ± SD from at least 3 animals per group are shown. Representative data from 3 independent experiments per cell line (Figure D adapted from Pesic et al., 2013).

3.1.2 Intravital imaging of Twitch1-labeled T cells in the spleen

Determining a threshold for high-calcium levels

In the present work, OVA specific T cells ($T_{OVA-Twitch1}$ cells) were used as a negative control. After *in vitro* activation, both $T_{MBP-Twitch1}$ and $T_{OVA-Twitch1}$ cells were adoptively transferred into the recipient animal. They accumulated within the spleen on day 3 after adoptive transfer and they were imaged by intravital microscopy. It was speculated that the presence of tiny amounts of MBP would be sufficient to provide weak stimulation on T cells and would reveal the antigen dependency of calcium signaling into the spleen.

Regardless of the antigen specificity of T cells and behaving much like control $T_{OVA-Twitch1}$ cells, $T_{MBP-Twitch1}$ cells continuously moved through the spleen milieu, by sporadically firing brief calcium spikes. However, the calcium levels of both $T_{MBP-Twitch1}$ and $T_{OVA-Twitch1}$ cells remained below the threshold (Fig. 3.1.4).

In order to set a specific ΔR/R threshold for high-calcium signaling, a 95% percentile was used. This percentile represents 95% of all analyzed calcium values of T cells in the spleen. In contrast, the upper 5% percentile, which exceeded the threshold of ΔR/R: 1.282, belongs to high-calcium signaling.
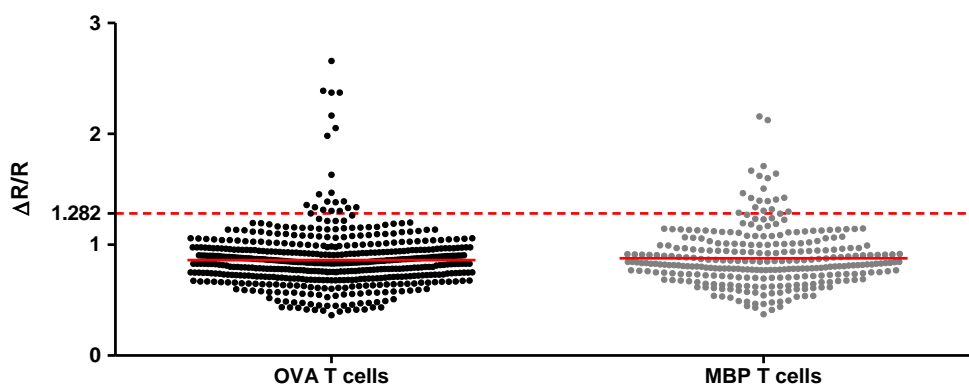
Figure 3.1.4 Twitch1-labeled T cells were imaged in the spleen on day 3 p.t. Cumulative plots of the calcium level (ΔR/R) are shown. Each dot represents a single time point in a particular cell. Hereafter, dotted horizontal lines (red) indicate the threshold (1.282) of the calcium level. Representative data from 2 independent experiments per cell line are shown.

Short high-calcium signaling in the spleen

Both $T_{MBP-Twitch1}$ and $T_{OVA-Twitch1}$ cells showed similarly infrequent and short-lasting calcium spikes. As reported before (Wei et al., 2007), and also in the present study, the majority of these calcium spikes were shorter than 2 minutes (Fig. 3.1.5A-B) and they were commonly associated with lower motility (Fig. 3.1.5C).
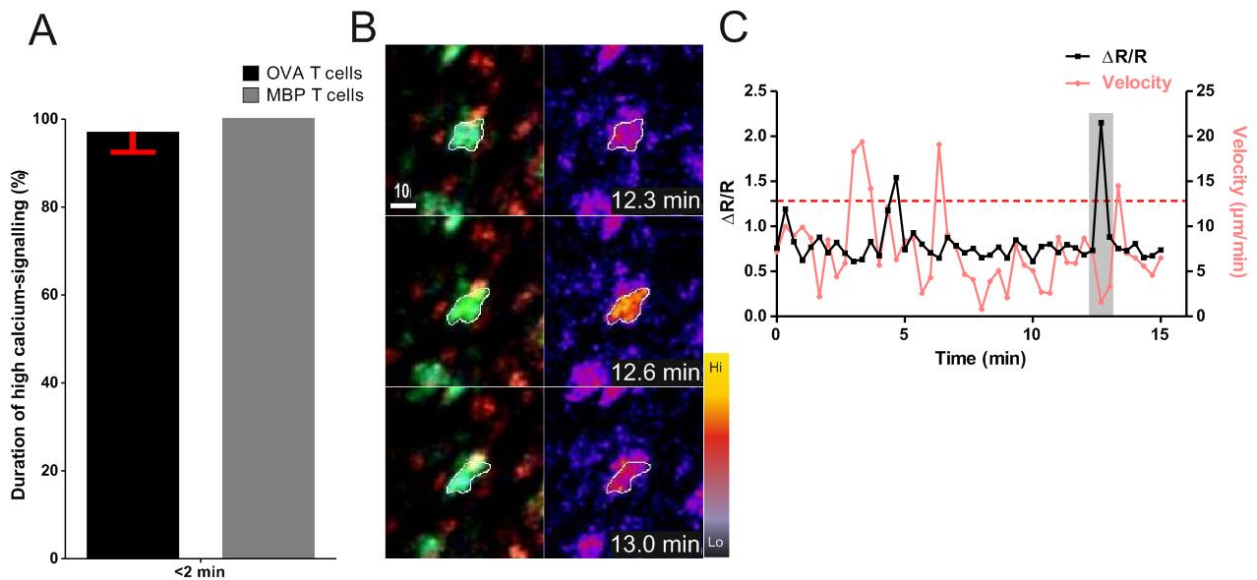
Figure 3.1.5 Short calcium spikes in the spleen. A. Duration of high-calcium signaling in the spleen. Representative data from 2 independent experiments per cell line are shown. B. Series from *in vivo* calcium imaging of the spleen with $T_{OVA-Twitch1}$ cells. A fluorescence overlay of $T_{OVA-Twitch1}$ cells encircled (left) and a pseudocolour ratio image with T cells encircled (right) are depicted. The inserted numbers indicate the relative time after the start of image acquisition. Scale bar: 10 μm. C. Representative track for intracellular calcium levels (black line) and T cell velocities (red line) in the spleen with two short high-calcium spikes. The grey area indicates the three imaging frames from (A).

Antigen application and maximum stimulation in the spleen

In order to provide the maximum intracellular high-calcium stimulation, soluble antigen was injected intravenously during intravital imaging. Splenic APCs were labeled with intravenous injection of fluorescent dextran. In line with a previous study (Odoardi et al., 2007b), within a short time after soluble antigen treatment, T cells decelerated and stopped. In addition, the majority of them showed long-lasting high-calcium signaling (Fig. 3.1.6A). It is important to note that both $T_{MBP-Twitch1}$ cells and $T_{OVA-Twitch1}$ cells responded to their specific antigen with similar time kinetics (Fig. 3.1.6B).

A

B
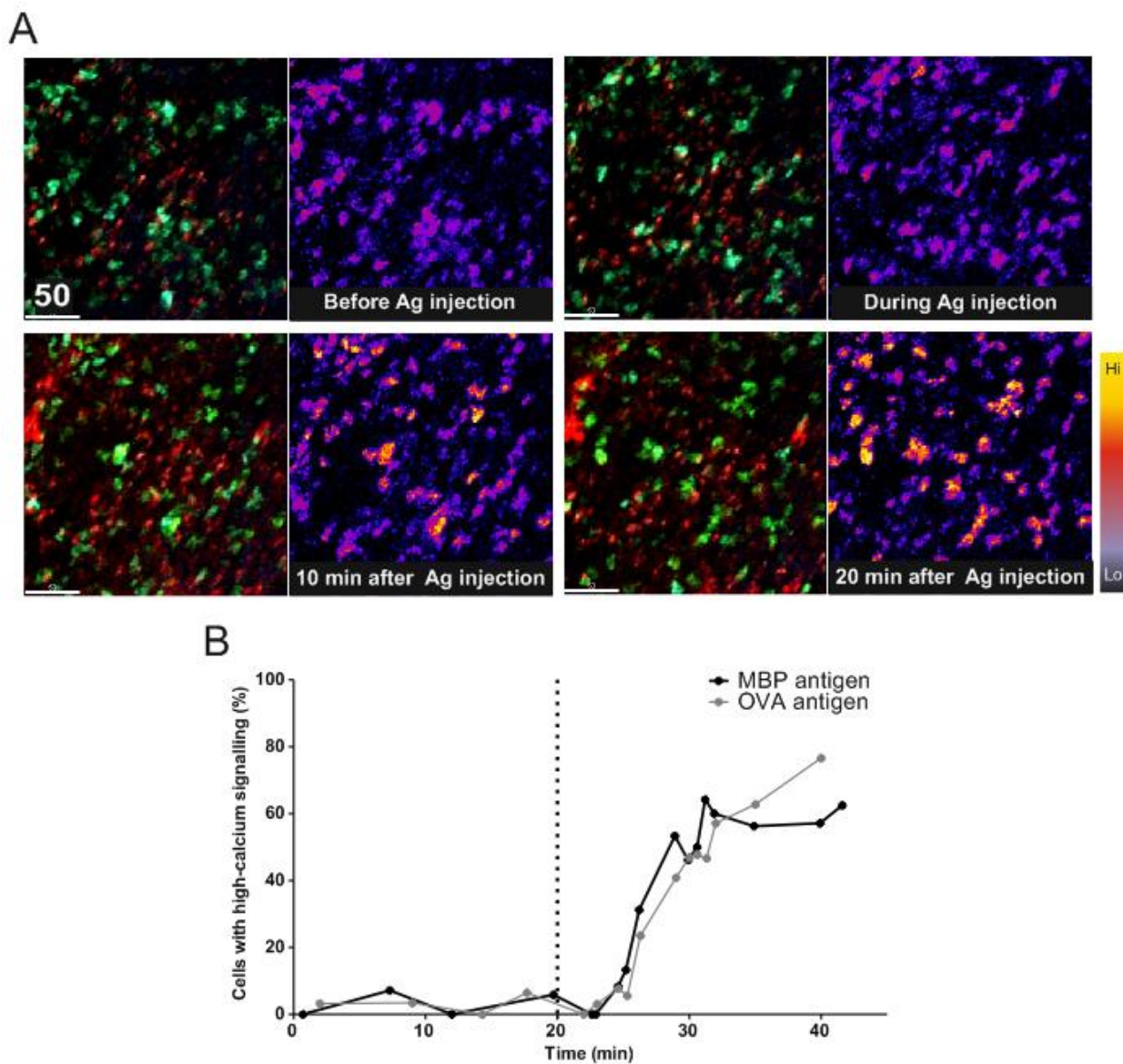
Figure 3.1.6 Soluble antigen treatment. A. Series from *in vivo* calcium imaging of the spleen with T_OVA-Twitch1 cells before and after soluble antigen treatment are shown. A fluorescence overlay of T_OVA-Twitch1 cells (left) and a pseudocolour ratio image with T cells (right) are depicted. Scale bar: 50 μm. T cells (blue/yellow) and phagocytes (red) are shown in fluorescent overlay. B. Time kinetics for the proportion of T_MBP-Twitch1 (black line) and T_OVA-Twitch1 (grey line) cells with high-calcium levels. The vertical line indicates the time point of soluble antigen treatment. The results are representative of at least three independent experiments.

3.1.3 Mechanisms of antigen-independent calcium spikes

MHC class II blocking in the spleen

The calcium spikes of T cells in low antigen milieus could be triggered either through T cell receptors receiving tonic signals from unspecified self-antigens (Hochweller et al., 2010) or through antigen-independent mechanisms (Revy et al., 2001). The administration of anti-MHC class II-blocking antibody slightly reduced the frequency of calcium signaling (Fig. 3.1.7).
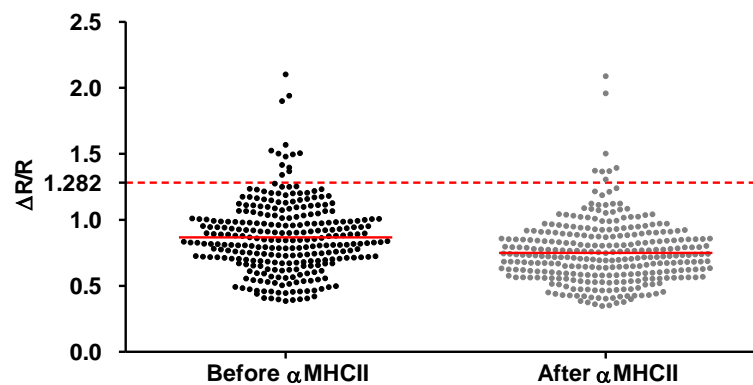
Figure 3.1.7 T$_{OVA-Twitch1}$ cells were imaged in the spleen on day 3 p.t. before and after injection of anti-MHC class II (αMHCII) antibody. Cumulative plots of the calcium level (ΔR/R) are shown. Each dot represents a single time point in a particular cell. The results are the sum of at least three independent experiments per treatment.

Chemokine signal induces short-lasting calcium spikes

As it was described previously, short-lasting calcium spikes in the spleen may derive from antigen-independent mechanisms. Thus, it was important to explore whether this calcium flux was induced through the chemokines receptors. In general, GPCRs trigger leukocyte locomotion and they are involved in chemokine activation. In contrast to *in vitro* activated T cells, which do not rearrange their gene expression profile, both T$_{MBP-Twitch1}$ and T$_{OVA-Twitch1}$ cells acquire a migratory phenotype in the spleen and express chemokine receptors. Consequently, in order to examine the GPCR effects in intrasplenic T cell behavior, T$_{OVA-Twitch1}$ cells were purified from the spleen on day 3 after adoptive transfer. Then, the T$_{OVA-Twitch1}$ cells were treated *in vitro* with inhibitors for chemokine receptors and re-transferred into the naïve recipients. On the day following the re-transfer, many autoreactive T cells were found in the spleen.

Initially, a general inhibitor of GPCRs was applied. PTX blocks a broad spectrum of chemokine receptors as it prevents the G proteins from interacting with their cognate GPCRs (Mangmool and Kurose,

2011). When $T_{OVA-Twitch1}$ cells were treated with this bacterial exotoxin, the proportion of cells which showed calcium spikes was significantly reduced (Fig. 3.1.8).
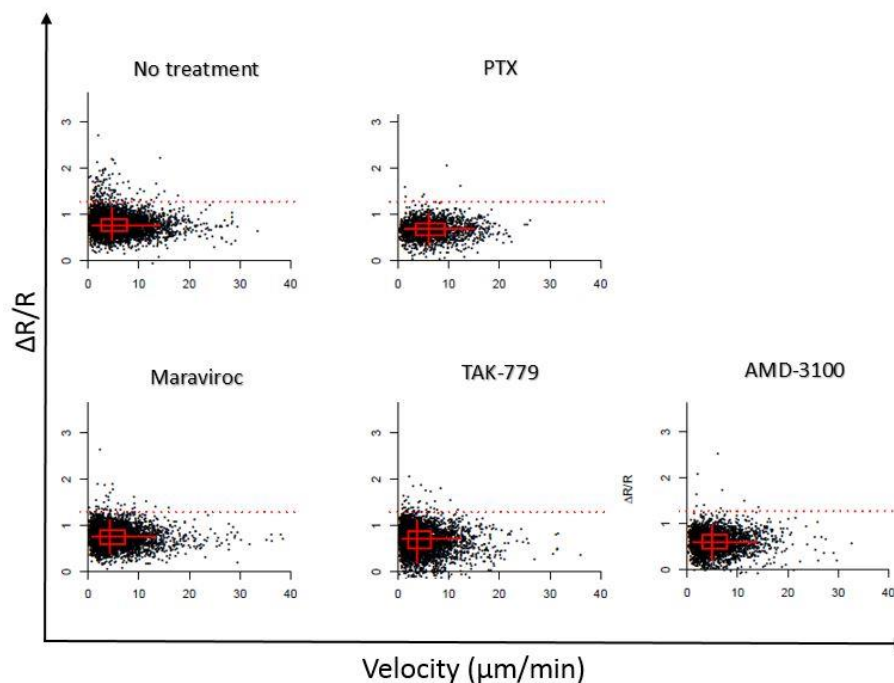
Figure 3.1.8 Scatter plots showing the $T_{OVA-Twitch1}$ velocity versus the calcium-indicator ratio change for each individual time point with or without inhibitor treatment. Mean values for ΔR/R and velocity are indicated along with a two-dimensional box plot. The results are the sum of at least three independent experiments per treatment.

In addition, according to a previous study, T cells express CCR1, -2b, -3, -5, -7 and CXCR4 in the spleen after adoptive transfer (Flügel et al., 2001). In order to clarify whether these chemokine receptors induce high-calcium signaling, three potential inhibitors were used. AMD-3100, a CXCR4 inhibitor, almost diminished the short-lasting calcium spikes (Fig. 3.1.9A and 3.1.9C). In addition, Maraviroc, a CCR5 inhibitor, and TAK-779, a CCR2-CCR5 inhibitor, reduced the frequency of short-lasting calcium spikes as effectively as PTX (Fig. 3.1.9A). However, none of these treatments influences T cell motility drastically (Fig. 3.1.9B) indicating that T cell migration is not depending on CCR2, CCR5 or CXCR4.
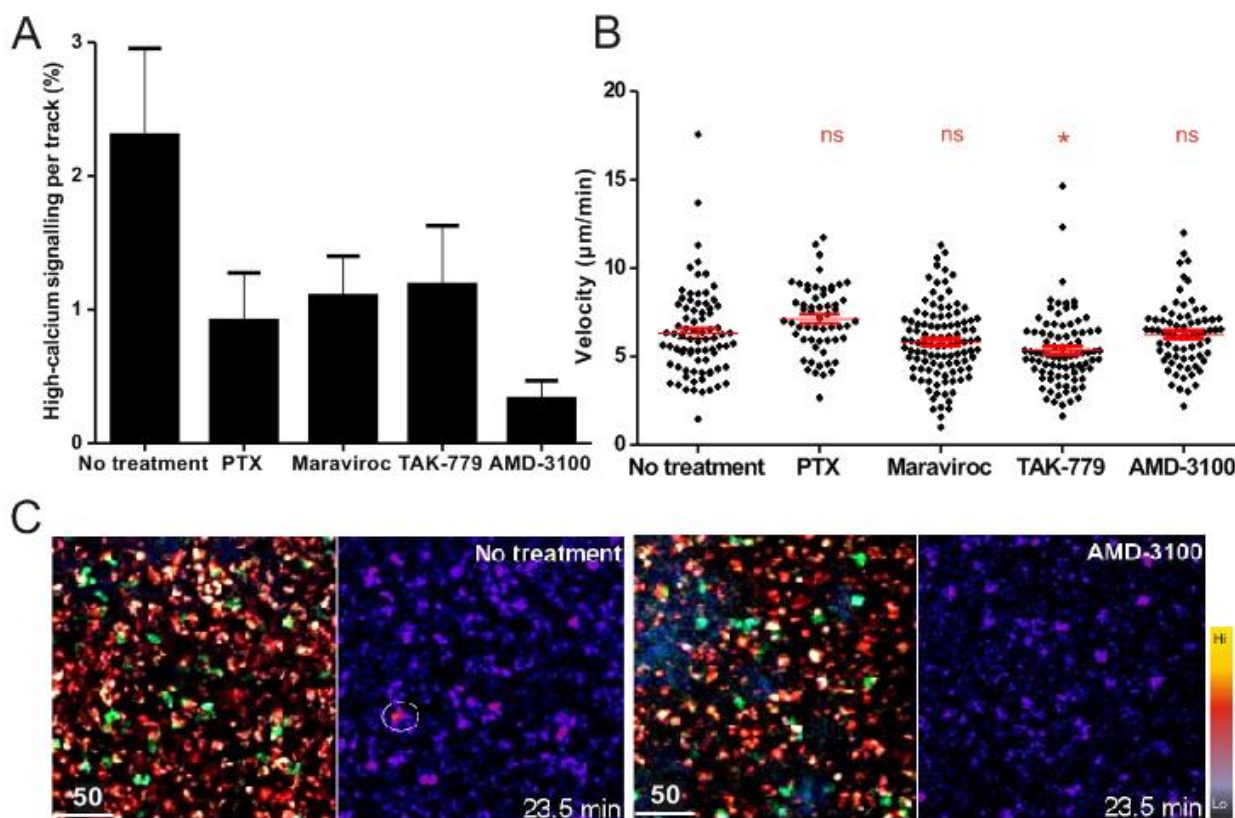
Figure 3.1.9 A. Percentage of high-calcium signaling per track in the spleen with or without inhibitor treatment. **B.** Quantification of the average T cell velocity in the spleen with or without inhibitor treatment. **C.** Representative images from *in vivo* calcium imaging of the spleen with T$_{OVA-Twitch1}$ cells. A fluorescence overlay of T$_{OVA-Twitch1}$ cells (left) and a pseudocolour ratio image with T cells (right) are depicted. A cell with elevated calcium is encircled in the pseudocolour ratio image. The inserted numbers indicate the relative time after the start of image acquisition. Scale bar: 50 μm. T cells (blue/yellow) and phagocytes (red) are shown in fluorescent overlay. **(A-B)** The data are presented as the mean ± s.e.m. The results are the sum of at least three independent experiments per treatment.

3.1.4 Intravital imaging of Twitch1-labeled T cells within leptomeningeal vessels

Bartholomäus et al. described the process of MBP specific encephalitogenic T cell infiltration into the CNS (Bartholomäus et al., 2009). After acquiring a migratory phenotype in the spleen and before the onset of EAE, T$_{MBP-GFP}$ cells appear in the blood vessels at the spinal cord leptomeninges. Within the leptomeningeal vessels, T cells roll, adhere, and crawl on the intraluminal surface. It is noteworthy to mention here, that both the crawling and the rolling T cells restrict ΔNFAT-GFP to their cytosol (Pesic et al., 2013). However, it has remained unclear whether T cells display different calcium levels during these interactions.

Activation status of rolling T cells

Intravital imaging using $T_{MBP-Twitch1}$ and $T_{OVA-Twitch1}$ cells was performed on day 2 p.t. in order to analyze the calcium dynamics of rolling T cells. Although two-photon microscopy is not an ideal method for detecting rolling cells, due to its relatively slow scanning rate, some rolling cells can be occasionally detected. Indeed, in this study, two-photon microscopy detected individual rolling T cells as a series of round cells within one single time frame (Fig. 3.1.10A-C).
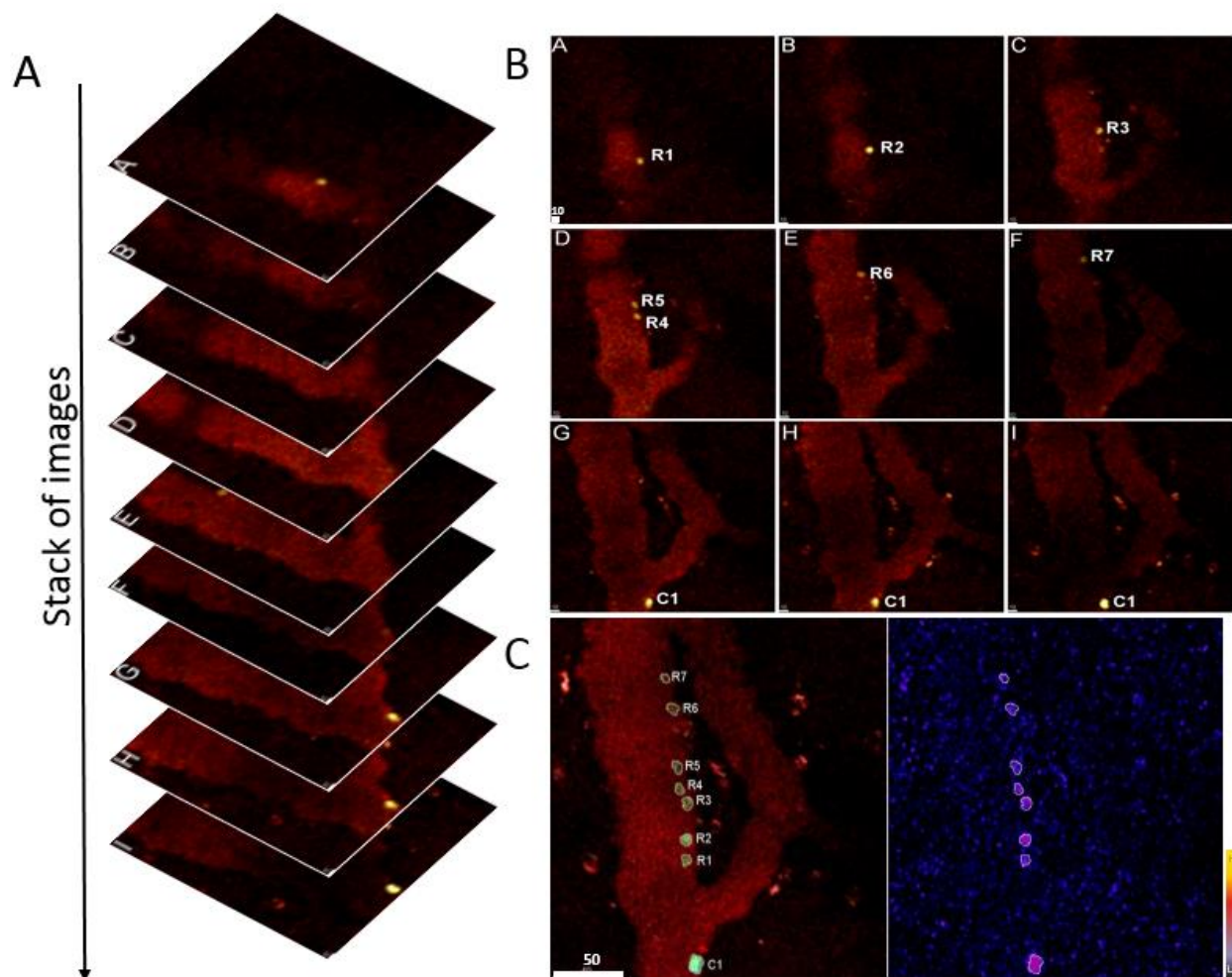
Figure 3.1.10 Detection of rolling and crawling cells by two-photon microscopy. Scheme to detect rolling and crawling cells. A. Scanning of z-dimension acquires a series of images. B. Typical cellular size is 10µm. Since z-interval is around 3-4 µm, one cell can be detected multiple times. The motility of rolling T cells is very high, therefore, a rolling cell locates at different x,y position in subsequent frames. For example, a rolling cell appears in images A-F in seven different positions (R1-R7). In images G-I, a crawling cell appears (C1). Scale bar: 10 µm.) C. Z-projection of images (A) reveals a trace of a rolling cell (R1-R7) and a crawling cell (C1). Scale bar: 50 µm. A fluorescence overlay of $T_{MBP-Twitch1}$ cells (left) and a pseudocolour ratio image with T cells (right) are depicted. T cells (blue/yellow) and blood vessel (red) are shown in fluorescent overlay.

Instantaneous velocity and intracellular calcium were analyzed at each event precisely. While rolling along the luminal surface, the T cells displayed no detectable calcium activity (Fig. 3.1.11A). Few events that correspond to the transition from rolling to crawling and from crawling to rolling were detected (Fig. 3.1.11B-C). Intriguingly, during this transition, cells often showed higher calcium spikes when they started to crawl without, however, following a constant and repetitive pattern (Fig. 3.1.11B).
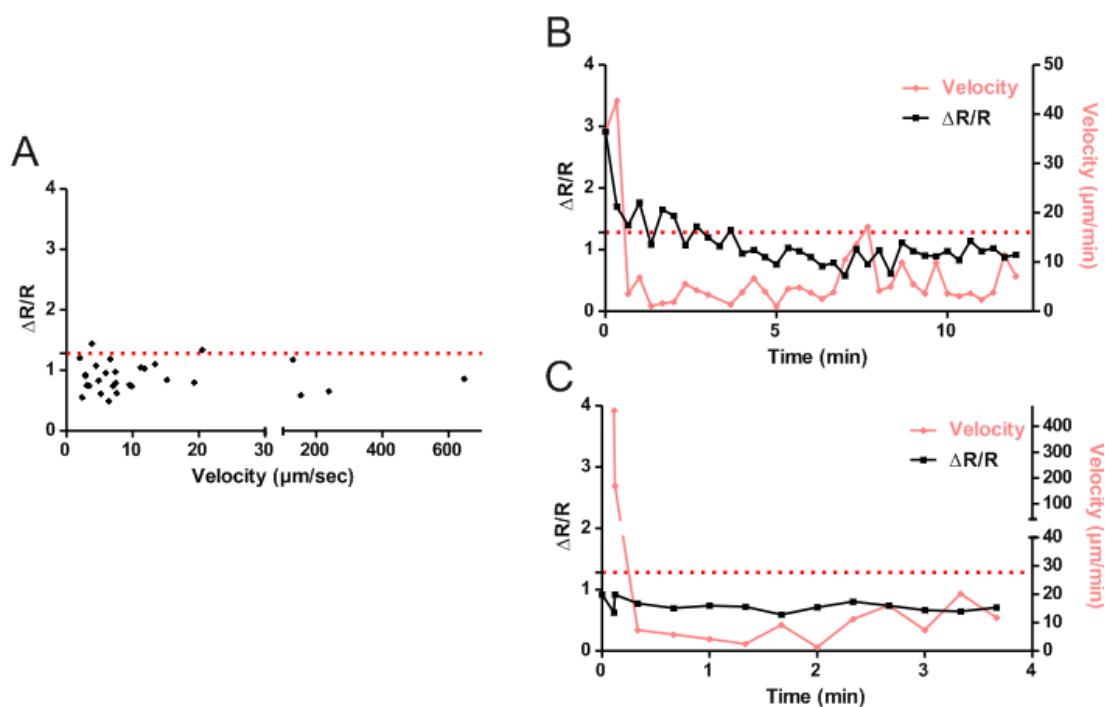
Figure 3.1.11 A. Scatter plot showing T$_{MBP\text{-}Twitch1}$ velocity versus calcium-indicator ratio change for each individual time point during rolling. The results are sum of three independent experiments. B-C Representative results of two T$_{MBP\text{-}Twitch1}$ cells and their calcium levels during transition from rolling to crawling. Velocity (red line) and calcium level (black line) are plotted. B. The rolling cell showed high-calcium spikes during transition. C. The rolling cell showed constant low-calcium levels during transition.

Activation status of crawling T cells

Opposed to intraluminal rolling, intraluminal crawling can be reliably detected by two-photon microscopy. The analysis showed that T cells rarely presented calcium spikes, regardless of their antigen specificity and instantaneous velocity (Fig. 3.1.12A-B). Therefore, the intraluminal crawling of T cells proceeded without elevated calcium signaling. Overall, the intraluminal locomotions of T$_{MBP\text{-}Twitch1}$ and T$_{OVA\text{-}Twitch1}$ cells were indistinguishable.
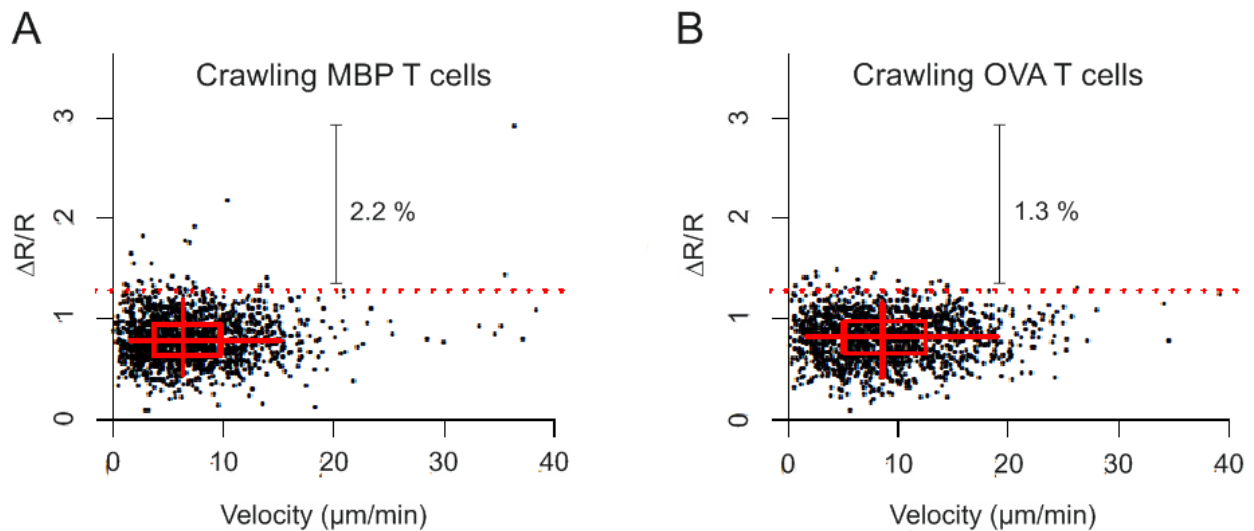
Figure 3.1.12 Scatter plots showing (A) T_{MBP-Twitch1} and (B) T_{OVA-Twitch1} velocity versus calcium-indicator ratio change for each individual time point during crawling. T_{MBP-Twitch1} (2.2%) and T_{OVA-Twitch1} (1.3%) showed rarely calcium spikes. The results are the sum of at least three independent experiments.

3.1.5 Intravital imaging of Twitch1-labeled T cells within leptomeninges

T cell activation during the prodromal phase of infiltration

After diapedesis and during the early prodromal phase of infiltration on day 2 p.t., T_{MBP-Twitch1} cells remained in close proximity with the abluminal vascular surface of pial blood vessels. At this point, right before the onset of clinical EAE, the number of cells in the spinal cord was low. They started scanning the CNS vessel-associated milieu seeking for APCs and forming short or long-lasting contacts with them (Fig. 3.1.13A). Upon antigen recognition, T cells decelerated and kept either a slow motility or they completely arrested around the APCs. In parallel, TCR stimulation led to high intracellular calcium signals that varied from infrequent short-lasting peaks to sustained plateaus (Fig. 3.1.13B). Confirming previous studies (Mues et al., 2013), it was observed that the velocity of T cells was inversely correlated to high-calcium signaling (Fig. 3.1.13B). In contrast to a previous study in which excessive amount of endogenous antigen was applied (Wei et al., 2007), here, it was showed that low levels of endogenous antigen were sufficient to induce long-lasting calcium spikes.
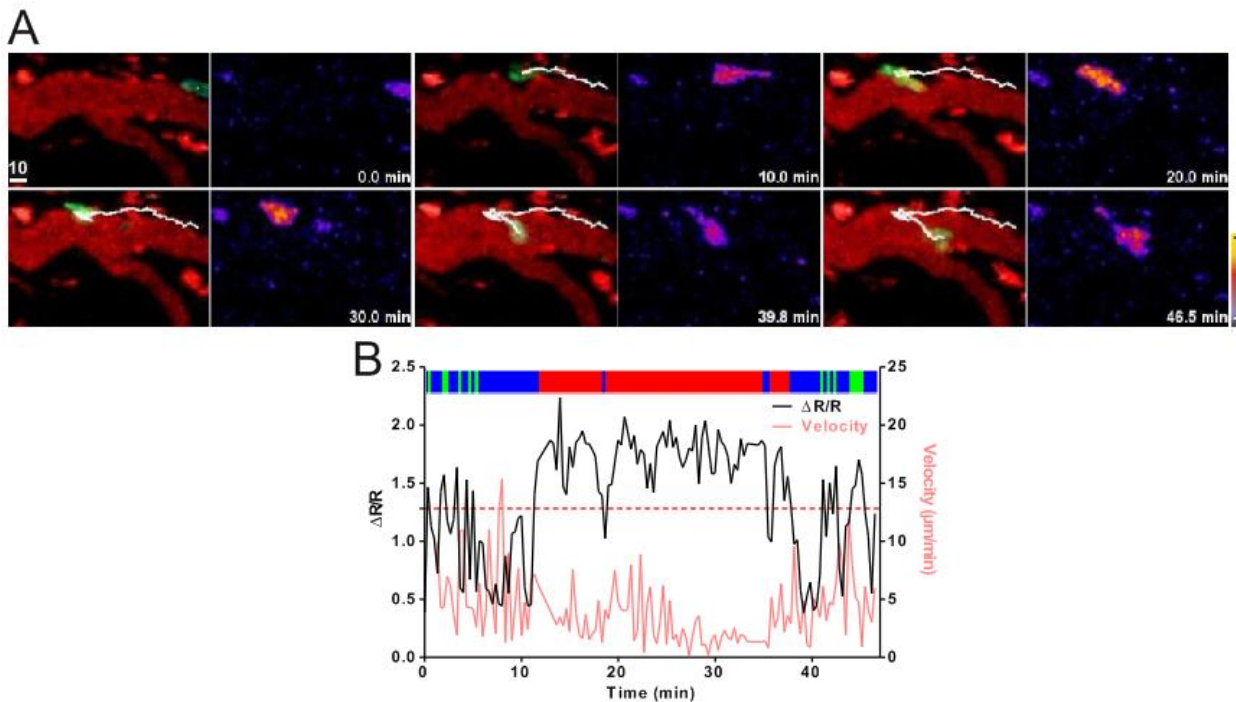
Figure 3.1.13 A. A series from *in vivo* calcium imaging of the meninges on day 2 p.t. is depicted. A fluorescence overlay of T$_{MBP-Twitch1}$ cells (left) and a pseudocolour ratio image (right) are shown. A trajectory line (white) is overlaid and represents a single T$_{MBP-Twitch1}$ cell track. The inserted numbers indicate the relative time after the start of image acquisition. Scale bar: 10 µm. T cells (blue/yellow) and phagocytes (red) are shown in fluorescent overlay. B. Representative track of a T$_{MBP-Twitch1}$ cell (depicted in A) showing the intracellular calcium levels (black line) and T cell velocities (red line) in the meninges on day 2 p.t. The dotted line depicts the ΔR/R threshold. A calcium history plot is overlaid. In the calcium history plots, a blue colour indicates low-calcium levels, a green colour indicates high-calcium levels shorter than 2 min and a red colour indicated high-calcium levels longer than 2 min.

T cell activation during the EAE onset

The behaviour of T$_{MBP-Twitch1}$ cells altered on day 3 p.t., at the onset of clinical EAE. T cells crossed the BBB at a higher rate and migrated randomly in all directions. T cell-APC contacts were followed by intensive intracellular high-calcium signals that varied from scattered, short-lived peaks to sustained plateaus (Fig. 3.1.14D). Although they presented similar calcium signatures as the ones from day 2 p.t. (Fig. 3.1.14B-C), they also started scanning the entire leptomeningeal space (Fig. 3.1.14E). Surprisingly, despite the similar percentage of long high-calcium signaling between day 2 and day 3 p.t. (Fig. 3.1.14C), the duration of high-calcium signaling was different (Fig. 3.1.14A). In general, T cells on day 2 and day 3 p.t. presented sustained high-calcium signals that lasted less than 20 min. However, it was only the T cells that initially breached the BBB which maintained increased intracellular calcium concentrations for over 20 min. On day 2 p.t., the longest high-calcium signal lasted for almost 2 hours.
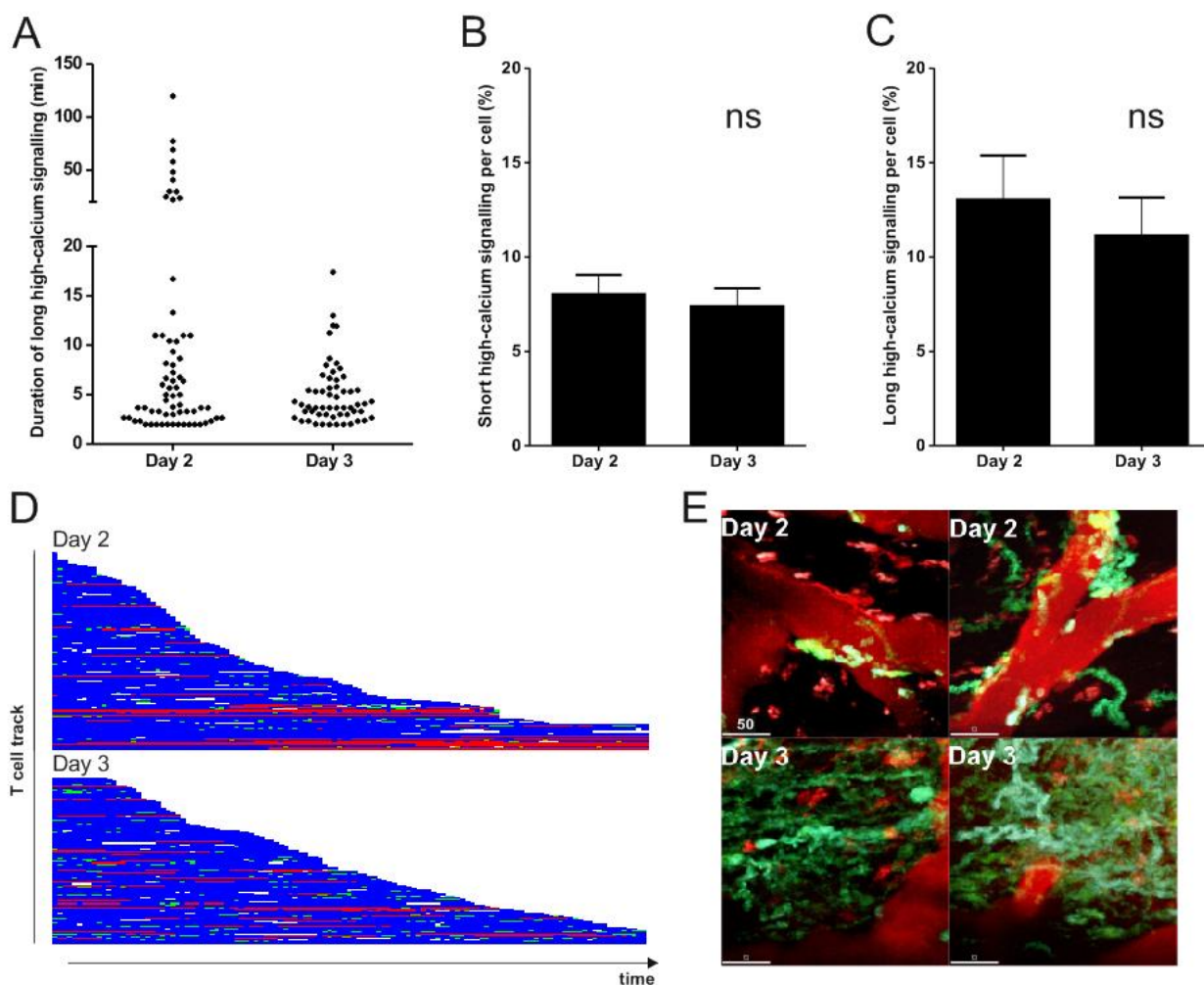
Figure 3.1.14 A. Cumulative plots of long high-calcium signaling (over 2 min) on days 2 and 3. B-C. The percentage of short (B) or long (C) high-calcium signaling per track on days 2 and 3. D. Calcium history plots of T$_{MBP-Twitch1}$ cells on days 2 and 3. Each line represents single T cell track. In the calcium history plots, a blue colour indicates low-calcium levels, a green colour indicates high-calcium levels shorter than 2 min and a red colour indicated high-calcium levels longer than 2 min. E. Time projections from four representative movies are shown for T$_{MBP-Twitch1}$ cells (green) on day 2 (upper pictures) and day 3 (lower pictures) p.t.. Scale bar: 50 μm. A-D The results are the sum of at least three independent experiments.

3.1.6 Intravital imaging of Twitch1-labeled T cells within parenchyma

During the acute phase of the EAE on day 4 p.t., T$_{MBP-Twitch1}$ cells massively invade the CNS and infiltrate deep into the parenchyma (Kawakami et al., 2005). Although the two-photon microscopy has a superior penetration depth, it is still impossible to perform imaging deep inside the spinal cord parenchyma. Therefore, imaging in the acute explant was performed as previously described (Kawakami et al., 2005) and dead cells were eliminated from the analysis after DAPI staining with low dose. Also, in order to identify the interaction partners of T$_{MBP-Twitch1}$ cells in the CNS parenchyma, the spinal cord explants were stained with fluorescent conjugated isolectin B4. The latter stained the microglia as well as the

infiltrated monocytes/macrophages. Two-photon imaging in the stained explant revealed an interaction between T_{MBP-Twitch1} cells and microphage-like cells (Fig. 3.1.15). In addition, during this interaction T_{MBP-Twitch1} cells showed both short- and long-lasting high-calcium spikes.
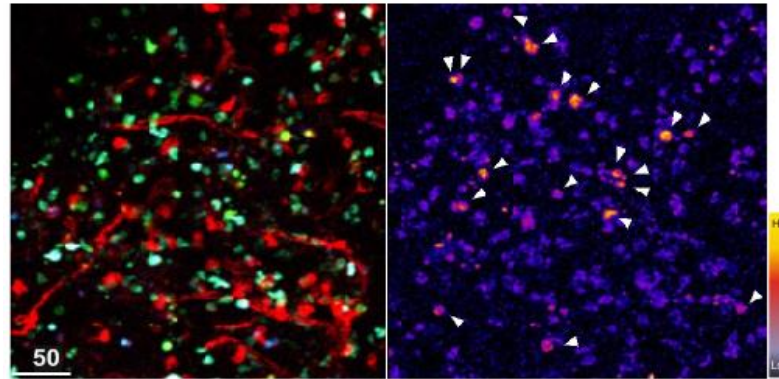
Figure 3.1.15 Sample image from an acute explant in the parenchyma with T_{MBP-Twitch1} cells. A fluorescence overlay of T_{MBP-Twitch1} cells (left) and a pseudocolour ratio image with T cells (right) are depicted. The acute explant was stained with isolectin B4 (red) and DAPI (blue) in left panel. Cells with elevated calcium are indicated with white arrowheads. Scale bar: 50 µm.

3.1.7 Deciphering the relation between antigen stimulation and intracellular calcium signaling

In contrast to encephalitogenic MBP specific T cells, OVA specific T cells do not infiltrate into the CNS. Therefore, T_{OVA-Twitch1} cells can be piloted there when they are co-transferred with non-labeled MBP specific T cells. The latter cells open the BBB and create an inflammatory microenvironment (Flügel et al., 2001). Two-photon imaging of T_{OVA-Twitch1} cells was performed in the spinal cord leptomeninges together with labeled APCs. The results indicated that T_{OVA-Twitch1} cells displayed significantly higher motility than T_{MBP-Twitch1} cells (Fig. 3.1.16A-B), which is in line with previous reports (Bartholomäus et al., 2009, Kawakami et al., 2005). As expected by their antigen specificity, the infiltrated T_{OVA-Twitch1} cells rarely emitted calcium spikes (Fig. 3.1.16A, Fig. 3.1.17A-B and Fig. 3.1.18). T_{OVA-Twitch1} cells spiked less than once per hour (Fig. 3.1.17A), while less than 1% of each analyzed T_{OVA-Twitch1} cell track showed high-calcium intracellular signaling during intravital imaging (Fig. 3.1.17B). However, those calcium spikes are always short-lasting, comparing to those of T_{MBP-Twitch1} cells. The T_{MBP-Twitch1} cells spiked 8.6 times per hour in average (Fig. 3.1.17A) and presented both long and short elevated calcium signaling (Fig. 3.1.17B).
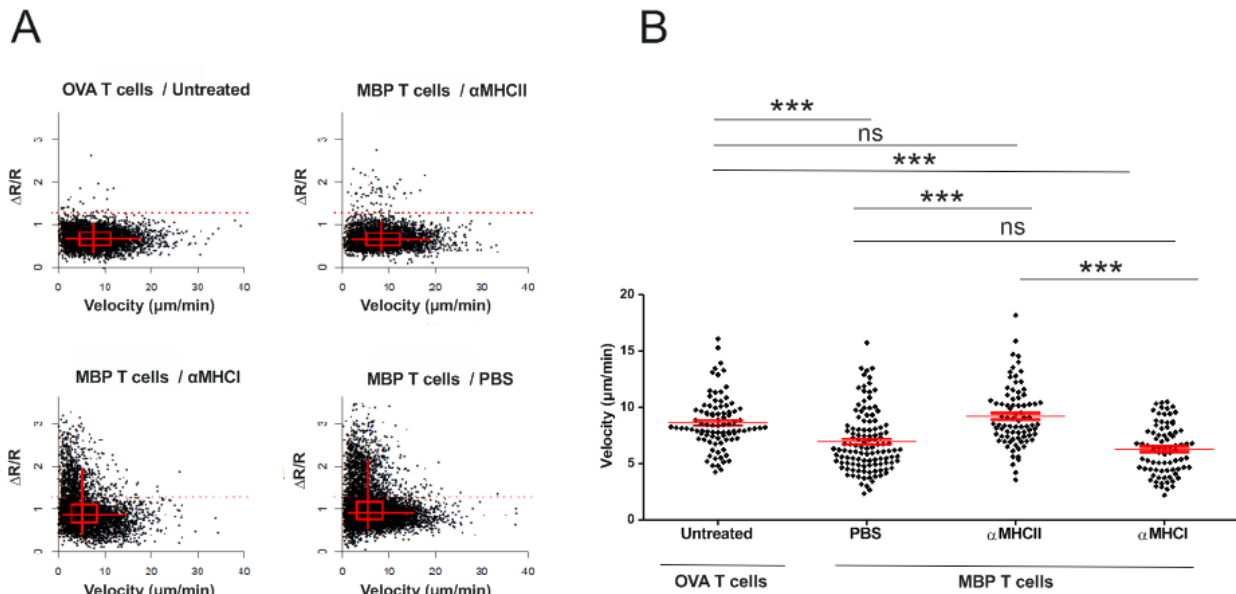
Figure 3.1.16 A. Scatter plots showing $T_{OVA-Twitch1}$ or $T_{MBP-Twitch1}$ velocity versus calcium-indicator ratio change for each individual time point with or without antibody treatment. Mean values for ΔR/R and velocity are indicated along with a two-dimensional box plot. (B) Quantification of the average T cell velocity in the spinal cord leptomeninges with or without antibody treatment. A-B. The results are the sum of at least three independent experiments per treatment.

Further evidence for antigen-dependent activation of encephalitogenic T cells emerged from intrathecal application of anti-MHC class II blocking antibody. As shown in Fig. 3.1.16B, the infusion of anti MHC class II restored the motility of $T_{MBP-Twitch1}$ cells to the level of $T_{OVA-Twitch1}$ cells. In addition, anti-MHC class II treatment reduced the number of spikes in $T_{MBP-Twitch1}$ cells to less than one per hour, again similar to $T_{OVA-Twitch1}$ cells. In contrast, anti-MHC class I antibody did not show any effect neither in locomotion nor in calcium responses. In fact, after MHCI treatment, the $T_{MBP-Twitch1}$ cells displayed similar calcium signatures with the non-treated ones whereas the anti-MHC class II treatment calcium signatures were similar to $T_{OVA-Twitch1}$ cell tracks (Fig. 3.1.18). As shown by panoramic pictures, this blocking effect was demonstrable in a larger area of spinal cord (Fig. 3.1.17C).

It is important to note that in contrast to peripheral treatment, only the anti-MHC class II treatment in the CNS blocked the development of clinical EAE dramatically (Fig. 3.1.17D). These results indicated that antigen-dependent stimulation induced long-lasting high-calcium signaling, which was definitely a crucial step to initiate CNS inflammation.
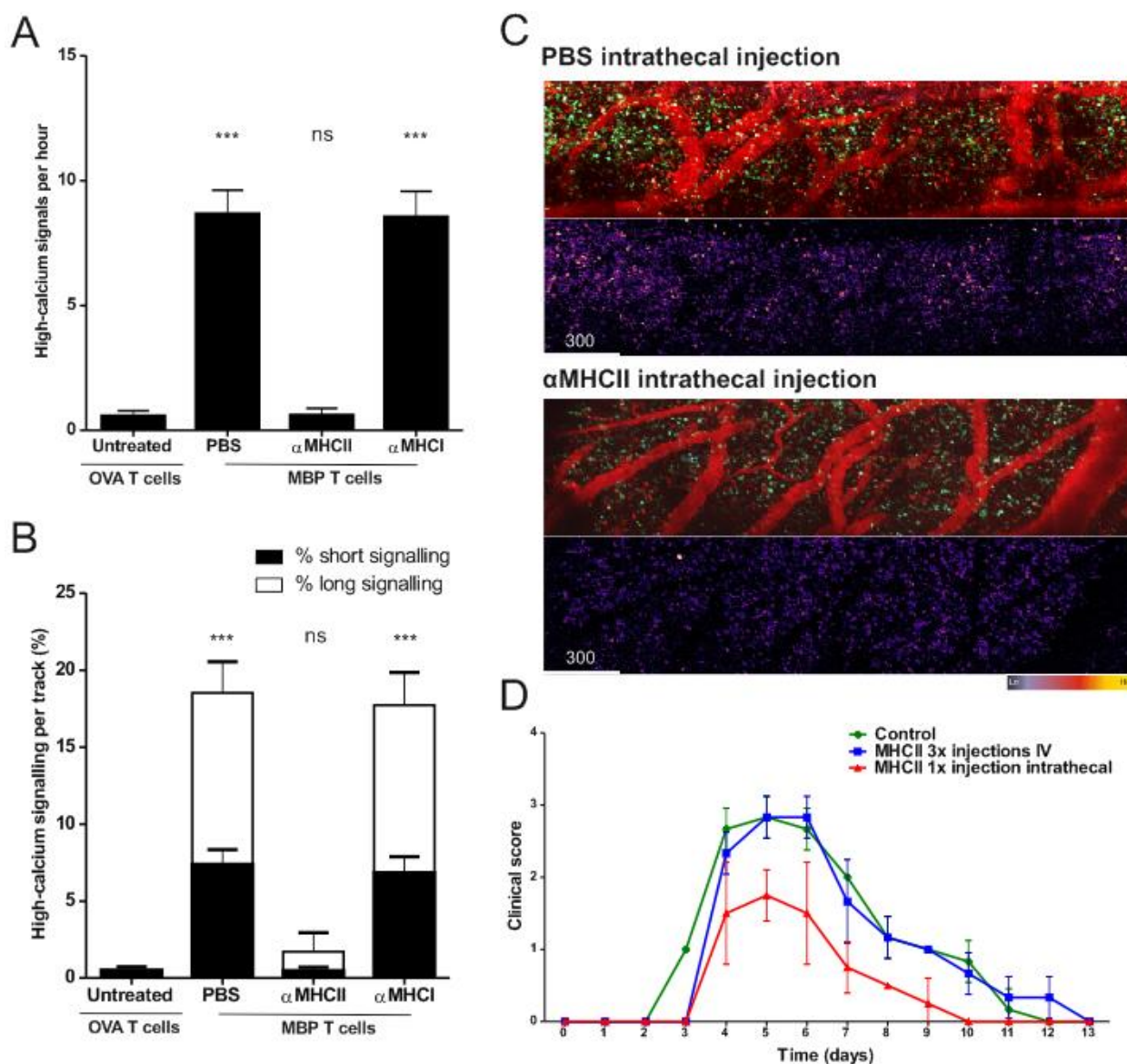
Figure 3.1.17 A-B. Frequency of high-calcium signals over the threshold normalized per hour (A) and the proportion of short or long high-calcium signaling during imaging (B) are shown. The results are the sum of at least three independent experiments per treatment. C. Representative panoramic pictures of T$_{MBP-Twitch1}$ cells in the spinal cord leptomeninges after PBS or anti MHC class II intrathecal injection are shown. Fluorescence overlay (upper) and a pseudocolour ratio image (lower) were obtained from intravital imaging on day 3 p.t.. Scale bar: 300 μm D. EAE clinical score induced by transfer of T$_{MBP-Twitch1}$ cells with or without anti MHC class II intrathecal (1x) or intravenous (3x) injections. Mean ± SD from at least 3 animals per group are shown. αMHCI: anti MHC class I.
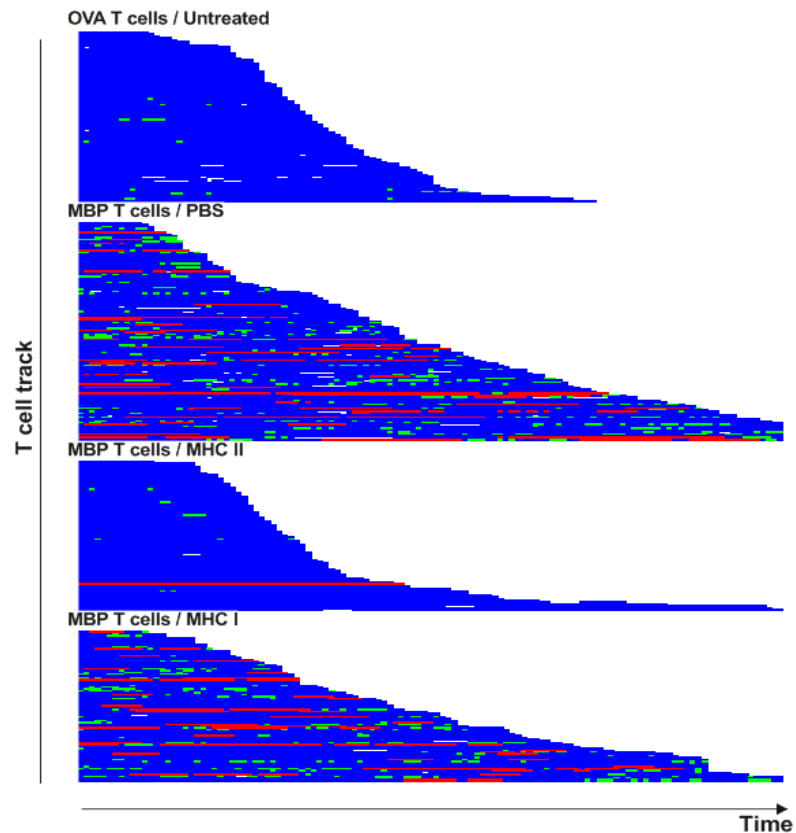
Figure 3.1.18 Calcium history plots of non-treated T$_{OVA-Twitch1}$ cells and T$_{MBP-Twitch1}$ cells on day 3 p.t. with or without antibody treatment. Each line represents one single T cell track. In the calcium history plots, the blue colour indicates low-calcium levels, the green colour indicates high-calcium levels shorter than 2 min, and the red colour indicates high-calcium levels longer than 2 min.

3.1.8 Leptomeningeal APCs have disparate functional potential

From intravital imaging, it was observed that not all APCs have the capacity to stimulate the T cells. CNS infiltrated T cells often passed neighbor APCs without stopping or presenting high-calcium signaling. Besides, the antigen presenting capacity of APCs in the CNS leptomeninges is considered very low (Bartholomäus et al., 2009). Time projection of pseudo-colored images revealed a mosaic of different calcium potentials amongst APCs (Fig. 3.1.19A). Single APCs were identified and the capacity was evaluated by calculating the percentage of activated T cells when T cells contacted them (Fig. 3.1.19B). The results confirmed an unequal distribution of calcium spikes, indicating that some APCs could activate T cells more efficiently than others (Fig. 3.1.19C). For example, APC No. 12 in Fig. 3.1.19B had a strong potential to stimulate T cells, whereas other APCs, such as APC No.3, hardly induced any T cell activation, although several T cells passed by.
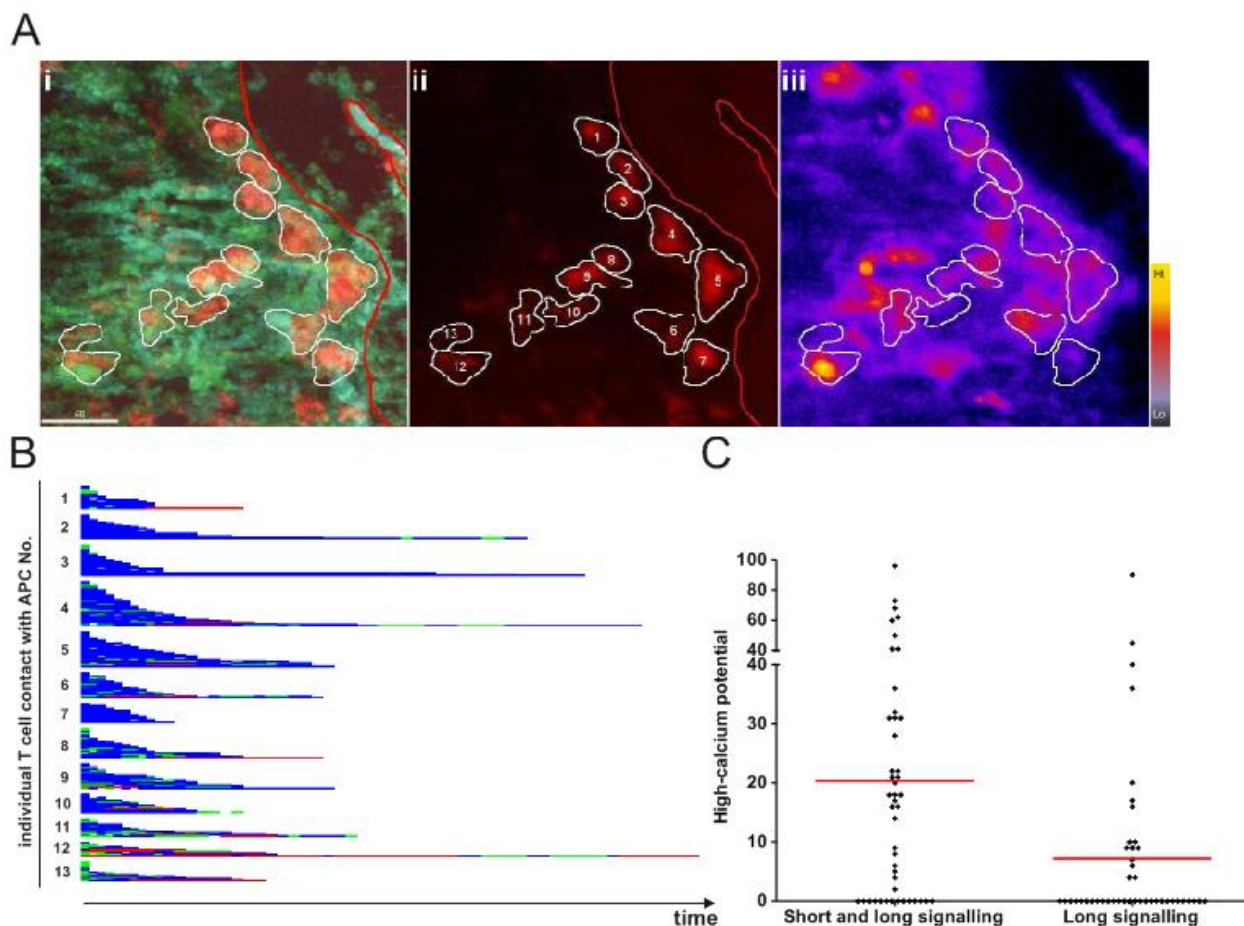
Figure 3.1.19 A. Sample images from *in vivo* calcium imaging of leptomeningeal vessels on day 3 p.t. A fluorescence overlay of T_{MBP-Twitch1} cells and APCs (i), only APCs (ii) and a pseudocolour ratio image with T_{MBP-Twitch1} cells and APCs (iii) are depicted. APCs with high and low potential to stimulate T cells are encircled. B. Calcium history plots of the T_{MBP-Twitch1} cells during contact with APCs. Numbers represent APCs identified in (Aii). Each line represents single continuous contact. Blue colour indicates low-calcium levels, green colour indicates high-calcium levels shorter than 2 min and red colour indicates high-calcium levels longer than 2 min. C. High-calcium potential in T cells during T cell/APC contacts. The calcium potential depicts the time proportion of the total short and/or long high-calcium signaling during T cell/APC contacts. Calcium potential=Duration of high-calcium signaling/duration of contact*100. The results are the sum of three independent experiments per time point.

54

3.2 A dual sensor: Combining NFAT and Twitch sensors

3.2.1 Comparing NFAT and Twitch1 sensors

Previously, MBP-specific T cells and MOG-specific T cells from Lewis rats were chosen as EAE[hi] (high encephalitogenic) and EAE[lo] (low encephalitogenic) respectively for the study of differential T cell activation *in vivo* by using a ΔNFAT-GFP sensor (Pesic et al., 2013). $T_{MBP-NFAT-GFP}$ cells made stable contacts with local APCs in the CNS, became activated and triggered classical acute EAE. On the other hand, MOG-specific T cells displayed no activation, and hardly mediated any clinical defects. Similar to $T_{OVA-Twitch1}$ cells which presented almost exclusively low-calcium levels, $T_{MOG-NFAT-GFP}$ cells restricted ΔNFAT-GFP to the cytoplasm (Fig. 3.2.1C). In contrast, MBP-specific T cells with nuclear ΔNFAT-GFP showed intercalated segments of coiled tracks (Fig. 3.2.1A). $T_{MBP-Twitch1}$ cells showed cramped zig-zag movement and presented sporadic short- and long-lasting high-calcium signaling (Fig. 3.2.1A-B). In addition, the percentage of cells with high-calcium levels was significantly lower compared to cells with nuclear ΔNFAT- GFP (Fig. 3.2.1C).
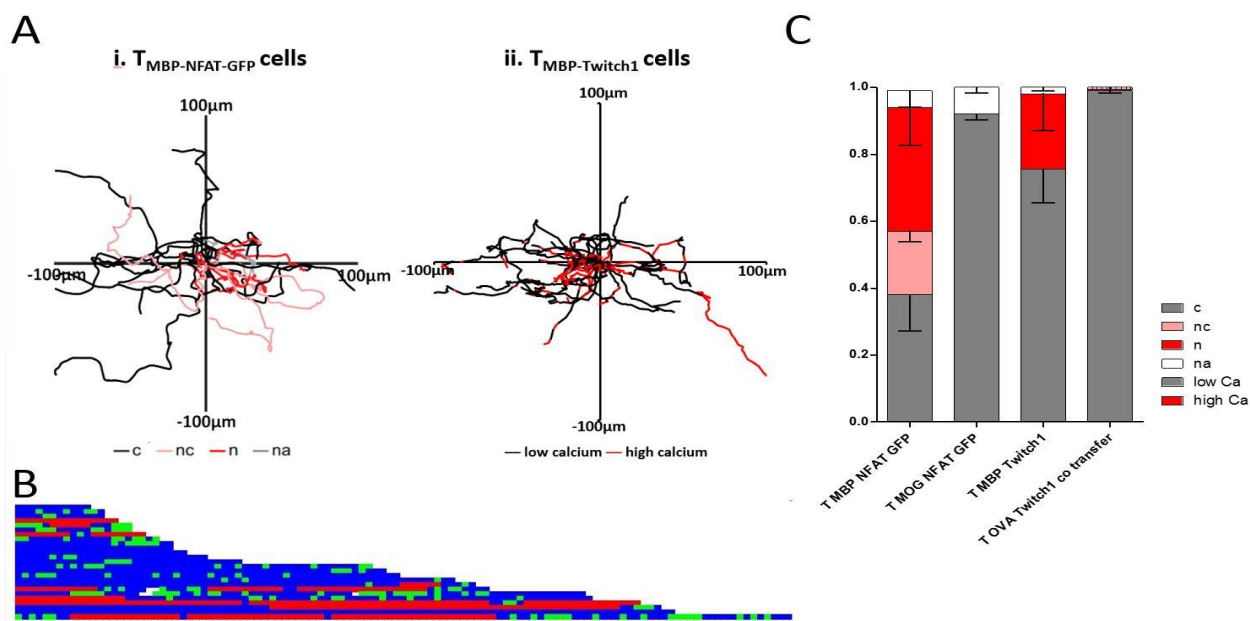
Figure 3.2.1 A. T cell trajectories from representative movies were superimposed; each line starts at the coordinate origin. Lines were colored to indicate the ΔNFAT-GFP location or the calcium levels. B. Calcium history plots of T_{MBP-}
Twitch1 on day 3 from Figure A. Each line represents one single cell track. In the calcium history plots, the blue colour indicates low-calcium levels, the green colour indicates high-calcium levels shorter than 2 min and the red colour indicates high-calcium levels longer than 2 min. C. ΔNFAT-GFP and calcium level patterns in the $T_{MOG/MBP-NFAT-GFP}$ and $T_{OVA/MBP-Twitch1}$ cells were categorized, and their relative occurrence calculated. n.a.: not analyzable. Results for A, B are representative and for C are mean with S.D, from at least three different experiments per cell line. (NFAT results adapted from Pesic et al., 2013).

Pesic et al. addressed the question whether sequential or stable T cell/APC interactions induced the T cell activation. It was indicated that very often "non-activating" contacts with high motility precede

the "activating" ones but mainly the long-lasting contacts are vital for T cell activation (Fig. 3.2.2B). During this study, it was found that a single T cell may interact with different APCs and receive diverse tonic or sustained high-calcium signals from them (Fig. 3.2.2A).

Nevertheless, the calcium signaling pattern that leads to NFAT translocation remains obscure. It is still not clear whether the accumulation of tonic signals is sufficient for T cell activation or a single long high-calcium spike implies NFAT mobilization. A combination of NFAT and Twitch1 would reveal the single-cell dynamics and interpret the various signaling sequences which lead to activation.
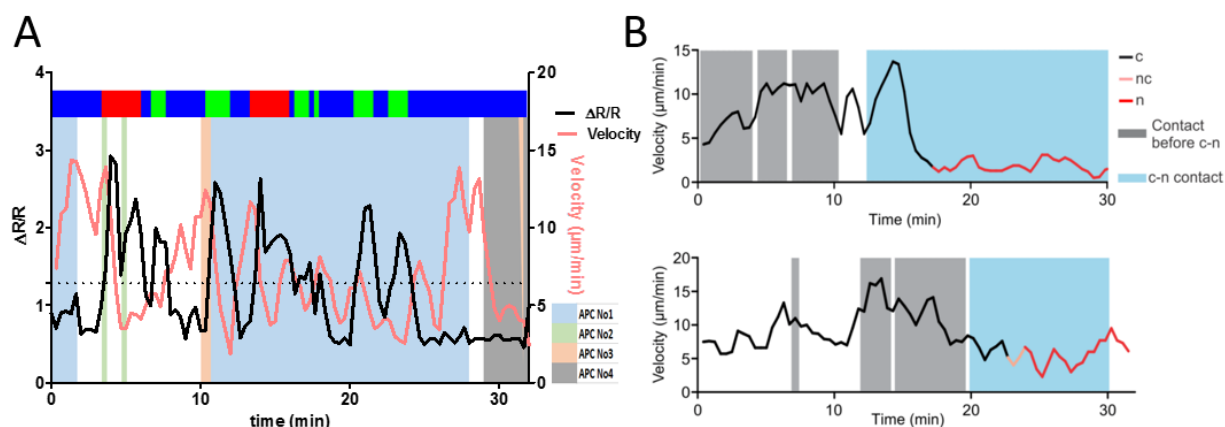
Figure 3.2.2 A. Representative track of a T_MBP-Twitch1 cell depicting the intracellular calcium levels (black line) and T cell velocities (red line - averaged over three time points) in the meninges on day 3 p.t.. The dotted line depicts the ΔR/R threshold. A calcium history plot is overlaid. In the calcium history plots, a blue colour indicates low-calcium levels, a green colour indicates high-calcium levels shorter than 2 min and a red colour indicated high-calcium levels longer than 2 min. Background colours represent contacts with four APCs. B. Instantaneous velocity (averaged over three time points) for two representative T_MBP- NFAT-GFP cells, making various "non-activating" (before c-n) contacts with APCs and finally making the "activating" one (c-n). Line color indicates ΔNFAT-GFP subcellular localization, and background color indicates T cell/APC interaction. (adapted from Pesic et al., 2013).

3.2.2 Evaluation of red fluorescent proteins for NFAT sensor

Pesic et al. introduced a GFP-conjugated, truncated variant of NFAT1 as a "functional" tag to visualize the real-time activation events (Pesic et al., 2013). This construct enclosed the regulatory domain of NFAT1 that is essential for phosphorylation, cytoplasmic sequestration, and calcium-induced and calcineurin-mediated dephosphorylation. Part of the DNA-binding domain of native NFAT was deleted (ΔNFAT-GFP) (Aramburu et al., 1998) so that it does not interfere with gene regulation by endogenous NFAT (Fig. 1.5.2A).

Depending on calcium levels, Twitch1 emits cyan fluorescence and/or yellow fluorescence upon CFP excitation. On the other hand, GFP possesses an emission spectra which is fairly close with YFP (Fig. 3.2.3A). Consequently, in two-photon microscopy it is almost impossible to discriminate between and

separate Twitch1 from ΔNFAT-GFP. For this reason, it was important to choose a set of FPs that would have minimal crosstalk in their emission channels. During this study, five candidates with different properties (regarding their emission spectra and their physiological quaternary structure) were tested for ΔNFAT fusion (Table 3.2.1).

	λ_{ex}	λ_{em}	Oligomerization status
eGFP	488	507	monomer
DsRed2	558	583	tetramer
mKate2	588	633	dimer
mRuby2	559	600	monomer
Fusion Red	580	608	monomer
LSSmOrange	437	572	monomer

Table 3.2.1 Properties of selected FPs. The peak excitation (Ex) and emission (Em) wavelengths and physiological quaternary structure are listed.

ΔNFAT DsRed2 fusion

During co-transferred experiments, DsRed2-labeled MBP specific T cells were injected together with $T_{OVA-Twitch1}$ cells in order to navigate the latter to meninges (see 3.1.7) (Fig. 3.2.3B). However, the transfection efficiency was not similar for NFAT-DsRed2 retroviral construct. The pMSCV-puro-ΔNFAT-DsRed2 retroviral vector (see 2.2.2) was transfected into packaging cells, GP+E86 cells, using the calcium phosphate method. While PuroR was expressed in retrovirus producing packaging cells, all attempts to express DsRed2 were unsuccessful. HEK 293 cells were transfected with the F2U-Δzeo-NFAT-DsRed2 plasmid and expressed both PuroR and DsRed2 (Fig. 3.2.3C). Nevertheless, there was no virus production after plasmid transfection. Notably, no ΔNFAT-DsRed2 translocation was observed after ionomycin stimulation (Fig. 3.2.3C).
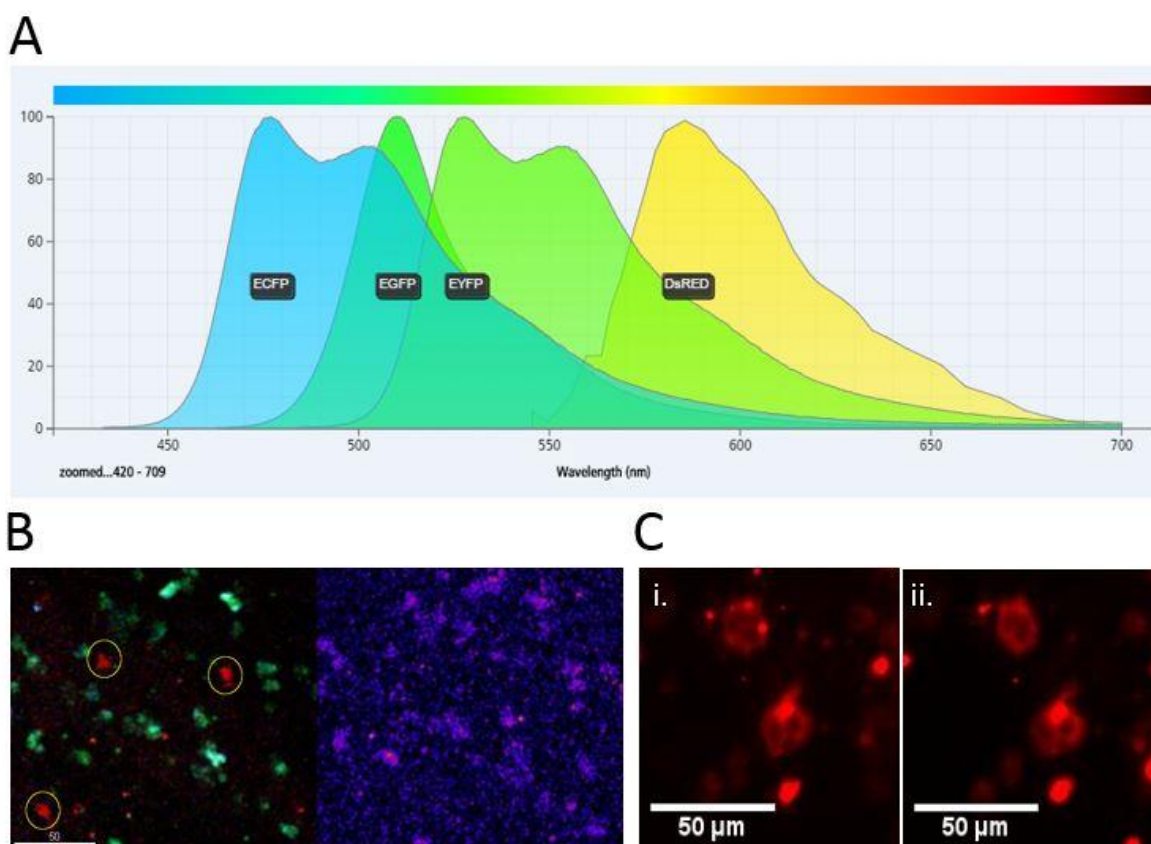
Figure 3.2.3 A. Fluorescence emission spectra of ECFP (blue) EGFP (deep green) EYFP (lighter green) and DsRed (yellow) (BD FLUORESCENCE SPECTRUM VIEWER) B. Sample images from *in vivo* calcium imaging of the meninges with T_OVA-Twitch1 cells (green) and T_MBP-DsRed2 cells (red – encircled). A pseudocolour ratio image with T cells (right) are depicted. Scale bar: 50 μm. C. Epifluorescence images of NFAT-DsRed2 expressing HEK 293 cells, before (i. Left) and after (ii. Right) addition of 4 μM ionomycin. Scale bar: 50 μm.

ΔNFAT mKate2 fusion

GP+E86 cells were transfected with the pMSCV-puro-ΔNFAT-mKate2 and expressed both PuroR and mKate2 (Fig. 3.2.4A). Similar to other red FPs, mKate2 presented a strong two-photon absorption in the region between 760-800 nm (Fig. 3.2.4B). Next, the translocation dynamics of ΔNFAT-GFP and ΔNFAT-mKate2 were investigated. Time-lapse recordings of *in vitro* co-cultured ΔNFAT-GFP and ΔNFAT-mKate2 expressing GP+E86 cells were acquired by fluorescent video-microscopy (Fig. 3.2.4C). Upon ionomycin stimulation, ΔNFAT-mKate2 was not toxic for the GP+E86 cells and the fluorescent signal of mKate2 was equally distributed at high expression levels within the cytosol or nucleus. However, the translocation of ΔNFAT-mKate2 from cytosol to nucleus occurred more slowly compared to ΔNFAT-GFP (Fig. 3.2.4D).
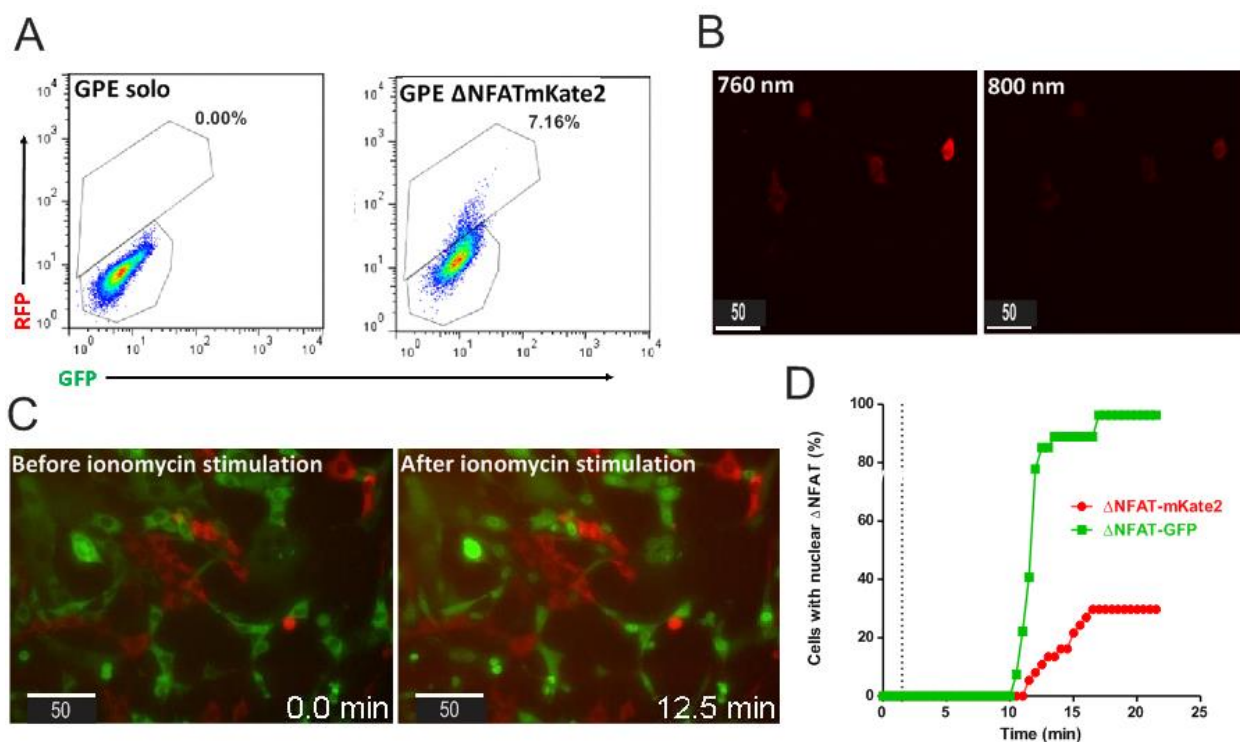
Figure 3.2.4 A. Flow cytometric analysis of ΔNFAT-mKate2 expression in GP+E86 cells before and after transfection. B. Two-photon microscopic acquisition of ΔNFAT-mKate2 expressing GP+E86 cells at two excitation wavelengths. C. Series from *in vitro* co-cultured ΔNFAT-GFP and ΔNFAT-mKate2 expressing GP+E86 cells before (left) and after (right) addition of 4 µM ionomycin. Images were acquired by fluorescence microscopy. D. Comparison of ΔNFAT-GFP and ΔNFAT-mKate2 translocation kinetics observed *in vitro* before and after addition of 4 µM ionomycin. The vertical line indicates the time point of ionomycin treatment. The results are representative of two independent experiments. B-C scale bar: 50 µm.

ΔNFAT mRuby2 and FusionRed fusions

GP+E86 cells were transfected with the pMSCV-puro-ΔNFAT-mRuby2 or pMSCV-puro-ΔNFAT-FusionRed vectors and later they were co-cultured with ΔNFAT-GFP expressing GP+E86 cells. The two-photon absorption properties of ΔNFAT-mRuby2 and ΔNFAT-FusionRed were tested at various excitation wavelengths (Fig. 3.2.5A and Fig. 3.2.6A). Upon two-photon irradiation, ΔNFAT-FusionRed presented a relatively stronger emission compared to ΔNFAT-mRuby2, nevertheless, both of them were visible in the spectral region of 800-810 nm.

As in the aforementioned ΔNFAT-mKate2 experiment and in order to examine the translocation dynamics, time-lapse recordings of vitro co-cultured ΔNFAT-GFP and ΔNFAT-mRuby2/ΔNFAT-FusionRed expressing GP+E86 cells were acquired by fluorescent video-microscopy (Fig. 3.2.5B and Fig. 3.2.6B). Upon 4 µM ionomycin stimulation, the translocation of all fused proteins from cytosol to nucleus occurred simultaneously (Fig. 3.2.5C and Fig. 3.2.6C).
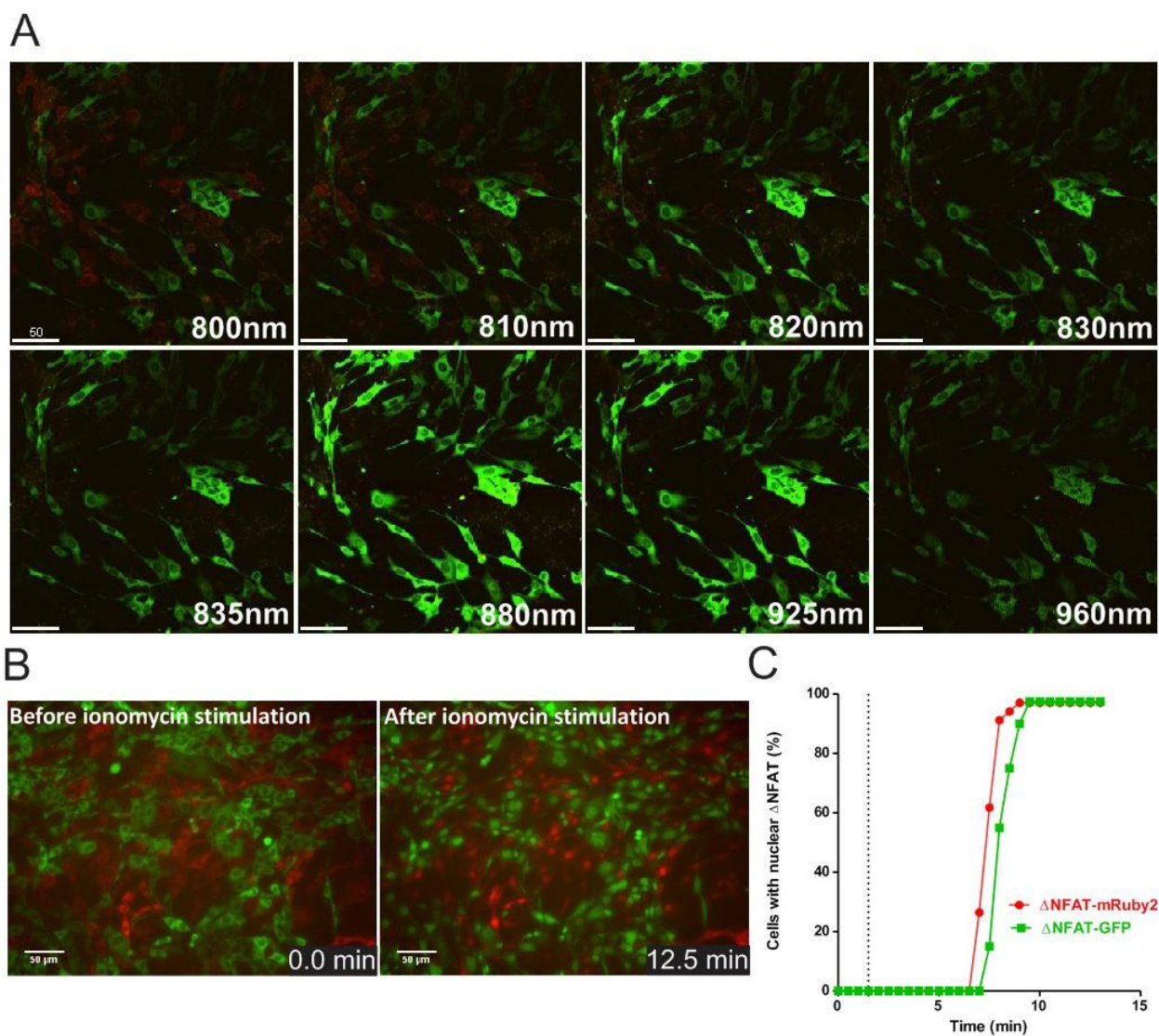
Figure 3.2.5 A. Two-photon microscopic acquisition of ΔNFAT-mRuby2 and ΔNFAT-GFP expressing GP+E86 cells at various excitation wavelengths. B. Series from *in vitro* co-cultured ΔNFAT-GFP and ΔNFAT-mRuby2 expressing GP+E86 cells before (left) and after (right) addition of 4 μM ionomycin. Images were acquired by fluorescence microscopy. A-B scale bar: 50 μm. C. Comparison of ΔNFAT-GFP and ΔNFAT-mRuby2 translocation kinetics observed *in vitro* before and after addition of 4 μM ionomycin. The vertical line indicates the time point of ionomycin treatment. The results are representative of two independent experiments.
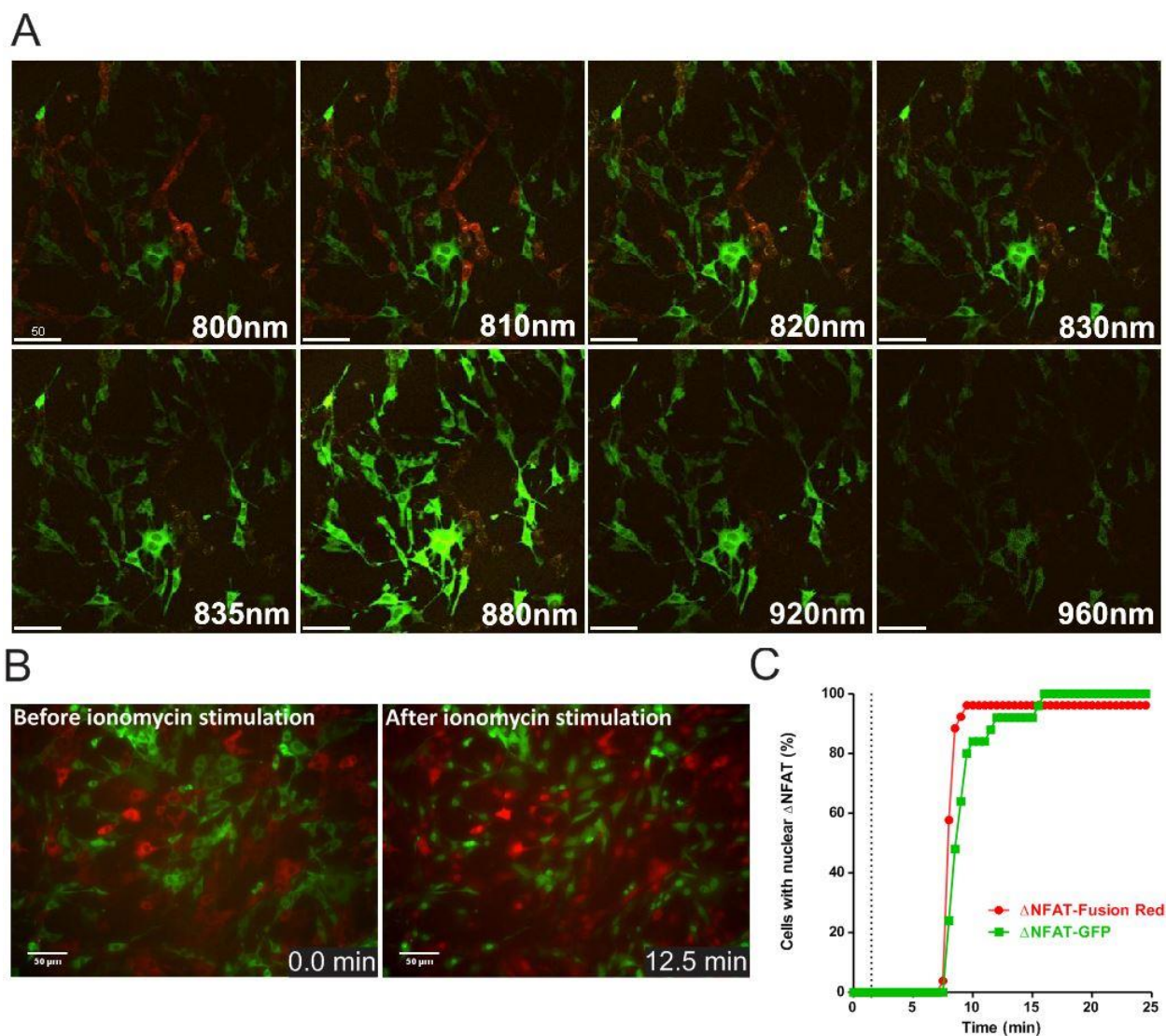
Figure 3.2.6 A. Two-photon microscopic acquisition of ΔNFAT-FusionRed and ΔNFAT-GFP expressing GP+E86 cells at various excitation wavelengths. B. Series from *in vitro* **co-cultured ΔNFAT-GFP and ΔNFAT-FusionRed expressing GP+E86 cells before (left) and after (right) addition of 4 µM ionomycin. Images were acquired by fluorescence microscopy. A-B scale bar: 50 µm. C. Comparison of ΔNFAT-GFP and ΔNFAT-FusionRed translocation kinetics observed** *in vitro* **before and after addition of 4 µM ionomycin. The vertical line indicates the time point of ionomycin treatment. The results are representative of two independent experiments.**

ΔNFAT LSSmOrange

GP+E86 cells were transfected with the pMSCV-ΔPGK-puro-ΔNFAT-LSSmOrange vector and they were co-cultured with ΔNFAT-GFP counterparts. ΔNFAT-LSSmOrange showed similar two-photon absorption compared to ΔNFAT-GFP in the spectral region between 800-900 nm (Fig. 3.2.7).
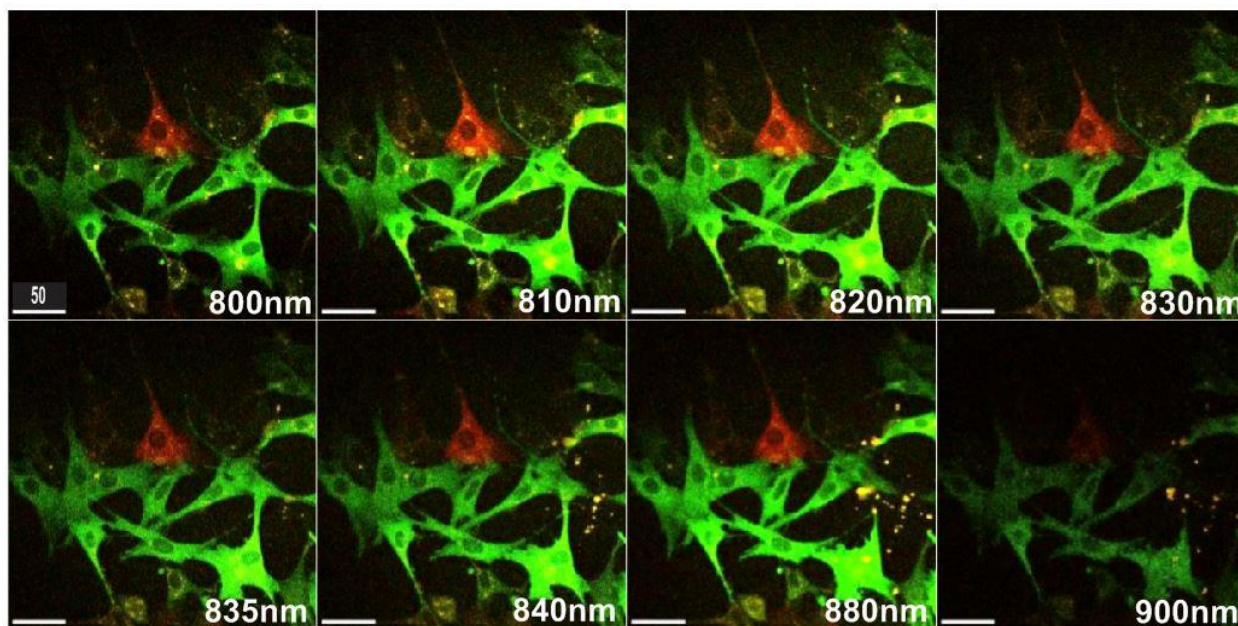
Figure 3.2.7 Two-photon microscopic acquisition of ΔNFAT-LSSmOrange and ΔNFAT-GFP expressing GP+E86 cells at various excitation wavelengths.

3.2.3 Combing NFAT and Twitch2B sensors

ΔNFAT-mRuby2 was selected as a reliable counterpart of ΔNFAT-GFP and was used for the construction of the dual sensor. The ΔNFAT-mRuby2-Twitch2B sequence was cloned into the PINCO vector (Fig. 3.2.8A) and time-lapse recordings of *in vitro* PINCO-puro-ΔNFAT-mRuby2-Twitch2B (Proteas) expressing GP+E86 cells were acquired by fluorescent video-microscopy, capturing the effects before and after ionomycin stimulation (Fig. 3.2.8B). As expected, the expression levels of both sensors differed amongst the cells. For this reason, dual expressing GP+E86 cells were isolated through cell sorting followed by further puromycin selection (Fig. 3.2.8C).
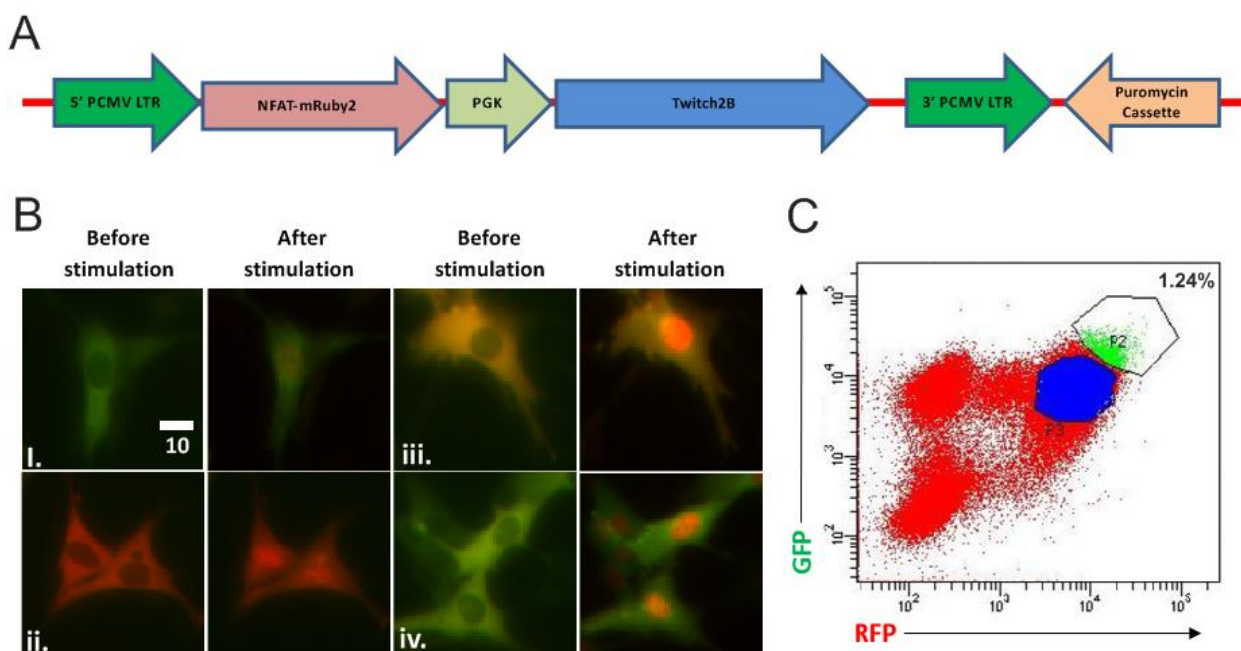
Figure 3.2.8 A. PINCO-puro-ΔNFAT-mRuby2-Twitch2B (Proteas) retroviral construct. B. Sample images from *in vitro* co-cultured GP+E86 cells with different expression patterns after Proteas transfection before (left) and after (right) addition of 4 μM ionomycin. i. cells expressing mainly Twitch2B ii. cells expressing only ΔNFAT-mRuby2 iii. cells expressing mainly ΔNFAT-mRuby2 iv. cells expressing both ΔNFAT-mRuby2 and Twitch2B. Images were acquired by fluorescence microscopy. Scale bar: 10 μm. C. Proteas expressing GP+E86 cells isolation by FACS sorting. A representative FACS graph of cells prepared *in vitro* after Proteas transfection. The P2 gate (green) represents highly expressing Proteas GP+E86 cells.

3.2.4 Two-photon microscopy of Proteas

The two-photon absorption properties of Proteas were tested over a range of 790–835 nm (Fig. 3.2.9A). The excitability and the fluorescence yield of both sensors strongly depended on the excitation wavelength. For example, at 790 nm only the ΔNFAT-mRuby2 was visible while at 835 nm it was barely detected. However, even far below the excitation peak for both sensors, it was still possible to generate reliable emission data. Series from *in vitro* calcium imaging of Proteas expressing GP+E86 cells were acquired by two-photon microscopy at 830 nm (Fig. 3.2.9B). Upon ionomycin stimulation, high-calcium signaling was instantly observed whereas the translocation of ΔNFAT-mRuby2 from cytosol to nucleus occurred within 5 minutes.
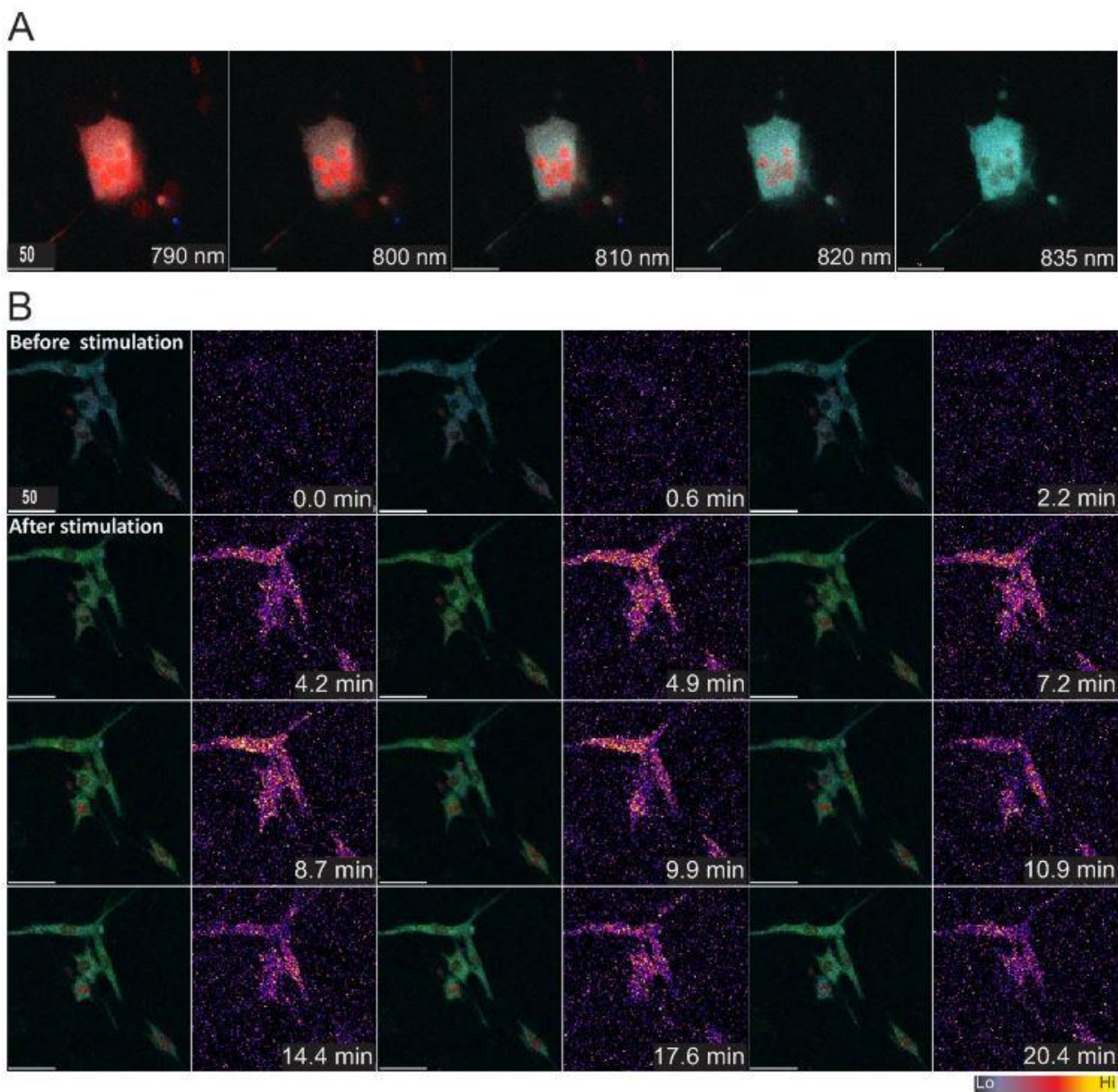
Figure 3.2.9 A. Two-photon microscopic acquisition of Proteas expressing GP+E86 cells at various excitation wavelengths after addition of 4 μM ionomycin. **B.** Series from *in vitro* calcium imaging of Proteas expressing GP+E86 cells before and after addition of 4 μM ionomycin at 830 nm wavelength. A fluorescence overlay of Proteas expressing GP+E86 cells (left) and a pseudocolour ratio image (right) are depicted. The inserted numbers indicate the relative time after the start of image acquisition. A-B. scale bar: 50 μm.

3.2.5 Establishing Proteas-labeled T cells

Primary T lymphocytes of preimmunized animals with MBP were cultivated together with Proteas transfected GP+E86 cells, producing a replication-deficient retrovirus. However, a Proteas gene transfer into rat antigen specific T cells was not successful (Fig. 3.2.10A). The gene transfer rates were extremely low, ranging between 0.05% and 0.1%.

The viral titers of three different viruses were tested in order to determine the retroviral integration and expression of Proteas in primary T lymphocytes. In a previous study, GFP transfected GP+E86 cells provided optimal doses of retroviruses to antigen specific T cells (Flügel et al., 1999) and Twitch1 transfected GP+E86 cells achieved a high efficiency gene delivery (see 3.1.1). Here, when NIH3T3 cells were treated with GFP and Twitch1 retroviruses, they produced high levels of transgene expression as measured by FACS (Fig. 3.2.10B). In contrast, the transduction efficiency of NIH3T3 cells with Proteas retroviruses was once again extremely low.
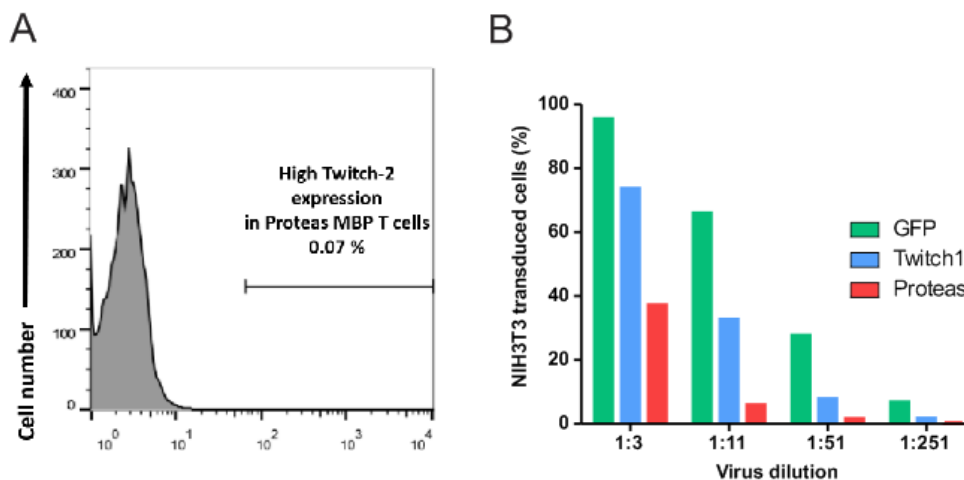
Figure 3.2.10 A. Representative flow cytometric histograms depicting Twitch2B expression levels of Proteas-expressing MBP specific T cells on day 5 after two rounds of restimulation. B. Comparison of GFP, Twitch1 and Proteas retroviral titers.

DISCUSSION

4.1 Context-dependent calcium signaling in encephalitogenic T cells

The autoreactive T cells follow a fascinating trek before they reach their ultimate target, the CNS white matter (Flügel et al., 2001). Their odyssey is not limited to one particular tissue; they travel through several distinct cellular milieus and they interact with local cells in the presence or absence of cognate antigen. These migratory cells receive signals that regulate their function and control their activation. Most of these signals are intimately linked with the intracellular calcium levels. The frequency, the duration and the topography of calcium signaling constitute indispensable indications for revealing indirectly the current status of a cell. In this study, calcium signaling was successfully visualized by applying the Twitch1 calcium sensor at a single cell resolution. During this study, Twitch1 was further optimised in order to express into rat T cells. As key modifications, the NeoR was shifted outside of the LTRs and the retroviral burden was reduced almost by 1.3 kb.

In order to study the effect of a chemokine or an antibody, it is always imperative to apply an experimental setup that reflects the physiological context. Especially for the GPCR-dependent short-lasting calcium spikes, numerous co-receptors and adaptor proteins are involved into the chemokine receptor signal. For example, calcium ionophores such as ionomycin that are used primarily in *in vitro* studies cannot mimic physiological stimuli and provoke similar signal transductions. Thus, only intravital imaging can reproduce the *in vivo* situation better than *in vitro* cell lines experiments. In addition, FACS calcium analysis cannot decipher the extent of activation and cannot track the contribution of a single cell to the overall response. Moreover, mouse EAE models are not the optimal to study encephalitogenic T cell infiltration into the CNS, because T cell infiltration kinetics vary among individuals. In contrast, *t*EAE model in Lewis rat showed excellent reproducibility and, therefore, is suitable to study T cell infiltration and interactions with local APCs.

The autoreactive T cells were imaged by two-photon intravital imaging both in the peripheral organs and the CNS. The limited scanning speed of the intravital two-photon setup that was used could not resolve calcium oscillations of <1 Hz such as those in neuronal cells, but it was sufficient to document intracellular calcium changes in T cells. Initially, during T cell-transferred EAE, freshly activated encephalitogenic T cells migrate to the peripheral organs (Wekerle et al., 1986) where they become licensed for CNS invasion (Schlager et al., 2016). Re-education occurs in the paracortical areas of 2° lymphatic tissues, which are occupied by T cells, DCs, macrophages, and fibroblastic reticular cells (Turley et al., 2010).

Next, in the spleen, the effector T cells are reprogrammed by down-regulating activation markers and up-regulating gene products that facilitate locomotion and cellular homing (Flügel et al., 2001). Interestingly, both MBP specific encephalitogenic and OVA specific non-encephalitogenic T cells showed similarly less frequent and short-lasting calcium spikes in the absence of specific antigen. Consequently, both MBP and OVA specific T cells acquire a migratory phenotype in the spleen. These spikes were partially blocked after the infusion of anti-MHCII antibodies. Antigen-independent intracellular calcium signaling could be triggered through GPCR signal transduction. Previously, fast confocal laser scanning technology revealed calcium spiking in response to GPCR engagement (Hillson and Hallett, 2007). In contradiction to an earlier report (Asperti-Boursin et al., 2007), it was described during this study that, PTX as well as other GPCR antagonists diminished short-lasting high-calcium signaling in the spleen without interfering with T cell migration. Besides, induction of calcium signaling *in vivo* with chemokine ligands would have been ambigious, mainly because the latter usually bind to the same receptor and activate different intracellular pathways (Zweemer et al., 2014). Antigen-independent intracellular calcium signaling was described previously *in vitro* by Revy et al. (Revy et al., 2001). They observed that in the absence of antigen, T cell-DC interactions produce weak and short calcium spikes. These responses were triggered mainly in naïve CD4$^+$ T cells which expressed a specific isoform of the repulsive molecule CD43. Since CD43 is involved in IS, calcium signaling seems to correlate with the formation of IS.

After acquiring a migratory phenotype in the spleen, the incoming T cells slow down and begin rolling along the inner vascular surface at spinal cord leptomeninges. Next, they attach firmly and crawl preferentially against the bloodstream until they extravasate or they are washed away. Short-lasting calcium spikes were observed when T cells proceeded from rolling to crawling. This infrequent high-calcium signaling could be explained by the fact that chemokines released by macrophages induce calcium influx via GPCRs and the elevated intracellular calcium switches the integrin confirmation from low to high affinity. Consequently, during leucocyte arrest, calcium influx promotes strengthened adhesion and cytoskeletal arrangement of many different cell types such as platelets, lymphocytes, fibroblasts, and endothelial cells (Dixit and Simon, 2012). For example, Orai1 synchronizes the transition between neutrophil rolling and arrest (Dixit and Simon, 2012).

T cell emigration into the leptomeningeal microenvironment occurs in two waves. After diapedesis, the prodromal T cells roam in close proximity within the perivascular area, until they encounter a particular set of local phagocytes (Bartholomäus et al., 2009). Upon antigen recognition, T cells present extensive high-calcium signaling ranging from some minutes to hours. At this point, the number of infiltrated T cells is quite low and T cells migrate along the blood vessels. The limited scope of scanning

around the meningeal vessels highlights the major contribution of perivascular macrophages in this process. In addition, both the expression of MHC class II molecules on glia cells and the production of inflammatory cytokines are low (Odoardi et al., 2012). Despite the fact that the capacity of antigen presentation to the T cells at the pre-clinical phase of EAE is limited (Bartholomäus et al., 2009), the duration of calcium spikes is longest on day 2 p.t. In fact, the early invading activated T cells start to produce inflammatory cytokines, which sequentially recruit other T cells and finally increase the permeability of BBB. This feedback-loop is in harmony with the hockey-stick kinetics of T cell invasion, which results in the exponential increase of the infiltrated T cell number.

A key finding that emerged from this study was the diversity of the stimulatory potential of individual leptomeningeal phagocytes. Each APC has different potential to stimulate T cells; some APCs attract numerous T cells and induce high-calcium responses, whereas other APCs are less active. This is not surprising because the availability of immunogenic myelin proteins is limited and the damage of the myelin sheath is minor in this EAE model. The infusion of myelin protein into the leptomeningeal space converted low-encephalitogenic T cells to high-encephalitogenic T cells (Odoardi et al., 2007a) and provided an indirect confirmation regarding the availability of endogenous antigens. In addition, those local APCs are not professional APCs, which are mainly found in the peripheral LNs (Bartholomäus et al., 2009). The stimulatory potential of individual leptomeningeal phagocytes can be linked to a 'first come – first served' rule.

Mempel et al. showed that antigen recognition can be separated into three phases (Mempel et al., 2004). During the initial phase, T cells showed repeated short-lasting contacts with APCs, which were followed by stable long-lasting contact on phase II. Later T cells detached from APCs and re-started free migration. In addition, T cell engagement is characterized by two distinct dynamics *in vivo* (Dustin, 2008). Upon encounter with an APC, T cells either develop transient contacts, termed immunological kinapses, or maintain sustained contacts from stable junctions called immunological synapses. The first type of behavior occurs during the early stages of T cell activation and mainly during Phase I and Phase III (Fooksman et al., 2010). In contrast, complete arrest of T cell migration and formation of synapses occurs only in Phase II. Nevertheless, during this study, no separated and distinct phases were observed for the majority of T cells. According to the aforementioned scheme, most of the APC contacts qualify as kinapses. Synapses were observed mainly during the 'first come – first served' phase, where contacts lasted for several hours and presented high intracellular calcium signals. This might be explained by the different type of T cells that were used. Antigen experienced effector T cells were injected, whereas Mempel et al. used naïve T cells. Effector T cells may possibly not need phase I, as they are already stimulated. It was

often observed that within a 10 minutes time frame, a particular encephalitogenic T cell makes multiple short-lasting contacts with APCs with acute calcium spikes, before it finally makes a stable contact with an APC with sustained calcium signaling. This sustained calcium signaling is much shorter compared to the contact duration of phase II that Mempel et al. described before. However, the three phase model fits perfectly for the early invading activated T cells during the 'first come – first served' phase. It can be speculated that CNS invasion initially follows the three phase model for breaching the BBB and, later, during the onset of *t*EAE, effector T cells preserve a maintenance phase. These findings support a previous suggestion that T cell-APC interactions within the leptomeninges serve to navigate effector T cells into the CNS parenchyma rather than arresting them for extended periods of time (Bartholomäus et al., 2009).

Wei et al. imaged calcium spikes in lymph node explants *ex vivo* by introducing T cells loaded with small-molecular fluorochrome (Wei et al., 2007). They described infrequent short-lasting calcium signaling under non-inflammatory condition as well as decreased motility during sustained high-calcium signaling. Moreover, they reported long-lasting calcium signaling, persisting over hours, under immunized condition, in contrast to this current study, which rarely showed contacts lasting for hours in the spinal cord leptomeninges. The aforementioned difference could be explained by the quality and quantity of antigen presentation. Immunization provides excess amount of antigen to professional APCs in lymph nodes; on the other hand, in the spinal cord meninges, even during the acute phase of inflammation, the quantity of local APCs and their saturation by endogenous antigen is limited. As Celli et al. suggested the availability of antigen presented on APC influences the duration of contacts and, hence, the T cell activation (Celli et al., 2007). Also, the antigen affinity determines the fate of a contact. Low-affinity antigens induce an exploratory behavior, characterized by partial deceleration and transient interactions with APCs (Moreau et al., 2015). The quality and the quantity of the antigen probably favors kinapses over synapses during the acute phase of inflammation in *t*EAE. In fact, this hypothesis was tested by administrating excess amount of specific antigen in the spleen. Infusion of soluble antigen caused direct arrest of specific T cells around the APCs, and constant rise of intracellular calcium levels.

In summary, it was shown that T cells present two different types of calcium signaling throughout their journey from i.v. transfer into the CNS parenchyma. The first type is antigen-independent and short-lasting, and is induced by GPCR-mediated and MHC-mediated signals. This type of calcium signaling might be essential in order to reprogram fully activated T cells to the migratory phenotype required for CNS infiltration. The second type of calcium signaling is the long-lasting, which depends on antigen and is closely linked with low motility and APC engagement. Sequentially, the saturated calcium signaling results in the nuclear translocation of NFAT and induces T cell activation.

The decryption of antigen-dependent and antigen-independent calcium responses in brain-autoimmune T cells may offer new therapeutic options. In peripheral immune organs, in particular, the reprogramming of freshly activated T cells to a "migratory" phenotype could be targeted. For example, Nicotinic Acid Adenine Dinucleotide Phosphate (NAADP) antagonist, BZ194, efficiently blocks intracellular calcium signaling (Dammermann et al., 2009) and ameliorates clinical EAE induced by the active immunization of myelin antigen via both prophylactic and therapeutic applications (Cordiglieri et al., 2010). Autoantigen presentation in the CNS leptomeninges should be reconsidered as an early therapeutic target, although previous treatment trials with MAbs were discouraging. In addition, the elevation of free chemokine levels may result in enhanced pathology (Zweemer et al., 2014). Nonetheless, more detailed studies need to be performed regarding the pharmacological blockade of GPCRs.

4.2   A dual sensor: Combing NFAT and Twitch sensors

Many aspects of CNS inflammation were still obscure, even after the development of the ΔNFAT-GFP activation sensor from the host lab (Pesic et al., 2013). Nevertheless, the obtained results significantly deepened the understandings of autoreactive T cell activation. In fact, the use of a Twitch calcium sensor enlightened the migratory mechanisms of CNS inflammation by successfully detecting weak signals such as the chemokine stimulation and the rolling-crawling transition.

Full activation, reflected by both the Twitch and NFAT sensors, happened in T cells with a high pathogenic potential, but not in weak encephalitogenic or non-encephalitogenic T cells (Kawakami et al., 2004). T cell activation often initiated with a series of brief contacts between T cells and APCs without ΔNFAT-GFP translocation, but ended in sustained adhesion with nuclear ΔNFAT displacement (Pesic et al., 2013). On the other hand, $T_{MBP-Twitch1}$ responded with acute calcium spikes during short-lasting contacts preceding arrest and long-lasting calcium spikes. Taken together, it can be speculated that calcium signaling is cumulative from multiple sources, and only after sufficient tonic signals ΔNFAT-GFP translocates to the nucleus (Henrickson et al., 2008). To test this hypothesis, the co-expression of Twitch and ΔNFAT-GFP within the same cell was necessary.

At first, it was essential to determine the ideal red fluorescent protein for ΔNFAT fusion. Five candidates ranging from the orange to the far-red fluorescence emission spectra were tested and compared with ΔNFAT-GFP. Two basic comparison criteria were evaluated: the two-photon absorption in the spectral region between 800-835 nm and the translocation dynamics upon stimulation. It is important to note that the excitation peak of an FP in two-photon microscopy does not always correspond with twice the wavelength of the one-photon microscopy excitation peak. In two-photon microscopy, many red FPs

have a broad excitation spectrum and high two-photon cross section in the range of 700-770 nm due to a higher-energy or short wavelength transitions of their chromophores (Fig. 4.2.1) (Drobizhev et al., 2011).
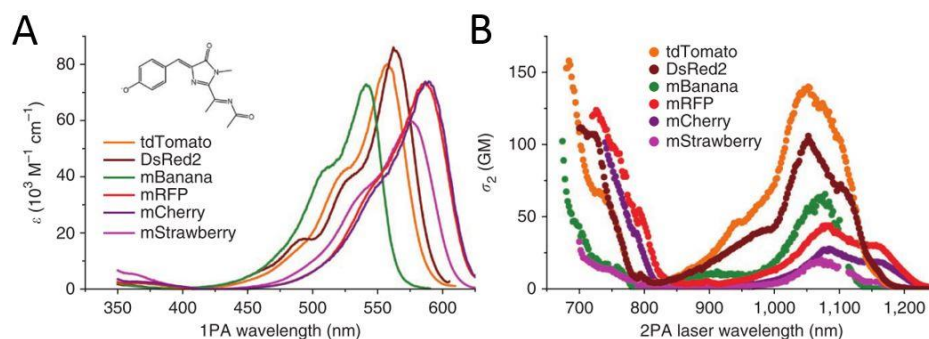
Figure 4.2.1 The one-photon (A) and two-photon (B) spectra of the Fruit series of fluorescent proteins. (adopted from Drobizhev et. al., 2011).

DsRed2 was the first tested candidate fused to ΔNFAT. It is a variant of red fluorescent protein drFP583, originally isolated from the sea anemone *Discosoma striata* (Matz et al., 1999). This FP is an obligate tetramer and presents higher solubility and lower tendency to form aggregates compared to DsRed1 (Clontech). DsRed2 was initially selected as a putative candidate for NFAT fusion because it exhibits distinct spectral properties in multicolor labeling experiments (Bartholomäus et al., 2009). In fact, in co-transferred experiments, DsRed2-labeled MBP specific T cells served to guide T$_{OVA-Twitch1}$ cells to meninges. However, all the attempts to express a DsRed2-ΔNFAT fusion protein were unsuccessful. After lentiviral transfection, brightly fluorescent dots in cells were observed. This cytotoxic effect was caused by non-specific dsRed2 oligomerization and formation of large aggregates. Besides, it was previously reported that DsRed-Express2 protein is suitable only for labeling whole cells rather than generating fusion proteins (Strack et al., 2008).

Next, the mKate2 fluorescent protein was evaluated. This is a far-red fluorescent protein generated after site-directed and two rounds of random mutagenesis of mKate (Shcherbo et al., 2009). Originally, the precursor FP mKate derived from the TagRFP which is expressed on the sea anemone *Entacmaea quadricolor* (Shcherbo et al., 2007). mKate2 was selected as a putative candidate for NFAT fusion because it is considered a super bright far-red FP (Shcherbo et al., 2009). Indeed, this FP is almost 3-fold brighter than mKate and 10-fold brighter than mPlum. In addition, mKate2 has been reported before for its successful performance in the majority of fusion constructs and its high level photostability during long-term time-lapse imaging, under both widefield and confocal microscopy (Shcherbo et al., 2009). Importantly, no visible aggregates or non-specific localizations were observed within 4 days of transfection in mammalian cells at high expression levels (Shcherbo et al., 2009). However, the translocation kinetics of ΔNFAT-mKate2 turned out slower compared to ΔNFAT-GFP. Despite

the initial naming of mKate2 where m- stands for monomeric, mKate2 is not monomeric. Indeed, high-pressure liquid chromatography revealed a dimeric character for the mKate2 (Shemiakina et al., 2012). Consequently, translocation occurred only partially because the monomer–dimer mKate2 equilibrium interfered with the normal function and localization of the ΔNFAT fusion protein.

Similar to mKate2, the far-red FP mRuby2 descends from the sea anemone *Entacmaea quadricolor* (Kredel et al., 2009, Lam et al., 2012). Together with the FP Clover, they consist an excellent pair for FRET imaging that exhibits less photobleaching when compared to mRuby (Lam et al., 2012). Since the FP Clover has longer excitation and emission maxima compared to EYFP, it was considered that mRuby2 and Twitch1 would have minimal crosstalk in their emission channels as well. FusionRed derives from mKate2 and demonstrates similar brightness, spectral and biochemical properties with its precursor (Shemiakina et al., 2012). This FP has been subjected to artificial monomerization (Shemiakina et al., 2012) because, as it was already mentioned, mKate2 displays a monomer-dimer equilibrium at low micromolar concentrations (Lin et al., 2009). FusionRed was selected as a putative candidate for NFAT fusion due to its proven performance in the majority of fusion constructs while no lysosomal localization was observed after 4 days of expression (Shemiakina et al., 2012). According to the present study, both ΔNFAT-mRuby2 and ΔNFAT-FusionRed presented sufficient two-photon absorption within the required spectral region and similar translocation dynamics compared to ΔNFAT-GFP. Therefore, both can be applied as a reliable counterpart of ΔNFAT-GFP.

The last tested candidate fused to ΔNFAT was LSSmOrange. It is a large Stokes shift (LSS) monomeric FP with red-shifted emission spectra derived from mOrange (Shaner et al., 2004). This FP was selected as a putative candidate for NFAT fusion because it is spectrally compatible with the CFP-YFP pair and was efficiently excited before in a four color single excitation confocal microscopy (Shcherbakova et al., 2012). Similar to mRuby2 and FusionRed, this FP demonstrated high photostability. Unfortunately, due to technical limitations, it was not possible to test this sensor under fluorescent video-microscopy. Thus, the translocation dynamics of ΔNFAT-LSSmOrange were not studied.

Five red FPs were evaluated and it was concluded that ΔNFAT-mRuby2, ΔNFAT-FusionRed and possibly ΔNFAT-LSSmOrange (more detailed studies need to be performed concerning the translocation dynamics) consist a reliable counterpart of ΔNFAT-GFP and could be used for the construction of a dual sensor. However, mRuby2 was preferred because it was used before in combination with Clover (Lam et al., 2012) and it would be an ideal partner for Twitch2B as well. Indeed, *in vitro* two-photon microscopic acquisition of Proteas (PINCO-puro-ΔNFAT-mRuby2-Twitch2B) expressing GP+E86 cells displayed excellent translocation kinetics and adequate two-photon absorption. Nevertheless, Proteas

gene transfer into rat antigen specific T cells was not successful. The low transduction efficiency of Proteas retrovirus probably occurred because of a promoter interference between the LTRs and the PGK. In general, internal strong promoters such as the PGK promoter compete with the transcription signals of the retroviral enhancers and severely decrease the viral titers (Blo et al., 2008).

Overall, this study made a substantial contribution to the body of knowledge in the visualization of fusion proteins by evaluating five candidates from the red fluorescent protein color palette. It consists a crucial step for expressing combined sensors and deciphering complex processes of the immune response.

REFERENCES

AFFATICATI, P., MIGNEN, O., JAMBOU, F., POTIER, M. C., KLINGEL-SCHMITT, I., DEGROUARD, J., PEINEAU, S., GOUADON, E., COLLINGRIDGE, G. L., LIBLAU, R., CAPIOD, T. & COHEN-KAMINSKY, S. 2011. Sustained calcium signalling and caspase-3 activation involve NMDA receptors in thymocytes in contact with dendritic cells. *Cell Death Differ,* 18**,** 99-108.

ARAMBURU, J., GARCIA-COZAR, F., RAGHAVAN, A., OKAMURA, H., RAO, A. & HOGAN, P. G. 1998. Selective inhibition of NFAT activation by a peptide spanning the calcineurin targeting site of NFAT. *Mol Cell,* 1**,** 627-37.

ASPERTI-BOURSIN, F., REAL, E., BISMUTH, G., TRAUTMANN, A. & DONNADIEU, E. 2007. CCR7 ligands control basal T cell motility within lymph node slices in a phosphoinositide 3-kinase-independent manner. *J Exp Med,* 204**,** 1167-79.

BAHBOUHI, B., BERTHELOT, L., PETTRE, S., MICHEL, L., WIERTLEWSKI, S., WEKSLER, B., ROMERO, I. A., MILLER, F., COURAUD, P. O., BROUARD, S., LAPLAUD, D. A. & SOULILLOU, J. P. 2009. Peripheral blood CD4+ T lymphocytes from multiple sclerosis patients are characterized by higher PSGL-1 expression and transmigration capacity across a human blood-brain barrier-derived endothelial cell line. *J Leukoc Biol,* 86**,** 1049-63.

BALAGOPALAN, L., BARR, V. A. & SAMELSON, L. E. 2009. Endocytic events in TCR signaling: focus on adapters in microclusters. *Immunol Rev,* 232**,** 84-98.

BARTHOLOMÄUS, I., KAWAKAMI, N., ODOARDI, F., SCHLÄGER, C., MILJKOVIC, D., ELLWART, J. W., KLINKERT, W. E. F., FLÜGEL-KOCH, C., ISSEKUTZ, T. B., WEKERLE, H. & FLÜGEL, A. 2009. Effector T cell interactions with meningeal vascular structures in nascent autoimmune CNS lesions. *Nature,* 462**,** 94-98.

BEN-NUN, A., KAUSHANSKY, N., KAWAKAMI, N., KRISHNAMOORTHY, G., BERER, K., LIBLAU, R., HOHLFELD, R. & WEKERLE, H. 2014. From classic to spontaneous and humanized models of multiple sclerosis: impact on understanding pathogenesis and drug development. *J Autoimmun,* 54**,** 33-50.

BEN-NUN, A., WEKERLE, H. & COHEN, I. R. 1981a. The rapid isolation of clonable antigen-specific T lymphocyte lines capable of mediating autoimmune encephalomyelitis. *European Journal of Immunology,* 11**,** 195-199.

BEN-NUN, A., WEKERLE, H. & COHEN, I. R. 1981b. Vaccination against autoimmune encephalomyelitis using attenuated cells of a T lymphocyte line reactive against myelin basic protein. *Nature,* 292**,** 60-61.

BENNETT, L. D., FOX, J. M. & SIGNORET, N. 2011. Mechanisms regulating chemokine receptor activity. *Immunology,* 134**,** 246-56.

BERER, K., MUES, M., KOUTROULOS, M., AL RASBI, Z., BOZIKI, M., JOHNER, C., WEKERLE, H. & KRISHNAMOORTHY, G. 2011. Commensal microbiota and myelin autoantigen cooperate to trigger autoimmune demyelination. *Nature,* 479**,** 538-541.

BITSCH, A., SCHUCHARDT, J., BUNKOWSKI, S., KUHLMANN, T. & BRUCK, W. 2000. Acute axonal injury in multiple sclerosis. Correlation with demyelination and inflammation. *Brain,* 123 (Pt 6)**,** 1174-83.

BLO, M., MICKLEM, D. R. & LORENS, J. B. 2008. Enhanced gene expression from retroviral vectors. *BMC Biotechnol,* 8**,** 19.

CAHALAN, M. D. & PARKER, I. 2008. Choreography of cell motility and interaction dynamics imaged by two-photon microscopy in lymphoid organs. *Annu Rev Immunol,* 26**,** 585-626.

CAMPBELL, B., VOGEL, P. J., FISHER, E. & LORENZ, R. 1973. Myelin basic protein administration in multiple sclerosis. *Arch Neurol,* 29**,** 10-5.

CELLI, S., LEMAÎTRE, F. & BOUSSO, P. 2007. Real-time manipulation of T cell-dendritic cell interactions in vivo reveals the importance of prolonged contacts for CD4 + T cell activation *Immunity,* 27**,** 625-634.

CHRISTO, S. N., DIENER, K. R. & HAYBALL, J. D. 2015. The functional contribution of calcium ion flux heterogeneity in T cells. *Immunol Cell Biol*.

CICCARELLI, O., BARKHOF, F., BODINI, B., DE STEFANO, N., GOLAY, X., NICOLAY, K., PELLETIER, D., POUWELS, P. J., SMITH, S. A., WHEELER-KINGSHOTT, C. A., STANKOFF, B., YOUSRY, T. & MILLER, D. H. 2014. Pathogenesis of multiple sclerosis: insights from molecular and metabolic imaging. *Lancet Neurol,* 13**,** 807-22.

CORDIGLIERI, C., ODOARDI, F., ZHANG, B., NEBEL, M., KAWAKAMI, N., KLINKERT, W. E. F., LODYGIN, D., LÜHDER, F., BREUNIG, E., SCHILD, D., ULAGANATHAN, V. K., DORNMAIR, K., DAMMERMANN, W., POTTER, B. V. L., GUSE, A. H. & FLÜGEL, A. 2010. Nicotinic acid adenine dinucleotide phosphate-mediated calcium signalling in effector T cells regulates autoimmunity of the central nervous system. *Brain,* 133**,** 1930-1943.

DAMMERMANN, W., ZHANG, B., NEBEL, M., CORDIGLIERI, C., ODOARDI, F., KIRCHBERGER, T., KAWAKAMI, N., DOWDEN, J., SCHMID, F., DORNMAIR, K., HOHENEGGER, M., FLÜGEL, A., GUSE, A. H. & POTTER, B. V. L. 2009. NAADP-mediated Ca2+ signaling via type 1 ryanodine receptor in T cells revealed by a synthetic NAADP antagonist. *Proceedings of the National Academy of Sciences (USA),* 106**,** 10678-10683.

DIXIT, N. & SIMON, S. I. 2012. Chemokines, selectins and intracellular calcium flux: temporal and spatial cues for leukocyte arrest. *Front Immunol,* 3**,** 188.

DOLMETSCH, R. E., LEWIS, R. S., GOODNOW, C. C. & HEALY, J. I. 1997. Differential activation of transcription factors induced by Ca2+ response amplitude and duration. *Nature,* 386**,** 855-8.

DOLMETSCH, R. E., XU, K. & LEWIS, R. S. 1998. Calcium oscillations increase the efficiency and specificity of gene expression. *Nature,* 392**,** 933-6.

DROBIZHEV, M., MAKAROV, N. S., TILLO, S. E., HUGHES, T. E. & REBANE, A. 2011. Two-photon absorption properties of fluorescent proteins. *Nat Methods,* 8**,** 393-9.

DUSTIN, M. L. 2008. T-cell activation through immunological synapses and kinapses. *Immunol Rev,* 221**,** 77-89.

ENGELHARDT, B. & COISNE, C. 2011. Fluids and barriers of the CNS establish immune privilege by confining immune surveillance to a two-walled castle moat surrounding the CNS castle. *Fluids Barriers CNS,* 8**,** 4.

ENGELHARDT, B. & RANSOHOFF, R. M. 2012. Capture, crawl, cross: the T cell code to breach the blood-brain barriers. *Trends Immunol,* 33**,** 579-89.

FAROUDI, M., UTZNY, C., SALIO, M., CERUNDOLO, V., GUIRAUD, M., MULLER, S. & VALITUTTI, S. 2003. Lytic versus stimulatory synapse in cytotoxic T lymphocyte/target cell interaction: manifestation of a dual activation threshold. *Proc Natl Acad Sci U S A,* 100**,** 14145-50.

FESKE, S. 2007. Calcium signalling in lymphocyte activation and disease. *Nat Rev Immunol,* 7**,** 690-702.

FESKE, S., SKOLNIK, E. Y. & PRAKRIYA, M. 2012. Ion channels and transporters in lymphocyte function and immunity. *Nat Rev Immunol,* 12**,** 532-47.

FLÜGEL, A., BERKOWICZ, T., RITTER, T., LABEUR, M., JENNE, D., LI, Z., ELLWART, J., WILLEM, M., LASSMANN, H. & WEKERLE, H. 2001. Migratory activity and functional changes of green fluorescent effector T cells before and during experimental autoimmune encephalomyelitis. *Immunity,* 14**,** 547-560.

FLÜGEL, A., WILLEM, M., BERKOWICZ, T. & WEKERLE, H. 1999. Gene transfer into CD4 + T lymphocytes: Green fluorescent protein engineered, encephalitogenic T cells used to illuminate immune responses in the brain. *Nature Medicine,* 5**,** 843-847.

FOOKSMAN, D. R., VARDHANA, S., VASILIVER-SHAMIS, G., LIESE, J., BLAIR, D. A., WAITE, J., SACRISTAN, C., VICTORA, G. D., ZANIN-ZHOROV, A. & DUSTIN, M. L. 2010. Functional anatomy of T cell activation and synapse formation. *Annu Rev Immunol,* 28**,** 79-105.

FREUND, J., STERN, E. R. & PISANI, T. M. 1947. Isoallergic encephalomyelitis and radiculitis in Guinea pigs after one injection of brain and mycobacteria in water-in-oil emulsion. *Journal of Immunology,* 57**,** 179-195.

FRIESE, M. A., SCHATTLING, B. & FUGGER, L. 2014. Mechanisms of neurodegeneration and axonal dysfunction in multiple sclerosis. *Nat Rev Neurol,* 10**,** 225-38.

FRISCHER, J. M., BRAMOW, S., DAL-BIANCO, A., LUCCHINETTI, C. F., RAUSCHKA, H., SCHMIDBAUER, M., LAURSEN, H., SORENSEN, P. S. & LASSMANN, H. 2009. The relation between inflammation and neurodegeneration in multiple sclerosis brains. *Brain,* 132**,** 1175-89.

GOWANS, J. L. 1966. Life-span, recirculation, and transformation of lymphocytes. *Int Rev Exp Pathol,* 5**,** 1-24.

GRIGNANI, F., KINSELLA, T., MENCARELLI, A., VALTIERI, M., RIGANELLI, D., GRIGNANI, F., LANFRANCONE, L., PESCHLE, C., NOLAN, G. P. & PELICCI, P. G. 1998. High-efficiency gene transfer and selection of human hematopoietic progenitor cells with a hybrid EBV/retroviral vector expressing the green fluorescence protein. *Cancer Res,* 58**,** 14-9.

GRYNKIEWICZ, G., POENIE, M. & TSIEN, R. Y. 1985. A new generation of Ca2+ indicators with greatly improved fluorescence properties. *J Biol Chem,* 260**,** 3440-50.

HARBO, H. F., GOLD, R. & TINTORE, M. 2013. Sex and gender issues in multiple sclerosis. *Therapeutic Advances in Neurological Disorders,* 6**,** 237-248.

HARBO, H. F., LIE, B. A., SAWCER, S., CELIUS, E. G., DAI, K. Z., OTURAI, A., HILLERT, J., LORENTZEN, A. R., LAAKSONEN, M., MYHR, K. M., RYDER, L. P., FREDRIKSON, S., NYLAND, H., SORENSEN, P. S., SANDBERG-WOLLHEIM, M., ANDERSEN, O., SVEJGAARD, A., EDLAND, A., MELLGREN, S. I., COMPSTON, A., VARTDAL, F. & SPURKLAND, A. 2004. Genes in the HLA class I region may contribute to the HLA class II-associated genetic susceptibility to multiple sclerosis. *Tissue Antigens,* 63**,** 237-47.

HENRICKSON, S. E., MEMPEL, T. R., MAZO, I. B., LIU, B., ARTYMOV, M. N., ZHENG, H., PEIXOTO, A., FLYNN, M. P., SENMAN, B., JUNT, T., WONG, H. C., CHAKRABORTY, A. K. & VON ANDRIAN, U. H. 2008. T cell sensing of antigen dose governs interactive behavior with dendritic cells and sets a threshold for T cell activation. *Nature Immunology,* 9**,** 282-291.

HILLERT, J. & OLERUP, O. 1993. Multiple sclerosis is associated with genes within or close to the HLA-DR-DQ subregion on a normal DR15,DQ6,Dw2 haplotype. *Neurology,* 43**,** 163-168.

HILLSON, E. J. & HALLETT, M. B. 2007. Localised and rapid Ca2+ micro-events in human neutrophils: conventional Ca2+ puffs and global waves without peripheral-restriction or wave cycling. *Cell Calcium,* 41**,** 525-36.

HOCHWELLER, K., WABNITZ, G. H., SAMSTAG, Y., SUFFNER, J., HÄMMERLING, G. J. & GARBI, N. 2010. Dendritic cells control T cell tonic signaling required for responsiveness to foreign antigen. *Proceedings of the National Academy of Sciences (USA),* 107**,** 5931-5936.

HOU, X., PEDI, L., DIVER, M. M. & LONG, S. B. 2012. Crystal structure of the calcium release-activated calcium channel Orai. *Science,* 338**,** 1308-13.

HOWELL, O. W., REEVES, C. A., NICHOLAS, R., CARASSITI, D., RADOTRA, B., GENTLEMAN, S. M., SERAFINI, B., ALOISI, F., RONCAROLI, F., MAGLIOZZI, R. & REYNOLDS, R. 2011. Meningeal inflammation is widespread and linked to cortical pathology in multiple sclerosis. *Brain,* 134**,** 2755-71.

INTERNATIONAL MULTIPLE SCLEROSIS GENETICS, C., WELLCOME TRUST CASE CONTROL, C., SAWCER, S., HELLENTHAL, G., PIRINEN, M., SPENCER, C. C., PATSOPOULOS, N. A., MOUTSIANAS, L., DILTHEY, A., SU, Z., FREEMAN, C., HUNT, S. E., EDKINS, S., GRAY, E., BOOTH, D. R., POTTER, S. C., GORIS, A., BAND, G., OTURAI, A. B., STRANGE, A., SAARELA, J., BELLENGUEZ, C., FONTAINE, B., GILLMAN, M., HEMMER, B., GWILLIAM, R., ZIPP, F., JAYAKUMAR, A., MARTIN, R., LESLIE, S., HAWKINS, S., GIANNOULATOU, E., D'ALFONSO, S., BLACKBURN, H., MARTINELLI BONESCHI, F., LIDDLE, J., HARBO, H. F., PEREZ, M. L., SPURKLAND, A., WALLER, M. J., MYCKO, M. P., RICKETTS, M., COMABELLA, M., HAMMOND, N., KOCKUM, I., MCCANN, O. T., BAN, M., WHITTAKER, P., KEMPPINEN, A., WESTON, P., HAWKINS, C., WIDAA, S., ZAJICEK, J., DRONOV, S., ROBERTSON, N., BUMPSTEAD, S. J., BARCELLOS, L. F., RAVINDRARAJAH, R., ABRAHAM, R., ALFREDSSON, L., ARDLIE, K., AUBIN, C., BAKER, A., BAKER, K., BARANZINI, S. E., BERGAMASCHI, L., BERGAMASCHI, R.,

BERNSTEIN, A., BERTHELE, A., BOGGILD, M., BRADFIELD, J. P., BRASSAT, D., BROADLEY, S. A., BUCK, D., BUTZKUEVEN, H., CAPRA, R., CARROLL, W. M., CAVALLA, P., CELIUS, E. G., CEPOK, S., CHIAVACCI, R., CLERGET-DARPOUX, F., CLYSTERS, K., COMI, G., COSSBURN, M., COURNU-REBEIX, I., COX, M. B., COZEN, W., CREE, B. A., CROSS, A. H., CUSI, D., DALY, M. J., DAVIS, E., DE BAKKER, P. I., DEBOUVERIE, M., D'HOOGHE M, B., DIXON, K., DOBOSI, R., DUBOIS, B., ELLINGHAUS, D., et al. 2011. Genetic risk and a primary role for cell-mediated immune mechanisms in multiple sclerosis. *Nature,* 476**,** 214-9.

JENSEN, P. C. & ROSENKILDE, M. M. 2009. Chapter 8. Activation mechanisms of chemokine receptors. *Methods Enzymol,* 461**,** 171-90.

JOSEPH, N., REICHER, B. & BARDA-SAAD, M. 2014. The calcium feedback loop and T cell activation: how cytoskeleton networks control intracellular calcium flux. *Biochim Biophys Acta,* 1838**,** 557-68.

JUNGER, W. G. 2011. Immune cell regulation by autocrine purinergic signalling. *Nat Rev Immunol,* 11**,** 201-12.

KAWAKAMI, N., LASSMANN, S., LI, Z., ODOARDI, F., RITTER, T., ZIEMSSEN, T., KLINKERT, W. E. F., ELLWART, J., BRADL, M., KRIVACIC, K., LASSMANN, H., RANSOHOFF, R. M., VOLK, H. D., WEKERLE, H., LININGTON, C. & FLÜGEL, A. 2004. The activation status of neuroantigen-specific T cells in the target organ determines the clinical outcome of autoimmune encephalomyelitis. *Journal of Experimental Medicine,* 199**,** 185-197.

KAWAKAMI, N., NÄGERL, U. V., ODOARDI, F., BONHOEFFER, T., WEKERLE, H. & FLÜGEL, A. 2005. Live imaging of effector cell trafficking and autoantigen recognition within the unfolding autoimmune encephalomyelitis lesion. *Journal of Experimental Medicine,* 201**,** 1805-1814.

KLINKERT, W. E. F. 1987. Homing of antigen-specific T cells in the Lewis rat. I. Accumulation of antigen reactive T cells in the perithymic lymph nodes. *Journal of Immunology,* 139**,** 1030-1036.

KOTTURI, M. F., HUNT, S. V. & JEFFERIES, W. A. 2006. Roles of CRAC and Cav-like channels in T cells: more than one gatekeeper? *Trends Pharmacol Sci,* 27**,** 360-7.

KREDEL, S., OSWALD, F., NIENHAUS, K., DEUSCHLE, K., ROCKER, C., WOLFF, M., HEILKER, R., NIENHAUS, G. U. & WIEDENMANN, J. 2009. mRuby, a bright monomeric red fluorescent protein for labeling of subcellular structures. *PLoS One,* 4**,** e4391.

KRISHNAMOORTHY, G., LASSMANN, H., WEKERLE, H. & HOLZ, A. 2006. Spontaneous opticospinal encephalomyelitis in a double-transgenic mouse model of autoimmune T cell/B cell cooperation. *Journal of Clinical Investigation,* 116**,** 2385-2392.

KRISHNAMOORTHY, G. & WEKERLE, H. 2009. EAE: an immunologist's magic eye. *Eur J Immunol,* 39**,** 2031-5.

KUHN, P. H., WANG, H., DISLICH, B., COLOMBO, A., ZEITSCHEL, U., ELLWART, J. W., KREMMER, E., ROSSNER, S. & LICHTENTHALER, S. F. 2010. ADAM10 is the physiologically relevant, constitutive alpha-secretase of the amyloid precursor protein in primary neurons. *EMBO J,* 29**,** 3020-32.

LAM, A. J., ST-PIERRE, F., GONG, Y., MARSHALL, J. D., CRANFILL, P. J., BAIRD, M. A., MCKEOWN, M. R., WIEDENMANN, J., DAVIDSON, M. W., SCHNITZER, M. J., TSIEN, R. Y. & LIN, M. Z. 2012. Improving FRET dynamic range with bright green and red fluorescent proteins. *Nat Methods,* 9**,** 1005-12.

LEWIS, R. S. 2001. Calcium signaling mechanisms in T lymphocytes. *Annu Rev Immunol,* 19**,** 497-521.

LIN, M. Z., MCKEOWN, M. R., NG, H. L., AGUILERA, T. A., SHANER, N. C., CAMPBELL, R. E., ADAMS, S. R., GROSS, L. A., MA, W., ALBER, T. & TSIEN, R. Y. 2009. Autofluorescent proteins with excitation in the optical window for intravital imaging in mammals. *Chem Biol,* 16**,** 1169-79.

LODYGIN, D., ODOARDI, F., SCHLAGER, C., KORNER, H., KITZ, A., NOSOV, M., VAN DEN BRANDT, J., REICHARDT, H. M., HABERL, M. & FLUGEL, A. 2013. A combination of fluorescent NFAT and H2B sensors uncovers dynamics of T cell activation in real time during CNS autoimmunity. *Nat Med,* 19**,** 784-90.

MACIAN, F. 2005. NFAT proteins: key regulators of T-cell development and function. *Nat Rev Immunol,* 5**,** 472-84.

MADSEN, L. S., ANDERSSON, E. C., JANSSON, L., KROGSGAARD, M., ANDERSEN, C. B., ENGSBERG, J., STROMINGER, J. L., SVEJGAARD, A., HOLMDAHL, R., WUCHERPFENNIG, K. W. & FUGGER, L. 1999. A humanized model for multiple sclerosis using HLA DR2 and a human T cell receptor. *Nature Genetics,* 23**,** 343-347.

MAIER, L. M., ANDERSON, D. E., SEVERSON, C. A., BAECHER-ALLAN, C., HEALY, B., LIU, D. V., WITTRUP, K. D., DE JAGER, P. L. & HAFLER, D. A. 2009. Soluble IL-2RA levels in multiple sclerosis subjects and the effect of soluble IL-2RA on immune responses. *J Immunol,* 182**,** 1541-7.

MANGMOOL, S. & KUROSE, H. 2011. G(i/o) protein-dependent and -independent actions of Pertussis Toxin (PTX). *Toxins (Basel),* 3**,** 884-99.

MANK, M., SANTOS, A. F., DIRENBERGER, S., MRSIC-FLOGEL, T. D., HOFER, S. B., STEIN, V., HENDEL, T., REIFF, D. F., LEVELT, C., BORST, A., BONHOEFFER, T., HÜBENER, M. & GRIESBECK, O. 2008. A genetically encoded calcium indicator for chronic in vivo two-photon imaging *Nature Methods,* 5**,** 805-811.

MARANGONI, F., MUROOKA, T. T., MANZO, T., KIM, E. Y., CARRIZOSA, E., ELPEK, N. M. & MEMPEL, T. R. 2013. The transcription factor NFAT exhibits signal memory during serial T cell interactions with antigen-presenting cells. *Immunity,* 38**,** 237-49.

MATZ, M. V., FRADKOV, A. F., LABAS, Y. A., SAVITSKY, A. P., ZARAISKY, A. G., MARKELOV, M. L. & LUKYANOV, S. A. 1999. Fluorescent proteins from nonbioluminescent Anthozoa species. *Nat Biotechnol,* 17**,** 969-73.

MEMPEL, T. R., HENRICKSON, S. E. & VON ANDRIAN, U. H. 2004. T-cell priming by dendritic cells in lymph nodes occurs in three distinct phases. *Nature,* 427**,** 154-159.

MINTA, A., KAO, J. P. & TSIEN, R. Y. 1989. Fluorescent indicators for cytosolic calcium based on rhodamine and fluorescein chromophores. *J Biol Chem,* 264**,** 8171-8.

MIYAWAKI, A., LLOPIS, J., HEIM, R., MCCAFFERY, J. M., ADAMS, J. A., IKURA, M. & TSIEN, R. Y. 1997. Fluorescent indicators for Ca2+ based on green fluorescent proteins and calmodulin. *Nature,* 388**,** 882-7.

MOREAU, H. D., LEMAITRE, F., GARROD, K. R., GARCIA, Z., LENNON-DUMENIL, A. M. & BOUSSO, P. 2015. Signal strength regulates antigen-mediated T-cell deceleration by distinct mechanisms to promote local exploration or arrest. *Proc Natl Acad Sci U S A,* 112**,** 12151-6.

MUES, M., BARTHOLOMAUS, I., THESTRUP, T., GRIESBECK, O., WEKERLE, H., KAWAKAMI, N. & KRISHNAMOORTHY, G. 2013. Real-time in vivo analysis of T cell activation in the central nervous system using a genetically encoded calcium indicator. *Nature Medicine,* 19**,** 778-83.

MUSTELIN, T. & TASKEN, K. 2003. Positive and negative regulation of T-cell activation through kinases and phosphatases. *Biochem J,* 371**,** 15-27.

ODOARDI, F., KAWAKAMI, N., KLINKERT, W. E. F., WEKERLE, H. & FLÜGEL, A. 2007a. Blood-borne soluble protein antigen intensifies T cell activation in autoimmune CNS lesions and exacerbates clinical disease. *Proceedings of the National Academy of Sciences (USA),* 104**,** 18625-18630.

ODOARDI, F., KAWAKAMI, N., LI, Z. X., CORDIGLIERI, C., RUNE, K., KLINKERT, W. E. F., ELLWART, J. W., BAUER, J., LASSMANN, H., WEKERLE, H. & FLÜGEL, A. 2007b. Instant effect of soluble antigen on effector T cells in peripheral immune organs during immunotherapy of autoimmune encephalomyelitis. *Proceedings of the National Academy of Sciences (USA),* 104**,** 920-925.

ODOARDI, F., SIE, C., STREYL, K., ULAGANATHAN, V. K., SCHLÄGER, C., LODYGIN, D., HECKELSMILLER, K., NIETFELD, W., ELLWART, J., KLINKERT, W. E. F., LOTTAZ, C., NOSOV, M., BRINKMANN, V., SPANG, R., LEHRACH, H., VINGRON, M., WEKERLE, H., FLÜGEL-KOCH, C. & FLÜGEL, A. 2012. Encephalitogenic T cells get licensed in the lung for entry into the central nervous system *Nature*.

OMILUSIK, K. D., NOHARA, L. L., STANWOOD, S. & JEFFERIES, W. A. 2013. Weft, warp, and weave: the intricate tapestry of calcium channels regulating T lymphocyte function. *Front Immunol,* 4**,** 164.

PARK, C. Y., HOOVER, P. J., MULLINS, F. M., BACHHAWAT, P., COVINGTON, E. D., RAUNSER, S., WALZ, T., GARCIA, K. C., DOLMETSCH, R. E. & LEWIS, R. S. 2009. STIM1 clusters and activates CRAC channels via direct binding of a cytosolic domain to Orai1. *Cell,* 136**,** 876-90.

PENNA, A., DEMURO, A., YEROMIN, A. V., ZHANG, S. L., SAFRINA, O., PARKER, I. & CAHALAN, M. D. 2008. The CRAC channel consists of a tetramer formed by Stim-induced dimerization of Orai dimers. *Nature,* 456**,** 116-20.

PESIC, M., BARTHOLOMAUS, I., KYRATSOUS, N. I., HEISSMEYER, V., WEKERLE, H. & KAWAKAMI, N. 2013. 2-photon imaging of phagocyte-mediated T cell activation in the CNS. *J Clin Invest,* 123**,** 1192-201.

PICCIO, L., ROSSI, B., SCARPINI, E., LAUDANNA, C., GIAGULLI, C., ISSEKUTZ, A. C., VESTWEBER, D., BUTCHER, E. C. & CONSTANTIN, G. 2002. Molecular mechanisms involved in lymphocyte recruitment in inflamed brain microvessels: critical roles for P-selectin glycoprotein ligand-1 and heterotrimeric G(i)-linked receptors. *J Immunol,* 168**,** 1940-9.

PÖLLINGER, B., KRISHNAMOORTHY, G., BERER, K., LASSMANN, H., BÖSL, M., DUNN, R., DOMINGUES, H. S., HOLZ, A., KURSCHUS, F. C. & WEKERLE, H. 2009. Spontaneous relapsing-remitting EAE in the SJL/J mouse: MOG-reactive transgenic T cells recruit endogenous MOG-specific B cells. *Journal of Experimental Medicine,* 206**,** 1303-1316.

POZO-GUISADO, E., CASAS-RUA, V., TOMAS-MARTIN, P., LOPEZ-GUERRERO, A. M., ALVAREZ-BARRIENTOS, A. & MARTIN-ROMERO, F. J. 2013. Phosphorylation of STIM1 at ERK1/2 target sites regulates interaction with the microtubule plus-end binding protein EB1. *J Cell Sci,* 126**,** 3170-80.

QIN, K., DONG, C., WU, G. & LAMBERT, N. A. 2011. Inactive-state preassembly of G(q)-coupled receptors and G(q) heterotrimers. *Nat Chem Biol,* 7**,** 740-7.

RAGHEB, S. & LISAK, R. P. 1993. Multiple sclerosis: genetic background versus environment. *Annals of Neurology,* 34**,** 509-10.

RAMAGOPALAN, S. V., HEGER, A., BERLANGA, A. J., MAUGERI, N. J., LINCOLN, M. R., BURRELL, A., HANDUNNETTHI, L., HANDEL, A. E., DISANTO, G., ORTON, S. M., WATSON, C. T., MORAHAN, J. M., GIOVANNONI, G., PONTING, C. P., EBERS, G. C. & KNIGHT, J. C. 2010. A ChIP-seq defined genome-wide map of vitamin D receptor binding: associations with disease and evolution. *Genome Res,* 20**,** 1352-60.

RAMAGOPALAN, S. V., MAUGERI, N. J., HANDUNNETTHI, L., LINCOLN, M. R., ORTON, S. M., DYMENT, D. A., DELUCA, G. C., HERRERA, B. M., CHAO, M. J., SADOVNICK, A. D., EBERS, G. C. & KNIGHT, J. C. 2009. Expression of the multiple sclerosis-associated MHC class II Allele HLA-DRB1*1501 is regulated by vitamin D. *PLoS Genet,* 5**,** e1000369.

RANDRIAMAMPITA, C. & LELLOUCH, A. C. 2014. Imaging early signaling events in T lymphocytes with fluorescent biosensors. *Biotechnol J,* 9**,** 203-12.

RANSOHOFF, R. M. 2012. Immunology: Licensed in the lungs. *Nature,* 488**,** 595-6.

RANSOHOFF, R. M., HAFLER, D. A. & LUCCHINETTI, C. F. 2015. Multiple sclerosis-a quiet revolution (vol 11, pg 134, 2015). *Nature Reviews Neurology,* 11.

REITER, E. & LEFKOWITZ, R. J. 2006. GRKs and beta-arrestins: roles in receptor silencing, trafficking and signaling. *Trends Endocrinol Metab,* 17**,** 159-65.

REVY, P., SOSPEDRA, M., BARBOUR, B. & TRAUTMANN, A. 2001. Functional antigen-independent synapses formed between T cells and dendritic cells. *Nature Immunology,* 2**,** 925-931.

RHODE, B. W., EMERMAN, M. & TEMIN, H. M. 1987. Instability of large direct repeats in retrovirus vectors. *J Virol,* 61**,** 925-7.

RIVERS, T. M., SPRUNT, D. H. & BERRY, G. P. 1933. Observations on attempts to produce acute disseminated encephalomyelitis in monkeys. *Journal of Experimental Medicine,* 58**,** 39-53.

SCALFARI, A., NEUHAUS, A., DAUMER, M., MURARO, P. A. & EBERS, G. C. 2014. Onset of secondary progressive phase and long-term evolution of multiple sclerosis. *J Neurol Neurosurg Psychiatry,* 85**,** 67-75.

SCHLAGER, C., KORNER, H., KRUEGER, M., VIDOLI, S., HABERL, M., MIELKE, D., BRYLLA, E., ISSEKUTZ, T., CABANAS, C., NELSON, P. J., ZIEMSSEN, T., ROHDE, V., BECHMANN, I., LODYGIN, D., ODOARDI, F. & FLUGEL, A. 2016. Effector T-cell trafficking between the leptomeninges and the cerebrospinal fluid. *Nature,* 530**,** 349-53.

SCHULZE-LUEHRMANN, J. & GHOSH, S. 2006. Antigen-receptor signaling to nuclear factor kappa B. *Immunity,* 25**,** 701-15.

SERAFINI, B., ROSICARELLI, B., FRANCIOTTA, D., MAGLIOZZI, R., REYNOLDS, R., CINQUE, P., ANDREONI, L., TRIVEDI, P., SALVETTI, M., FAGGIONI, A. & ALOISI, F. 2007. Dysregulated Epstein-Barr virus infection in the multiple sclerosis brain. *Journal of Experimental Medicine,* 204**,** 2899-2912.

SHANER, N. C., CAMPBELL, R. E., STEINBACH, P. A., GIEPMANS, B. N., PALMER, A. E. & TSIEN, R. Y. 2004. Improved monomeric red, orange and yellow fluorescent proteins derived from Discosoma sp. red fluorescent protein. *Nat Biotechnol,* 22**,** 1567-72.

SHAW, K. T., HO, A. M., RAGHAVAN, A., KIM, J., JAIN, J., PARK, J., SHARMA, S., RAO, A. & HOGAN, P. G. 1995. Immunosuppressive drugs prevent a rapid dephosphorylation of transcription factor NFAT1 in stimulated immune cells. *Proceedings of the National Academy of Sciences of the United States of America,* 92**,** 11205-9.

SHCHERBAKOVA, D. M., HINK, M. A., JOOSEN, L., GADELLA, T. W. & VERKHUSHA, V. V. 2012. An orange fluorescent protein with a large Stokes shift for single-excitation multicolor FCCS and FRET imaging. *J Am Chem Soc,* 134**,** 7913-23.

SHCHERBO, D., MERZLYAK, E. M., CHEPURNYKH, T. V., FRADKOV, A. F., ERMAKOVA, G. V., SOLOVIEVA, E. A., LUKYANOV, K. A., BOGDANOVA, E. A., ZARAISKY, A. G., LUKYANOV, S. & CHUDAKOV, D. M. 2007. Bright far-red fluorescent protein for whole-body imaging. *Nat Methods,* 4**,** 741-6.

SHCHERBO, D., MURPHY, C. S., ERMAKOVA, G. V., SOLOVIEVA, E. A., CHEPURNYKH, T. V., SHCHEGLOV, A. S., VERKHUSHA, V. V., PLETNEV, V. Z., HAZELWOOD, K. L., ROCHE, P. M., LUKYANOV, S., ZARAISKY, A. G., DAVIDSON, M. W. & CHUDAKOV, D. M. 2009. Far-red fluorescent tags for protein imaging in living tissues. *Biochem J,* 418**,** 567-74.

SHEMIAKINA, II, ERMAKOVA, G. V., CRANFILL, P. J., BAIRD, M. A., EVANS, R. A., SOUSLOVA, E. A., STAROVEROV, D. B., GOROKHOVATSKY, A. Y., PUTINTSEVA, E. V., GORODNICHEVA, T. V., CHEPURNYKH, T. V., STRUKOVA, L., LUKYANOV, S., ZARAISKY, A. G., DAVIDSON, M. W., CHUDAKOV, D. M. & SHCHERBO, D. 2012. A monomeric red fluorescent protein with low cytotoxicity. *Nat Commun,* 3**,** 1204.

SHULMAN, Z., COHEN, S. J., ROEDIGER, B., KALCHENKO, V., JAIN, R., GRABOVSKY, V., KLEIN, E., SHINDER, V., STOLER-BARAK, L., FEIGELSON, S. W., MESHEL, T., NURMI, S. M., GOLDSTEIN, I., HARTLEY, O., GAHMBERG, C. G., ETZIONI, A., WENINGER, W., BEN-BARUCH, A. & ALON, R. 2012. Transendothelial migration of lymphocytes mediated by intraendothelial vesicle stores rather than by extracellular chemokine depots. *Nat Immunol,* 13**,** 67-76.

SMOLDERS, J. 2011. Vitamin d and multiple sclerosis: correlation, causality, and controversy. *Autoimmune Dis,* 2011**,** 629538.

SOMMER, F., BISCHOF, S., ROLLINGHOFF, M. & LOHOFF, M. 1994. Demonstration of organic anion transport in T lymphocytes. L-lactate and fluo-3 are target molecules. *J Immunol,* 153**,** 3523-32.

SONG, S., LI, J., ZHU, L., CAI, L., XU, Q., LING, C., SU, Y. & HU, Q. 2012. Irregular Ca(2+) oscillations regulate transcription via cumulative spike duration and spike amplitude. *J Biol Chem,* 287**,** 40246-55.

STRACK, R. L., STRONGIN, D. E., BHATTACHARYYA, D., TAO, W., BERMAN, A., BROXMEYER, H. E., KEENAN, R. J. & GLICK, B. S. 2008. A noncytotoxic DsRed variant for whole-cell labeling. *Nat Methods,* 5**,** 955-7.

THESTRUP, T., LITZLBAUER, J., BARTHOLOMAUS, I., MUES, M., RUSSO, L., DANA, H., KOVALCHUK, Y., LIANG, Y., KALAMAKIS, G., LAUKAT, Y., BECKER, S., WITTE, G., GEIGER, A., ALLEN, T., ROME, L. C., CHEN, T. W., KIM, D. S., GARASCHUK, O., GRIESINGER, C. & GRIESBECK, O. 2014. Optimized ratiometric

calcium sensors for functional in vivo imaging of neurons and T lymphocytes. *Nat Methods,* 11**,** 175-82.

TSIEN, R. Y., RINK, T. J. & POENIE, M. 1985. Measurement of cytosolic free Ca2+ in individual small cells using fluorescence microscopy with dual excitation wavelengths. *Cell Calcium,* 6**,** 145-57.

TURLEY, S. J., FLETCHER, A. L. & ELPEK, K. G. 2010. The stromal and haematopoietic antigen-presenting cells that reside in secondary lymphoid organs. *Nat Rev Immunol,* 10**,** 813-25.

WEI, S. H., SAFRINA, O., YU, Y., GARROD, K. R., CAHALAN, M. D. & PARKER, I. 2007. Ca 2+ signals in CD4 + T cells during early contacts with antigen-bearing dendritic cells in lymph node *Journal of Immunology,* 179 1586-1594.

WEKERLE, H., LININGTON, C., LASSMANN, H. & MEYERMANN, R. 1986. Cellular immune reactivity within the CNS. *Trends in Neuroscience,* 9**,** 271-277.

WILLER, C. J., DYMENT, D. A., RISCH, N. J., SADOVNICK, A. D., EBERS, G. C. & CANADIAN COLLABORATIVE STUDY, G. 2003. Twin concordance and sibling recurrence rates in multiple sclerosis. *Proc Natl Acad Sci U S A,* 100**,** 12877-82.

YEO, T. W., DE JAGER, P. L., GREGORY, S. G., BARCELLOS, L. F., WALTON, A., GORIS, A., FENOGLIO, C., BAN, M., TAYLOR, C. J., GOODMAN, R. S., WALSH, E., WOLFISH, C. S., HORTON, R., TRAHERNE, J., BECK, S., TROWSDALE, J., CAILLIER, S. J., IVINSON, A. J., GREEN, T., POBYWAJLO, S., LANDER, E. S., PERICAK-VANCE, M. A., HAINES, J. L., DALY, M. J., OKSENBERG, J. R., HAUSER, S. L., COMPSTON, A., HAFLER, D. A., RIOUX, J. D. & SAWCER, S. 2007. A second major histocompatibility complex susceptibility locus for multiple sclerosis. *Ann Neurol,* 61**,** 228-36.

ZLOKOVIC, B. V. 2008. The blood-brain barrier in health and chronic neurodegenerative disorders. *Neuron,* 57**,** 178-201.

ZWEEMER, A. J., TORASKAR, J., HEITMAN, L. H. & AP, I. J. 2014. Bias in chemokine receptor signalling. *Trends Immunol,* 35**,** 243-52.

ABBREVIATIONS

7TM	seven transmembrane
αMHCI	anti-MHC class I
αMHCII	anti-MHC class II
ΔNFAT	truncated NFAT
APC	Antigen Presenting Cell
BBB	Blood-Brain Barrier
c	cytosolic
CaM	Calmodulin
CD	Codon Diversified
CD	Cluster of Differentiation
CFP	Cyan Fluorescent Protein
CMV	Cytomegalovirus
CNS	Central Nervous System
CRAC	Calcium-Release-Activated Calcium
DAG	Diacylglycerol
DMEM	Dulbecco's Modified Eagle Medium
DMSO	Dimethyl Sulfoxide
EAE	Experimental Autoimmune Encephalomyelitis
EDTA	Ethylenediaminetetraacetic Acid
EH	Eagle's HEPES
ER	Endoplasmic Reticulum
FACS	Fluorescence-Activated Cell Sorting
FCS	Fetal Calf Serum
FP	Fluorescent Protein
FRET	Förster/Fluorescence Resonance Energy Transfer
G proteins	GTP-binding proteins
GALT	Gut Associated Lymphoid Tissue

GFP	Green Fluorescent Protein
GPCR	G Protein Coupled Receptor
HEPES	4-(2-hydroxyethyl)-1-piperazineethanesulfonic acid
HLA	Human Leukocyte Antigens
i.v.	intravenous
IFNγ	Interferon Gamma
IRES	Internal Ribosomal Entry Site
IL	Interleukin
IP_3	Inositol triphosphate
IP_3R	tetrameric IP_3 Receptor
IS	Immunological Synapse
ITAM	Immunoreceptor Tyrosine-based Activation Motif
ITK	IL-2 Inducible T cell Kinase
LAT	Linker for Activation of T cells
LCK	Lymphocyte-specific protein tyrosine Kinase
LSS	large Stokes Shift
LTR	Long Terminal Repeat
MBP	Myelin Basic Protein
MHC	Major Histocompatibility Complex
MOG	Myelin Oligodendrocyte Glycoprotein
MS	Multiple Sclerosis
n	nuclear
NeoR	Neomycin Resistance cassette
NFAT	Nuclear Factor of Activated T cells
NF-κB	Nuclear Factor kappa B
ns	not significant
ORF	Open Reading Frame
ori	origin of replication
OVA	Ovalbumin

p.t.	post transfer
PBS	Phosphate Buffered Saline
PCR	Polymerase Chain Reaction
PFA	Paraformaldehyde
PGK	Phosphoglycerate Kinase promoter
PLCγ1	Phospholipase Cγ1
PM	Plasma Membrane
PMA	Phorbol 12-Myristate 13-Acetate
PTX	Pertussis Toxin
PuroR	Puromycin Resistance gene
R	Ratio
rcf	relative centrifugal force
RFP	Red Fluorescent Protein
ROI	Regions Of Interest
SLP76	SRC-homology-2-domain-containing Leukocyte Protein of 76 kDa
SNARF	Seminaphthorhodafluor
SOCE	Store-Operated Calcium Entry
SRC	Sarcoma tyrosine kinase
STIM	Stromal Cell Interaction Molecule
TCGF	T Cell Grow Factor
TCM	T Cell Medium
TCR	T Cell Receptor
*t*EAE	transfer EAE
TnC	Troponin C
YFP	Yellow Fluorescent Protein
ZAP	Zeta-chain-Associated Protein kinase

RESOURCES & CONTRIBUTIONS

T cell lines were established by Dr. Naoto Kawakami with technical assistance of Sabine Kosin.

Antibody production was performed by Dr. Naoto Kawakami with technical assistance of Sabine Kosin.

PINCO-Twitch1 and PINCO-Twitch2B clonings were partially performed by Dr. Marsilius Mues.

Lentivirus production and transduction experiments were performed by Stefan Lichtenthaler's Lab (DZNE).

Analysis tools including programs for the automated export of two-photon imaging data and the analysis of T cell motility and APC contacts were provided by Dr. Ingo Bartholomäus and Guokun Zhang.

Experiments regarding the translocation dynamics of red fluorescent protein candidates were partially performed by Dr. Marija Pesic.

Part of analysis of motility of T cells was performed by Dr. Marija Pesic, Miriam Wörner and Ping Fang.

Cell sorting was performed by Dr. Martin Spitaler (MPI Biochemistry, Munich) and Joachim W. Ellwart (Institute for Experimental Hematology, Helmholtz Centre, Munich).

PUBLICATIONS

A.L. Savvides, T.L. Nikolakopoulou, **N. Kyratsous**, E.A. Katsifas, G. Kanini and A.D. Karagouni: Bacterial Deterioration of Marble Monuments: A Case Study of the Conservation Project of Acropolis Monuments. *Geomicrobiology Journal*. 31. 726-736 (2014)

M. Pesic, N. Kawakami, I. Bartholomäus, , and **N.I. Kyratsous**: Imaging of immune cell behavior   and function in multiple sclerosis and experimental autoimmune encephalomyelitis. *Clinical and Experimental Neuroimmunology*. 4. 27-35 (2013)

M. Pesic, I. Bartholomäus, **N.I. Kyratsous**, V. Heissmeyer, H. Wekerle, and N. Kawakami: 2-photon imaging of phagocyte-mediated T cell activation in the CNS. *Journal of Clinical Investigation* 123. 1192-1201 (2013)

N. Kawakami, I. Bartholomäus, M. Pesic, and **N.I. Kyratsous**: Intravital imaging of autoreactive T cells in living animals. *Methods in Cell Biology*. 113. 149-168 (2013)

ACKNOWLEDGEMENTS